Propagation Models for Multiple-Antenna Systems: Methodology, Measurements, and Statistics.

by

Keith T. Herring

Submitted to the Department of Electrical Engineering and
Computer Science
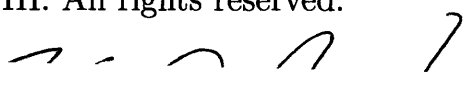in partial fulfillment of the requirements for the degree of

Doctor of Philosophy in Electrical Engineering and Computer Science

at the

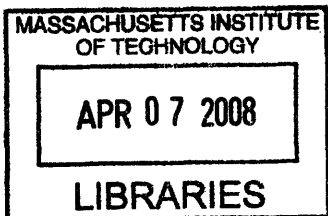MASSACHUSETTS INSTITUTE OF TECHNOLOGY

February 2008

Author ....
Department of Electrical Engineering and
Computer Science
February. 2008

Certified by......................................
David H. Staelin
Professor of Electrical Engineering
Thesis Supervisor

Accepted by.......................................
Terry P. Orlando
Chairman, Department Committee on Graduate Students

Propagation Models for

Multiple-Antenna Systems:

Methodology, Measurements, and Statistics.

by

Keith T. Herring

Abstract

The trend in wireless communications is towards utilization of multiple antenna systems. While techniques such as beam-forming and spatial diversity have been implemented for some time, the emergence of Multiple-Input Multiple-Output (MIMO) communications has increased commercial interest and development in multiple-antenna technology. Given this trend it has become increasingly important that we understand the propagation characteristics of the environments where this new technology will be deployed. In particular the development of low-cost, high-performance system architectures and protocols is largely dependent on the accuracy of available channel models for approximating realized propagation behavior.

The first contribution of this thesis is a methodology for the modeling of wireless propagation in multiple antenna systems. Specifically we consider the problem of propagation modeling from the perspective of the protocol designer and system engineer. By defining the wireless channel as the complex narrow-band channel response h ϵ C between two devices, we characterize the important degrees of freedom associated with the channel by modeling it as a function of its path-loss, multipath/frequency, time stability, spatial, and polarization characteristics. We then motivate this model by presenting a general set of design decisions that depend on these parameters such as network density, channel allocation, and channel-state information (CSI) update rate. Lastly we provide a parametrization of the environment into measurable factors that can be used to predict channel behavior including link-length, Line-Of-Sight (LOS), link topology (e.g. air-to-ground), building density, and other physical parameters.

The second contribution of this thesis is the experimental analysis and development of this modeling space. Specifically we have gathered a large database of real wireless channel data from a diverse set of propagation environments. A mobile channel-data collection system was built for obtaining the required data which includes an eight-channel software receiver and a collection of WiFi channel sounders. The software receiver synchronously samples the 20-MHz band centered at 2.4 GHz from eight configurable antennas. Measure-

ments have been carried out for both air-to-ground and ground-to-ground links for distances ranging from tens of meters to several kilometers throughout the city of Cambridge, MA.

Here we have developed a collection of models for predicting channel behavior, including a model for estimating the path-loss coefficient α in street environments that utilizes two physical parameters: P_1 = percentage of building gaps averaged over each side of the street, P_2 = percentage of the street length that has a building gap on at least one side of the street. Results show a linear increase in α of 0.53 and 0.32 per 10% increase in P_1 and P_2, respectively, with RMS errors of 0.47 and 0.27 α for α's between 2 and 5. Experiments indicate a 10dB performance advantage in estimating path-loss with this multi-factor model over the optimal linear estimator (upper-bound empirical model) for link lengths as short as 100 meters. In contrast, air-to-ground links have been shown to exhibit log-normal fading with an average attenuation of $\alpha \approx 2$ and standard deviation of 8dB.

Additionally we provide exhaustive evidence that the small-scale fading behavior (frequency domain) of both Non-Line-Of-Sight (NLOS) air-to-ground and ground-to-ground links as short as tens of meters is Rayleigh distributed. More specifically, fading distributions across a diverse set of environments and link lengths have been shown to have Rician K-factors smaller than 1, suggesting robust performance of the Rayleigh model. A model is also presented that defines a stochastic distribution for the delay-spread of the channel as a function of the link-length (d_o), multipath component (MPC) decay-rate (β = attenuation per unit delay $[\frac{dBm}{10\cdot\log_{10}(m)}]$), and MPC arrival-rate (q = MPCs per unit delay $[\frac{MPCs}{m}]$). Experiments support the use of this model over a spectrum of link-lengths (50m-700m) and indicate a dense arrival-rate (q) (on the order of 1 $\frac{MPC}{m}$) in ground-to-ground links. In this range the frequency structure of the channel is insensitive to q, which reduces the modeling complexity to a single unknown parameter, β. We provide estimators for β over a variety of environment types that have been shown to closely replicate the fade width distribution in these environments.

The observed time-coherence length (t_c) of MPCs tend to be either less than 300ms (high-frequency) or 5 seconds and longer (low-frequency), resulting in a Rician-like distribution for fading in the time domain. We show that the time characteristics of the channel are accurately modeled as the superposition of two independent circularly symmetric complex gaussian random variables corresponding to the channel response due to a set of stable and unstable MPCs. We observe the S-factor, defined as the ratio of average power in stable to unstable MPCs (distinct from the Rician K-factor), which ranges between 0-30dB depending on environment and link length, and can be estimated with an rms error of 3dB in both ground-to-ground and air-to-ground link regimes. Experiments show improved performance of this model over the Rician fading model which has been shown to underestimate high fade events (tails) in the time domain, corresponding to cases where the stable MPCs destructively combine to form a null.

Additionally, the Kronecker MIMO channel model is shown to predict channel capacity (of a 7x7 system) with an rms error of 1.7 $\frac{bits}{s\cdot Hz}$ (at 20dB SNR) over a diverse set of observed outdoor environments. Experiments indicate a 3dB performance advantage in this prediction when applied to environments that are not dominated by single-bounce propagation paths (Single-bounce: 2.1 $\frac{bits}{s\cdot Hz}$ rms, Multi-bounce: 1 $\frac{bits}{s\cdot Hz}$ rms).

Thesis Supervisor: David H. Staelin
Title: Professor of Electrical Engineering

Acknowledgments

As the contemporary American legend Stephen Colbert has often related in one form or another, I like getting credit for things. However in a departure from that philosophy, I must admit that this research would not have been possible without the help of many other heroes. Many thanks to:

Professor David Staelin: I'd like to start by thanking my advisor Professor Staelin. I've met a variety of people during the first 26 years of my life and he's in the top-tier when it comes to qualities such as character and creativity, to name a few. He brings a sense of excitement and dedication to his work that I hope to emulate in my own career. I'm particularly grateful for the many discussions that we've had over the years. Regardless of how busy he is, he always makes time to talk when I stop by his office. The advice and stories he has related to me has been invaluable to my own development and has helped prepare me for the exciting times that lie ahead. Thanks Professor Staelin.

Jack Holloway: During this project I had the good fortune to meet Jack. A lot of credit goes to him for getting this research off the ground including developing the original architecture for the software receiver, designing/building the baseband sample/control boards, and the countless number of hours spent consulting with me and working on other engineering projects during development of the instrument. Additionally, a non-negligible part of this contribution was carried out on Saturdays after his official obligation to the project was over. While I'm certain that spending his Saturdays working with me on the receiver was high on his list of fun things to do with his free time (end sarcasm), this further illustrates the kind of person he is. Jack is now serving our country as a 2nd Lt. (ranking as of Aug 07 when we last spoke) in the U.S. Marine Corps and will be entering flight training school in the near future. Take care buddy, I'll always appreciate what you did on this project.

Dr. Dan Bliss: Dan is another example of my good fortune in working with talented people during this research. Dan is on the senior technical staff (as of this month, congrats Dan) at Lincoln Laboratory and would often make the drive from Lincoln to campus in order to discuss research with our wireless group. Thanks Dan for taking the time out of your busy schedule to make this trip so many times, for your many helpful suggestions during these meetings, for responding to countless emails, for participating as a member of my thesis committee, and of course for all those lattes you bought us during our Stata chats.

Prof. Vincent Chan: I'd additionally like to thank Prof. Chan for taking the time to be a part of my thesis committee and meeting with me on several occasions to talk about research and other interesting topics. I enjoyed our conversations.

Sanjit Biswas and ROOFNET team: for providing us with equipment and software that we utilized as the core component of our channel sounding (transmitter-end) system. Much thanks to Sanjit for meeting with me on several occasions to get this sounding equipment up and running. Best of luck to him and the rest of the group in their future research and projects.

Al McGurl and Bill Gibbs: for helping me with many projects that were vital to getting this research moving including securing access to the roofs on Buildings 26/36, providing us with the van for our experiments, arranging the installation of a roof rack on that van, building/installing the antenna rack on top of our receiver (see Figure 6-2 for this example of Bill's craftsmanship which is far superior to my own), letting me borrow their tools on numerous occasions (see wet/dry vac, cordless drill, wood clamps, etc), and rescuing my equipment from the tow truck last fall. Thanks guys I really appreciate all your help.

Lourenco Pires: for lending me test equipment on numerous occasions that

William Hajjar (MIT Parking): for allowing me to park my measurement equipment across campus without fear of accruing a small fortune in parking tickets.

MIT and Cambridge Police: for believing me on numerous occasions that I was running experiments.

Cambridge Pedestrians: for providing me with a whole spectrum of facial expressions.

Seung E. Lee: for encouragement utilizing the technique known as reverse psychology.

Pippen: for spending so much time with me and the laptop, and all the interesting conversations we had at 271 Summer, 60 Wadsworth, and 70 Amherst.

Edgar Gonzalez: for repeatedly beating me in squash. I'll never meet anyone quite like you again man. Thanks for being a good friend.

The good people whom first contact was made in the 80's and 90's: Tom, Phyllis, Paul, Harold, Ines, Dale, Brad, Cleave, Wayne, Pat, Jay, Lucy, Evelyn, Chris, Richard, Courtney, Brian, Kyle, Zach, Loren, Scott, Darren

The good people whom first contact was made in the 21st century: Steve, Virginia, Sara, Leigh-leigh, Charlie!!, Charles, Jean, Goksel, Akshay, Shubham, Arkansas(Vasanth)

Margaret-Virginia Stringfellow Herring: Well these are the last words that I'll be typing into this thesis. Lets be honest, there's been a lot of conversation over the last couple years about this or that malfunctioning and a few conspiracies here and there but in the end we, like Shackleton before us, persevered. Personally I would attribute it to our fortitude. Sure historians will probably look back and give credit to Thomas Edison, but I as well as

yourself know that it was you that held up the other end both figuratively and literally. My point being that you actually did lift the receiver on and off the van with me literally hundreds of times. Looking back I don't think you particularly enjoyed doing this which brings me to the point I'm trying to make, I love you Maggie. Thanks for all the times you put aside your own work (including studying for your qualifiers) to walk over to the Stata loading dock to help me with the equipment, for enduring some cold trial runs last winter, and for the enumerable number of sacrifices that you made. The credit for this work goes in large part to you. Thanks to TLOML.

Contents

List of Figures

19

List of Tables

Chapter 1

Introduction

In recent years it has been found that proper deployment of multiple antennas at both the transmitter and receiver can increase the capacity of the wireless link [1]-[4]. Such a system, referred to as Multiple-Input Multiple-Output (MIMO), takes advantage of orthogonal spatial sub-channels formed in multipath environments by simultaneously communicating over each sub-channel, a technique known as spatial multiplexing [6]. This technology coupled with diversity and beam-forming techniques has driven an increased commercial interest in multiple-antenna systems. Given this trend it has become increasingly important that we understand the propagation characteristics of the environments where this new technology will be deployed. In particular the development of low-cost, high-performance system architectures and protocols is largely dependent on the accuracy of available channel models for approximating realized propagation behavior.

The first contribution of this thesis is a methodology for the modeling of wireless propagation in multiple antenna systems. By defining the wireless channel as the complex narrow-band channel response $h \in \mathcal{C}$ between two devices, we characterize the important degrees of freedom associated with the channel by modeling it as a function of its path-loss, multipath/frequency, time stability, spatial, and polarization characteristics. Given this channel model we have devised a series of experiments associated with each channel parameter that aims to explore its structure over a diverse set of propagation environments. More specifically we will be looking at

outdoor propagation environments with link lengths on the order of tens of meters to several kilometers. It is in this environmental regime where many networks utilizing multiple-antenna technology will operate in the near future, e.g. 802.11 (WiFi) and 802.16 (WiMax).

In order to realize these experiments we have developed a Channel-Data Collection System (CDCS). The CDCS includes an eight-channel receiving system, WiFi channel sounders, antennas, system control software, database management utilities, a GPS tracking system, and infrastructure for system mobility. The equipment operates over a bandwidth of 20 MHz centered at 2.4 GHz. Additionally a collection of algorithms has been developed for extracting and estimating the desired channel information from the raw data collected by our system.

We begin this thesis in Chapter 2 by motivating the utilization of multiple-antenna systems in wireless communication. Following this introduction we present our modeling methodology in Chapter 3. The Channel-Data Collection System (CDCS) and its associated performance analysis is presented in Chapter 4. Next in Chapter 5 we present the channel extraction and estimation algorithms that we have built which provide channel estimates from the raw data sets collected by our system. In Chapter 6 we present our work associated with the path-loss characteristics of the wireless channel. In particular we discuss the details of the experiments, models, and results associated with this channel parameter. Similarly we discuss our work associated with the frequency, stability, and spatial characteristics in Chapters 7, 8, and 9 respectfully. Lastly, in Chapter 10 we outline the conclusions of this research and provide suggestions for future work.

Chapter 2

Multiple Antenna Systems

In this chapter we motivate the use of multiple antenna systems in wireless communications. Specifically we introduce Multiple-Input Multiple-Output (MIMO) technology which has increased interest in multi-antenna design. Additionally we discuss the more traditional techniques of spatial diversity and beam-forming.

2.1 MIMO System Model

A Multiple-Input Multiple-Output (MIMO) wireless communication system by definition deploys multiple antenna elements at both ends of the link. The instantaneous narrow-band channel for a MIMO system can be modeled as,

$$y = Hx + n$$

where y ϵ $\mathcal{C}^N$ and x ϵ $\mathcal{C}^M$ denote[1] the signals received at the N receive antennas and the signals transmitted from the M transmit antennas respectfully. Here,

$$n \sim \mathcal{CN}(0, \sigma_n^2 I_N)$$

represents the system and channel noise[2] [3]. The channel matrix, H ϵ $\mathcal{C}^{NxM}$, represents

---

[1]$\mathcal{C}^N$: N-dimensional complex space
[2]$\mathcal{CN}(\mu, \Lambda)$: Circular symmetric complex gaussian distribution, mean μ, covariance matrix, Λ
[3]I_N: NxN Identity Matrix

the channel between each pair of transmit and receive antennas. This model can be extended by allowing the channel matrix H to vary as a function of frequency and time.

2.2 Channel Matrix Decomposition

2.2.1 Parallel Spatial Channels

Consider now the Singular Value Decomposition (SVD) of the channel matrix, H,

$$H = U\Sigma V^H$$

where U ϵ $\mathcal{C}^{NxN}$, V ϵ $\mathcal{C}^{MxM}$ are unitary rotation matrices, Σ ϵ $\mathcal{R}^{NxM}$ is a rectangular diagonal matrix whose diagonal elements are all non-negative, and N,M are the number of receive and transmit antennas respectfully [4]. We can make a change of basis by defining:

$$\widehat{y} = U^H y$$

$$\widehat{x} = V^H x$$

$$\widehat{n} = U^H n$$

The MIMO system model can then be expressed as:

$$y = Hx + n$$

$$\Rightarrow y = U\Sigma V^H x + n$$

$$\Rightarrow U^H y = \Sigma V^H x + U^H n$$

$$\Rightarrow \widehat{y} = \Sigma \widehat{x} + \widehat{n}$$

$$\Rightarrow \widehat{y_i} = \sigma_i \widehat{x_i} + \widehat{n_i} \qquad \text{for i =1,2,...,K}$$

---

[4] V^H: Conjugate Transpose of matrix V

where,

$$K = \min(M, N)$$

and

$$\sigma_1 > \sigma_2 > \text{.......} > \sigma_K$$

are the K non-zero singular values of H. Here we see that the MIMO channel can be broken into K orthogonal spatial sub-channels which we refer to as eigenmodes [6].

2.3   Spatial Multiplexing

Given the equivalence of the MIMO channel to K orthogonal spatial sub-channels we can consider communicating over each of these eigenmodes simultaneously. The Shannon Capacity of an instantaneous Single-Intput Single-Output (SISO) channel, h, is

$$C = \log_2(1 + \frac{P \cdot |h|^2}{\sigma_n^2}) = log_2(1 + SNR) \qquad \text{(bits/s/Hz)}$$

where P is the transmit power constraint of the system and σ_n^2 the total power due to channel noise. By orthogonality we can derive the capacity of the MIMO channel as being equal to the sum over K SISO channels corresponding to the K eigenmodes of the MIMO channel,

$$C = \sum_{i=1}^{K} log_2(1 + \frac{P_i \cdot \sigma_i^2}{\sigma_n^2}) = \sum_{i=1}^{K} log_2(1 + SNR_i) \qquad \text{(bits/s/Hz)}$$

where P_i is the power allocated to the ith eigenmode such that the total power constraint (P) is met,

$$\sum_{i=1}^{K} P_i \leq P$$

and SNR_i refers to the Signal-to-Noise ratio of the ith spatial sub-channel. Here we see a potential benefit from the deployment of MIMO systems in the form of an increase in channel capacity. Spatial Multiplexing then refers to the process of transmitting independent data streams over these orthogonal sub-channels (eigenmodes) in order

to increase the data rate of the link.

2.3.1 Power Allocation

The problem of allocating power to orthogonal sub-channels (frequency, time, spatial) is solved optimally with respect to total channel capacity using the waterfilling allocation [6],

$$P_i = \max(c - \frac{\sigma_n^2}{\sigma_i^2}, 0)$$

with c defined such that the total power constraint P is met.

High SNR vs Low SNR Regimes

In the low SNR limit, capacity is power limited and the water filling powers will result in power allocation only to only the strongest eigenmode. In the other extreme as SNR becomes large any difference between eigenmodes will be negligible and the optimal waterfilling power allocation will be equal across modes [6].

Uninformed Transmitter (UT) vs Informed Transmitter (IT)

MIMO systems can be categorized based on the amount of channel information available at the transmitter. In one extreme the transmitter knows the channel matrix, H, exactly in which case it can optimally allocate power to the eigenmodes according to the waterfilling powers. In the other extreme no channel information is known at the transmitter so that it is optimal to allocate equal power across antenna which is equivalent to equal power distribution to each of the eigenmodes [7].

2.3.2 Equal Allocation Capacity

With respect to spatial multiplexing the high SNR regime is of most interest. As described above it is in this regime that it is optimal to allocate power to multiple spatial channels. The MIMO channel capacity in the case of equal power allocation

is then [6],

$$C = \sum_{i=1}^{K} log_2(1 + \frac{P \cdot \sigma_i^2}{M\sigma_n^2}) = log_2(|I_N + \frac{P}{M\sigma_n^2}HH^H|) \qquad \text{(bits/s/Hz)}$$

2.4 Additional Benefits of Multiple-Antenna Systems

Before spatial multiplexing was developed, multiple antenna systems were traditionally utilized in other ways.

2.4.1 Diversity

In a rich multipath scattering environment the narrow-band channel can be modeled as having a complex gaussian distribution. In this setting there exists a non-negligible probability that the attenuation of the channel is prohibitively high, resulting in a low channel capacity. Consider then deploying multiple antennas and spacing them in such a way that the channels between each of them and the other link end can be considered independent. Such a strategy increases the probability of having at least one link with sufficient Signal-to-Noise ratio. In fact this probability increases exponentially with N · M, where N and M are the numbers of antennas at the receiver and transmitter, respectfully. Such behavior is referred to as spatial diversity. Given this definition, diversity can be obtained with multiple antennas at one or both link ends.

2.4.2 Beamforming

Beamforming is a method used in multiple antenna systems to focus energy in certain angular directions at either the transmitter or receiver. This is carried out by properly phasing the data streams at each antenna relative to one another. With this method a relative power gain is achieved in certain directions whose maximum achievable gain is proportional to N·M, i.e. the product of the number of receive and transmit

31

antennas. Beamforming is also achievable with multiple antennas at one or both link ends.

2.4.3 Trade-offs

The optimal way to utilize multiple antennas in such a system depends on the propagation environment [20]. The preferred strategy is dependent on the requirements of the system. Each link end, transmitter and receiver, can be classified as being either directive or diverse. A directive link end is one in which the dominant signal paths arrive (or depart) from a small number of directions. Conversely, in a diverse link end signals arrive (or depart) from a large number of directions. If the propagation environment is directive at both link ends then beamforming is the preferred use of the antennas. In this case there is no spatial diversity or multiplexing gain to be exploited. In the case of one diverse and one directive link end diversity is often the preferred mode of operation since diversity can be used at the diverse link end. Lastly, in the case of diversity at both link ends, spatial multiplexing is the preferred method of operation as a capacity gain is possible.

Chapter 3

Channel Model and Methodology

In this chapter we present a methodology for modeling wireless propagation for multiple antenna systems. Specifically we consider the problem from the perspective of protocol designers and network/system engineers. The first component of the methodology is a characterization of the important degrees of freedom associated with the wireless channel, particularly those required to ensure intelligent engineering and design decisions. The second component of the methodology reduces these channel parameters to a set of metrics that provide sufficient information to the engineer. Specifically, we characterize the set of design decisions that depend on each channel parameter and its associated metrics. The final component considers the role of environmental information in modeling and prediction of these metrics. Given that complete knowledge of the environment is practically never available, we consider a parametrization of the environment that is high in information content and potentially measurable.

3.1 Channel Parametrization

In this section we characterize the important degrees of freedom associated with the wireless channel with respect to the design and engineering of multiple antenna wireless systems. We start by defining the channel as the input-output relationship

33

of a wireless system which at the lowest level can be described as,

$$y(t,f) = x(t,f) \cdot h(t,f,s_T,s_R,\Omega_T,\Omega_R,\theta_T,\theta_R) \tag{3.1}$$

where the signal received y, is the transmitted signal x, scaled by the channel h, which is a function of time t, frequency f, transmitter position s_T, receiver position s_R, direction of transmission departure Ω_T, direction of arrival at the receiver Ω_R, transmitted polarization θ_T, and received polarization θ_R. The relation in 3.1 is referred to in the literature as the double-directional channel model [25] and it gives a complete description of channel propagation. In practice however, modeling channel behavior to this level of detail is not feasible. Instead our approach is to model individually the power attenuation, frequency, time, spatial, and polarization characteristics of the channel in such a way that the behavior of these parameters applicable to system/protocol design are efficiently captured. We now define these model parameters.

3.1.1   Power Attenuation/Large-Scale Fading

The first parameter of importance is the power attenuation of the channel. This refers to the loss in power due to propagation between transmitter and receiver. Fading of this type is generally broken into two categories, path-loss and shadowing, corresponding to attenuation due to propagation length and scattering objects, respectively.

3.1.2   Frequency/Multipath

The second channel parameter is the frequency structure of the channel. In multipath/scattering environments distinct propagation paths constructively and destructively interfere with one another at the receiver. This delay pattern in the time domain results in a frequency dependent channel response.

34

3.1.3 Time/Stability

The time characteristics are the third channel parameter. As objects within the propagation environment move, even with stable link-ends, the channel response changes. This occurs as small movements of scatterers introduce small propagation delays of the signal paths associated with those scatterers. At the receiver this results in the superposition of propagation paths with different relative phases which generally results in a distinct channel response.

3.1.4 Spatial

The fourth channel parameter is the spatial degrees of freedom. This refers to the dependence of the channel on small spatial displacements (on the order of the carrier wavelength) at both the transmitter and receiver. This structure is driven by the joint angular spectrums at each link-end as small spatial movements result in angle-dependent phase shifts of the arriving multipath components.

3.1.5 Polarization

The final parameter is the polarization structure of the channel. More specifically this refers to the behavior of the channel in coupling the three orthogonal polarizations.

3.2 Design Decisions and Channel Metrics

We now motivate the importance of these channel parameters in protocol and system design. In what follows we describe a general set of design decisions that depend on each channel parameter and an associated set of metrics for efficiently quantifying their behavior.

3.2.1 Power Attenuation

Design Decisions/Parameters

1. Wireless Node Density ($\frac{nodes}{m^2}$)

2. Transmit Power (dBm)

Metrics

1. **Path-Loss Coefficient** (α): Path-loss refers to the average signal power attenuation as a function of the propagation path length between transmitter and receiver. In free space the electric far field at the receiver due to a signal originating from the transmitter is inversely proportional to the distance between them. The power then decays proportionally to the squared path distance, r, in free space,

$$P_r \propto \frac{P_t}{r^2}$$

where P_r and P_t are the signal power at the receiver and transmitter respectfully. However, the propagation environment in practice contains objects that reflect, scatter, or absorb the signal radiated from the transmitter. This often results in a path-loss that is higher than that of free space attenuation,

$$P_r = C \cdot \frac{P_t}{r^\alpha}$$

where $\alpha > 2$ and C is a constant environmental attenuation factor. A useful metric then for quantifying this behavior is the path-loss coefficient α.

2. **Shadowing-Level** (σ_S): While α gives a measure of the mean-attenuation as a function of distance, the shadowing-level (σ_S) is a measure of the deviation from this mean,

$$\sigma_S = \sqrt{\mathrm{E}[(|h|^2 - C \cdot \frac{P_t}{r^\alpha})^2]}$$

where $|h|^2$ is the squared amplitude of the channel.

3.2.2 Frequency/Multipath

Design Decisions/Parameters

1. Wideband system: Equalizer filter length (seconds)

2. OFDM system: Channel bandwidth (MHz)

3. MIMO system: Computational Complexity ($\frac{\text{SVD operations}}{MHz}$)

Metrics

1. **Delay Spread** (τ_{DS}): The difference in propagation path length (or equivalently delay) between the shortest and longest propagation paths. More specifically delay spread is calculated as a function of threshold C,

$$\tau_{DS}(C) = \max_{i,j \epsilon S_C} |d_i - d_j| \ [\text{m}]$$

   where d_i is the propagation path length (meters) of the ith significant multipath component (MPC) and,

$$|h_i|^2 > C \Rightarrow i \epsilon S_C$$

   where $|h_i|^2$ is the squared amplitude of the ith MPC. This describes the delay spread as being calculated over the set S_C of significant (in the power sense) MPCs.

2. **Coherence Bandwidth** (B_c): The frequency domain equivalent to delay spread is the coherence bandwidth. The coherence bandwidth is defined as,

$$B_c(C) = \frac{c_{light}}{\tau_d(C)} \ [\text{Hz}]$$

   where $c_{light} \approx 3 \cdot 10^8 \ \frac{m}{s}$. Here we see that the coherence bandwidth is inversely proportional to the delay spread and describes the de-correlation length in the frequency domain. Channels in which the coherence bandwidth is larger than that of the signal bandwidth are referred to as 'flat fading' channels. Otherwise

they are referred to as 'frequency selective' since the channel response is different over the various frequencies being utilized in the communication band.

3. **Small-Scale Fading Distribution**: Specifically this refers to the expected statistical distribution of the narrow-band channel h ϵ C, $f_h(x)$. Widely utilized distributions for modeling the behavior of —h— include the Rayleigh and Rician distributions.

3.2.3 Time/Stability

Design Decisions/Parameters

1. Channel State Information (CSI) Update Rate ($\frac{\text{Estimations/Flops}}{s}$)

Metrics

1. **Time Coherence Length** (T_c): The time coherence length of the channel is a measure of how long the channel can be expected to be stable. We can measure this as,

$$T_c(V_m, V_p, p) = t \text{ [sec]}$$

$$\text{s.t. } t = \max_{\tilde{t}} \text{ Prob}(A \cap B) = p$$

where the events A and B are defined as,

$$A = \{\frac{1}{V_m} \leq \frac{|h_o|^2}{|h_{\tilde{t}}|^2} \leq V_m\}$$

$$B = \{-V_p \leq (\angle h_o - \angle h_{\tilde{t}}) \leq V_p\}$$

where h_o and $h_{\tilde{t}}$ are realizations of the same channel separated by $\tilde{t}$ seconds in time. Here the time-coherence length is defined as a function of a tolerance V_m (magnitude) and V_p (phase) in which the channel can change before being considered different.

38

3.2.4 Spatial

Design Decisions

1. Antenna Array Topology/Spacing

2. Number of Antennas per node

Metrics

1. **Channel Capacity**: see section 2.3

2. **Spatial Coherence Length** (S_c): This is the same measure as the time co-herence length but applied to spatial displacement.

3.2.5 Polarization

Design Decisions

1. Polarization-Mix of antenna elements

Metrics

1. **Cross-Polar Discrimination (XPD)**: XPD is defined as the cross-polar dis-crimination of the channel. This refers to the tendency of the channel to isolate the orthogonal polarizations. By orthogonal polarizations we refer here to the horizontal (average over two horizontal polarizations) and vertical polarization basis. Formally then we can define XPD as,

$$XPD_{VH} = \frac{P_{VH}}{P_{VV}}$$

$$XPD_{HV} = \frac{P_{HV}}{P_{HH}}$$

where P_{ij} (i,j ϵ {H,V}) is the average power received by elements with po-larization j from elements that transmit with polarization i. Note that there are two XPD values specified for each direction the isolation/coupling takes

place. These parameters are not equal in general because the corresponding paths are different. An XPD of zero then corresponds to a channel in which the orthogonal polarizations are perfectly isolated. Conversely, an XPD of one corresponds to a channel that couples equal energy to each polarization. The XPD of the channel is a relevant parameter for MIMO systems. If both XPD values are zero, i.e. perfect polarization isolation, then the two polarizations (horizontal/vertical) can be treated as orthogonal spatial subchannels and be used accordingly in a MIMO system. If the XPD is closer to unity then more detailed information of the polarization structure is needed in order to access its MIMO-relevant quality.

2. **Cross-Polarization Correlation**: A more precise description of the MIMO-relevant polarization structure of the channel includes the correlation coefficient between orthogonally polarized antenna elements. In cases where there is high coupling between such channels the possibility remains that they may be uncorrelated. In such circumstances the orthogonal polarizations of the channel can still provide spatial multiplexing.

3.3   Environmental Parametrization

The behavior of each channel parameter is dependent on the environment. If everything about the environment was known, including the exact positions and dynamics of every scatterer and link-end, then channel characteristics could be precisely calculated. The double-directional channel model (3.1) and various ray-tracing techniques assume such complete knowledge of the channel environment. In practice however, such a detailed description of the environment is generally impossible to acquire. Instead we consider reducing the environment space to a set of potentially measurable environment parameters that are high in channel information content. We now briefly describe some candidate link/environment parameters that meet these qualifications:

1. Link-Length: The link-length is formally defined as the distance between trans-

mitting and receiving nodes over a wireless link. In general we would expect channel behavior to be sensitive to this parameter. For example as will be discussed in the following chapters we would expect power attenuation, multipath richness, polarization coupling, channel instability, and spatial diversity to all increase with increased link-length.

2. Link Type (Ground-to-Ground vs. Air-to-Ground links): Here we define link type as the relative height between antennas at each end of the wireless link. While this parameter is generally categorized as a continuous spectrum of height differentials, we consider breaking link type into two regimes, namely: Ground-to-Ground and Air-to-Ground links. The former corresponding to links in which the antennas at each link end are mounted with nearly the same height (< tens of wavelengths) and the latter being the case in which the antenna at one link end is mounted well above the other. As we will see in the following chapters the proper model and/or model parameters for describing path-loss, stability, and multipath channel behavior is highly dependent on the type of link.

3. Line-Of-Sight (Non-Line-Of-Sight (NLOS) vs. Line-Of-Sight (LOS)): A wireless link is considered LOS if the antennas at each link end are physically visible to one another, otherwise it is considered NLOS. As we will see in the following chapters the presence of LOS can often result in there being present a multipath component that dominates the channel response. We will see in the following chapters that if this is the case different models that account for this dominant component will be necessary for accurately describing channel behavior.

4. Physical Parameters: As described above it is of interest to isolate physical environmental parameters for inputs into channel models that are both easily measurable and provide insight into channel behavior. Here we list some examples of such parameters that will be further explored in the subsequent chapters:

    (a) Building Density: In urban/suburban environments this serves as an ap-

proximation to the richness of the scattering environment. As we will see channel behavior such as path-loss, multipath, and spatial structure is correlated to this physical parameter.

(b) Traffic Rates: This serves as an approximation to the instability of the scattering environment and can then be used as input into a channel stability model.

Chapter 4

Channel-Data Collection System

The Channel-Data Collection System (CDCS) is a set of instrumentation and software that functions as a system for collecting large amounts of wireless channel data. The CDCS presented here was developed specifically for the research contained in this thesis. The system blocks that comprise the CDCS are an eight-channel software receiver, channel sounder (WiFi transmitter), collection of antenna elements, software packages (distributed across several devices – laptop, lab network, onboard receiver PC) for system control and database management, a GPS tracking system, and additionally infrastructure for system mobility. See Figure 4-1 for an overview of the system components.

4.1 Software Receiver

The software receiver introduced in this thesis is designed to sample the 33-MHz band centered at 2.422 GHz, which is allocated as channel 3 of the 802.11b wireless standard. The receiver synchronously samples this band at 67 MHz at eight configurable antenna elements for 1-msec continuous bursts. Each burst of channel data, referred to as a snapshot, is then downloaded to an on-board PC where it is stored until it can transferred to the database for post-collection processing. The receiver can be broken into the following functional blocks: RF Front-End, Baseband Sampling/Control, CPU–Control/Storage, Clock Generation/Distribution, and Power Supply. The re-

43
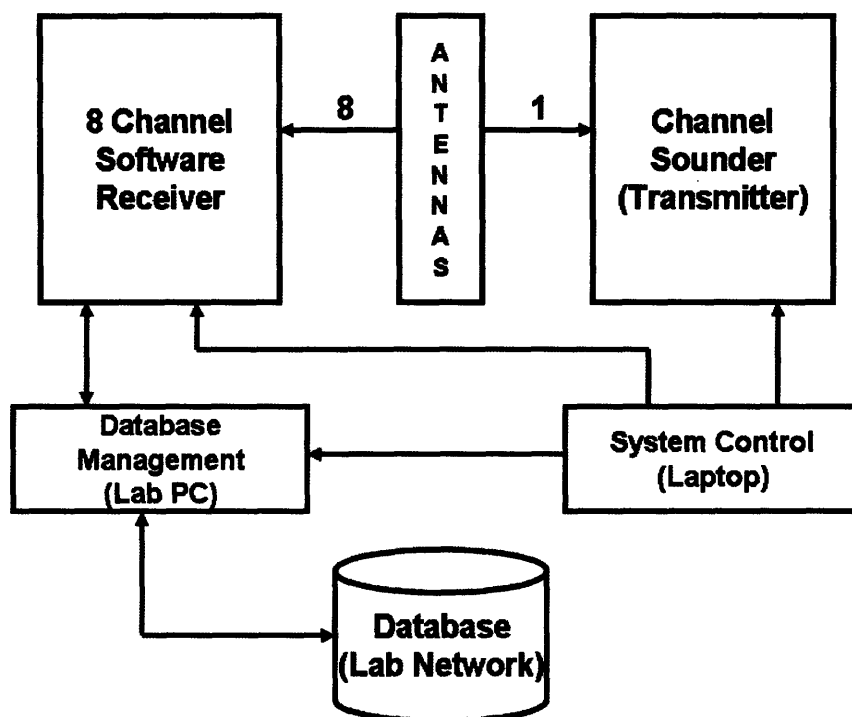
Figure 4-1: The Channel-Data Collection System

ceiver is housed in a 3'x3'x1' aluminum case. Figure 4-2 displays an image of the software receiver with the case cover and antennas removed. Additionally Figure 4-3 presents the block diagram of the receiving system.

This device was co-developed and constructed by the author and Jack Holloway. Jack's invaluable contributions to this engineering project include developing the original architecture for the software receiver, designing/building the baseband sample/control boards, and a countless number of consulting hours with the author throughout development.

4.1.1 RF Front-End

The RF front-end of each channel is comprised of an antenna lead, two low-noise amplifiers, and a mixer housed in an RF shielding box. The mixer on each channel is driven by the same local oscillator at a frequency of 2.406Ghz. See Figure 4-4 for a diagram of the RF front-end subsystem and Table 4.1 for the corresponding part
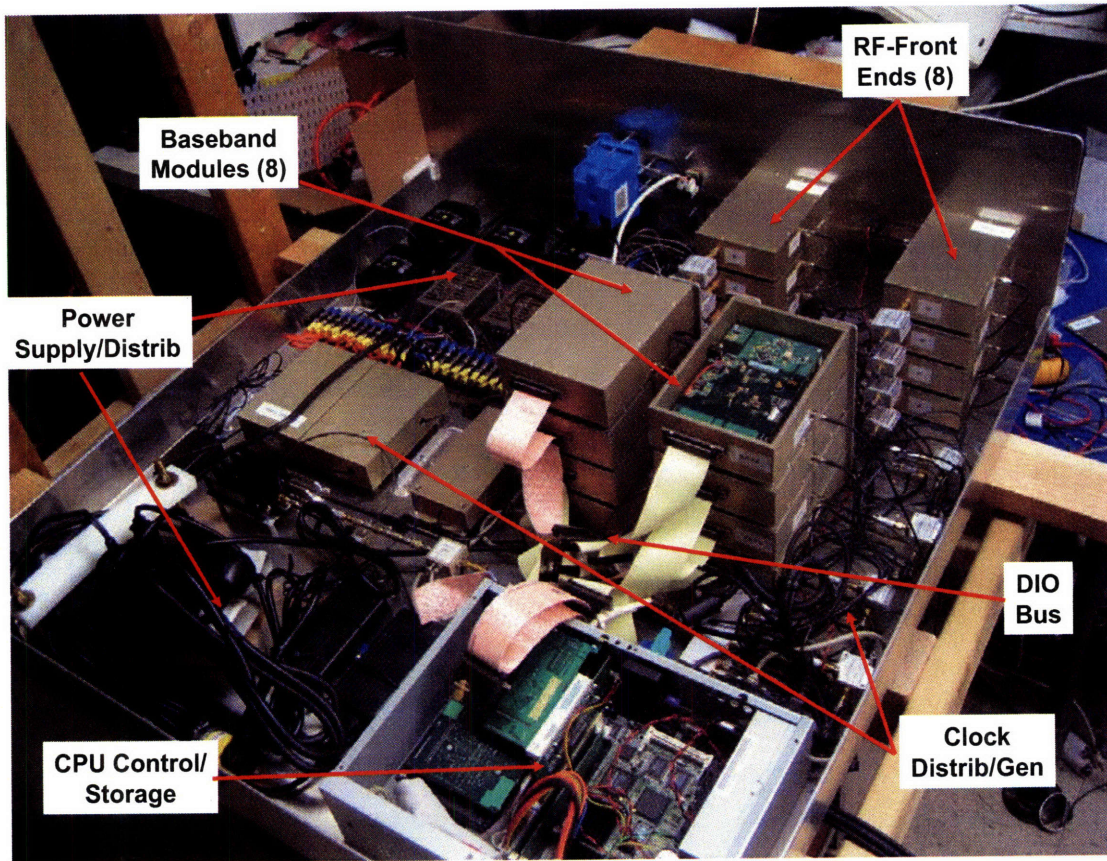
Figure 4-2: The eight channel software receiver: With case cover and antennas removed

descriptions.

4.1.2 Baseband Sampling and Low-Level Control

Baseband sampling and the lowest level of receiver operation on each channel is handled by custom built sampling/control boards. Each board is populated by a 30-MHz low-pass anti-aliasing filter/amplifier, 12-bit analog-to-digital converter (ADC), a 65-kSample FIFO buffer for temporary data storage, and Field-Programmable Gate Array (FPGA) controller. The eight printed circuit boards (PCBs) are individually housed in RF shielding boxes. See Figure 4-5 for a diagram of a single baseband module.
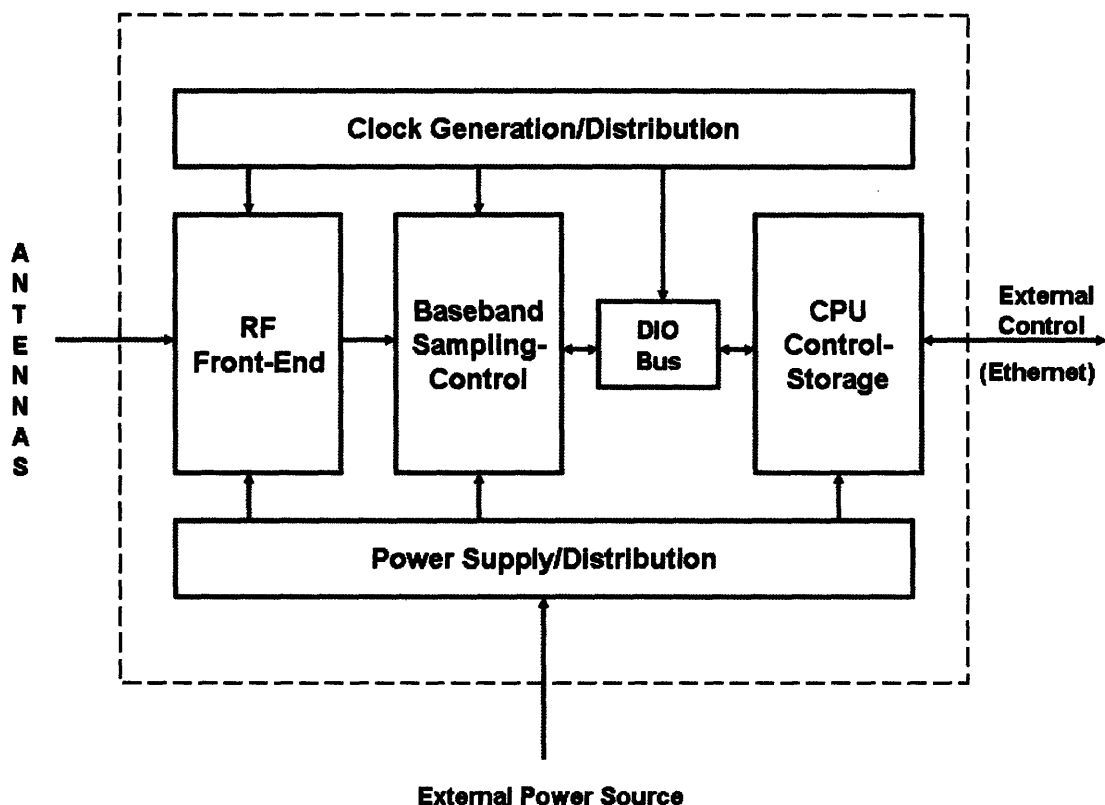
Figure 4-3: The Software Receiver

Analog Front-End

Before sampling, the signal supplied from the RF front-end is amplified to the appropriate level for interfacing with the ADCs. In addition a low-pass filter is applied to prevent aliasing before sampling.

Analog to Digital Conversion

The ADCs (synchronous across eight receive channels) sample the incoming waveform at a rate of 67MSps with 12-bit precision. The amplification in the analog front-end filter is set so that the bottom one to two bits of the sampled waveform correspond to the thermal noise floor of the receiver.
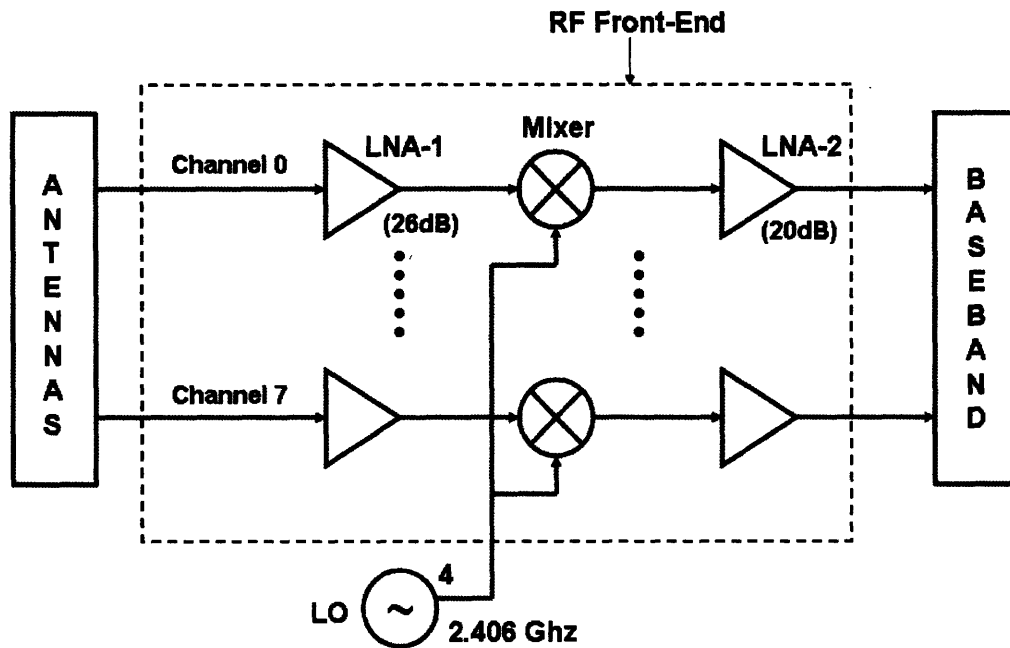
Figure 4-4: The RF-Front End

Sample Buffers

After the signal is digitally sampled the resulting samples are stored in a temporary
FIFO buffer for storage until they can be downloaded to the PC. The buffer's ca-
pacity is 65k 12-bit samples, giving the receiver a total continuous sampling duration
(snapshot length) of approximately 1 msec.

Low-Level Control

FPGAs on the sampling boards implement the lowest level of control by defining a
finite state machine representing the board level operation of the receiver.

4.1.3 Finite State Machine

Instruction Word

Operation of the FPGAs is controlled from the on-board PC, described in the next
section, with an instruction set defined by the firmware loaded on the FPGAs. Each
instruction word from this set is 20 bits wide with the format displayed in Figure 4-6

Table 4.1: RF Front-End Part Descriptions

Part	Specs
Mixer	Clock Input: 2.406Ghz
	Loss: 4.5dB
	1dB Compression: +3dBm
Pre-Mix LNAs	Gain: 26dB
	Noise Figure: 0.6dB
	Freq Range: 2-2.5Ghz
Post-Mix LNAs	Gain: 20dB
	Noise Figure: 2.9dB
	Freq Range: 0.1:1000Mhz

The instruction word is divided into the following sub-words:

1. **ID** (bits 19-16): The top four bits of the instruction word are assigned to the sub-word ID. The ID sub-word signifies which of the 8 receivers the instruction is addressed to. These 4 bits can take on any of 8 valid values (0-7) corresponding to the 8 receive channels. Note the extra bit was left for a possible future expansion of the system to 16 channels.

2. **INST** (bits 15-12): The next four bits of the instruction word are assigned to the sub-word INST. The INST sub-word signifies which of the instruction actions, corresponding to a state of the FSM, are to be carried out. This sub-word can take on any of 5 values corresponding to the 5 FSM states to be discussed shortly.

3. **DATA** (bits 11-0): The final 12 bits of the instruction word are assigned to the sub-word DATA. The DATA sub-word carries data from the baseband module to the CPU. As will be discussed shortly this data can take the form of raw channel samples or synchronization signals between the two devices.

FSM States

The controller finite state machine (FSM) is made up of 5 major states which describe the sequential board-level operation of the receiver. Figure 4-7 displays the state diagram.
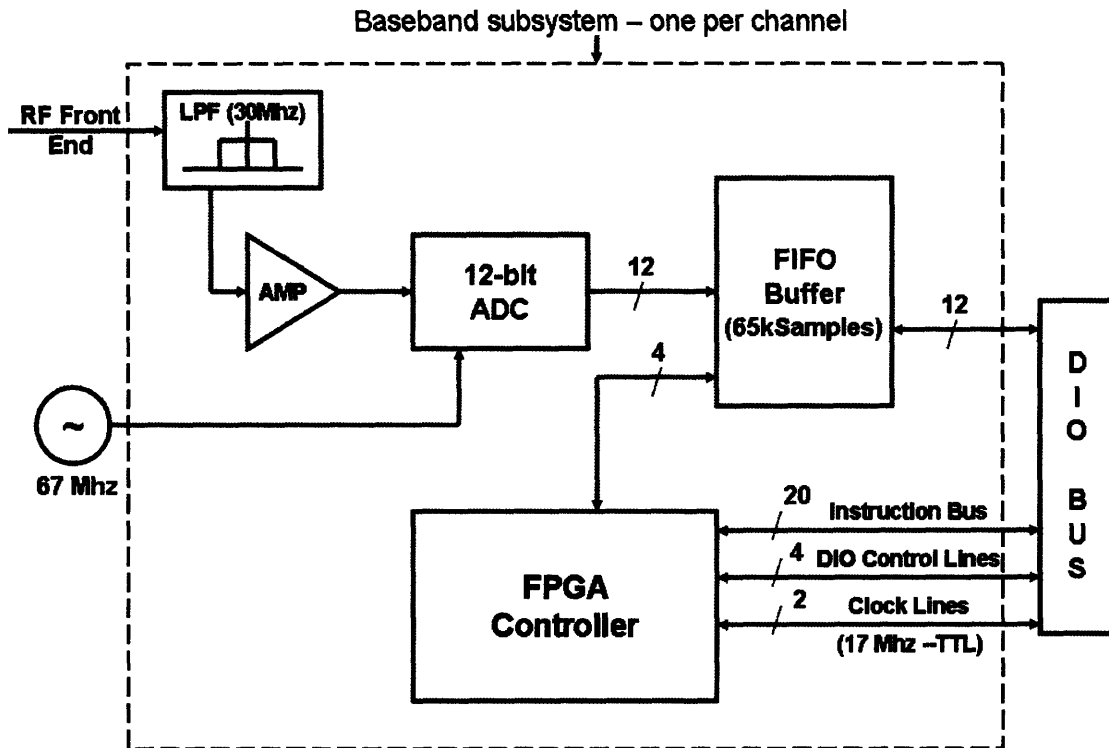
Figure 4-5: The Baseband Sampling-Control Subsystem

RESET (Instruction: 0000)

When the instruction 0000 is placed on the DIO bus, independent of the current ID tag, all connected sampling boards enter the RESET stage. The purpose of the RESET stage is to initialize all the relevant bus lines on all connected baseband modules for the beginning of a sampling sequence. Following the RESET state only the DETECT state may be entered as the next state of operation.

DETECT (Instruction: 1110)

Following the RESET state, receiver operation enters the DETECT state. The purpose of the DETECT state is to verify that each receive channel is working properly and ready for channel sampling. The receive channels are sequentially detected by placing the instruction 1110 on the INST lines (see Figure 4-5) and the individual ID tags on the ID DIO bus lines. As each receiver channel is detected the FPGA of the
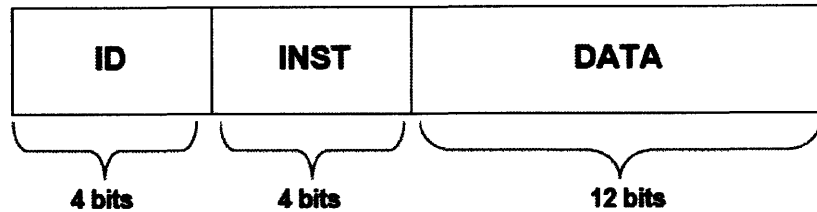
Figure 4-6: The Instruction Word

appropriate board places the message,

$$\underbrace{111....1}_{8bits} | \underbrace{id}_{4bits}$$

on the DATA sub-word of the bus. Here the last four bits, id, refer to the id number of the receive channel being detected. This message allows the CPU controller to know that the detection was successful. If this message is not received then this indicates a hardware failure for that channel.

CEXE (Instruction: 1000)

Following the DETECT state the receiver is ready to collect a snapshot. After detection when the instruction 1000 is placed on the INST lines, regardless of the current ID tag, all connected receive channels enter the CEXE state. Once in the CEXE state the channel begins sampling the incoming baseband waveform on the next clock pulse. The waveform is continuously sampled until the 65KSample FIFO buffer is completely filled.

POLE (Instruction: 0011)

After the CEXE state has been entered the POLE state may be initiated. The purpose of the POLE state is to request the status of the sampling process started by the CEXE state. The receive channels are sequentially poled by placing the word
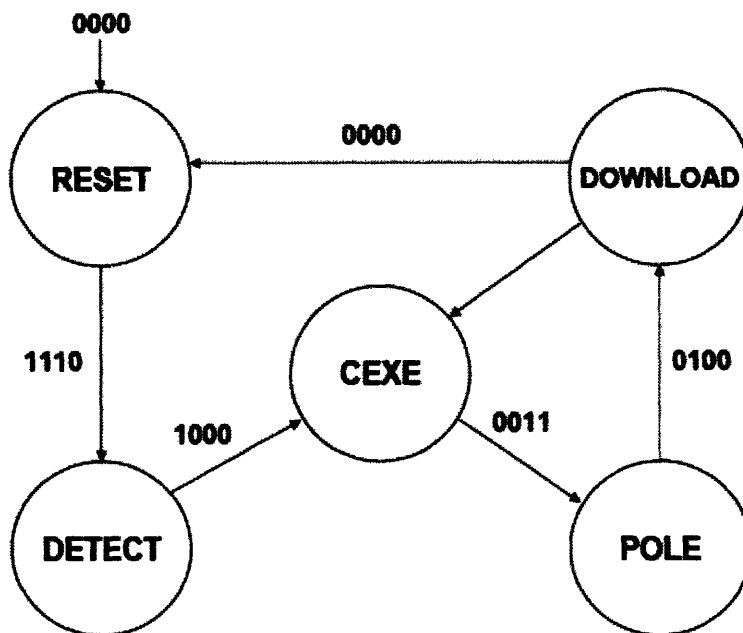
Figure 4-7: The Finite State Machine

0011 on the INST lines and the appropriate ID tag on ID bus lines. Similar to the DETECT state, the word,

$$\underbrace{111....1}_{8bits} | \underbrace{id}_{4bits}$$

will be placed on the DATA lines (see Figure 4-5) if the sampling has completed, meaning a full set of 65K Samples has been stored in the FIFO. If this message is not received then the CPU must continue to reissue a POLE request until it is received. If the message isn't received within a reasonable amount of time (on the order of a second) then this signifies improper functioning of that baseband module.

DOWNLOAD (Instruction: 0100)

After the POLE state is completed successfully the sampled channel data contained in the FIFO buffers is ready to be downloaded to the PC. The data from each receiver chain is sequentially downloaded by placing the word 0100 on the INST lines and the

appropriate ID tag on its respective lines. Once the transfer is initiated a new FIFO output (sample) is placed on the data lines every DIO Bus clock pulse (17 Mhz). After the data on all receivers is downloaded the receiver may re-enter the CEXE state for sampling of more channel data or enter the RESET state for reconfiguring the subset of channels used for the next snapshot.

4.1.4 CPU–Control/Storage

On-board the receiver is a compact 700-Mhz Pentium III PC. The PC's function is to control receiver operation by issuing commands from the instruction set, defined by the FPGA FSMs, to the baseband modules over the DIO bus. Additionally the PC is responsible for all higher level control of the receiving system and for acting as an intermediate storage facility for the channel data. See Figure 4-8 for a diagram of this subsystem.
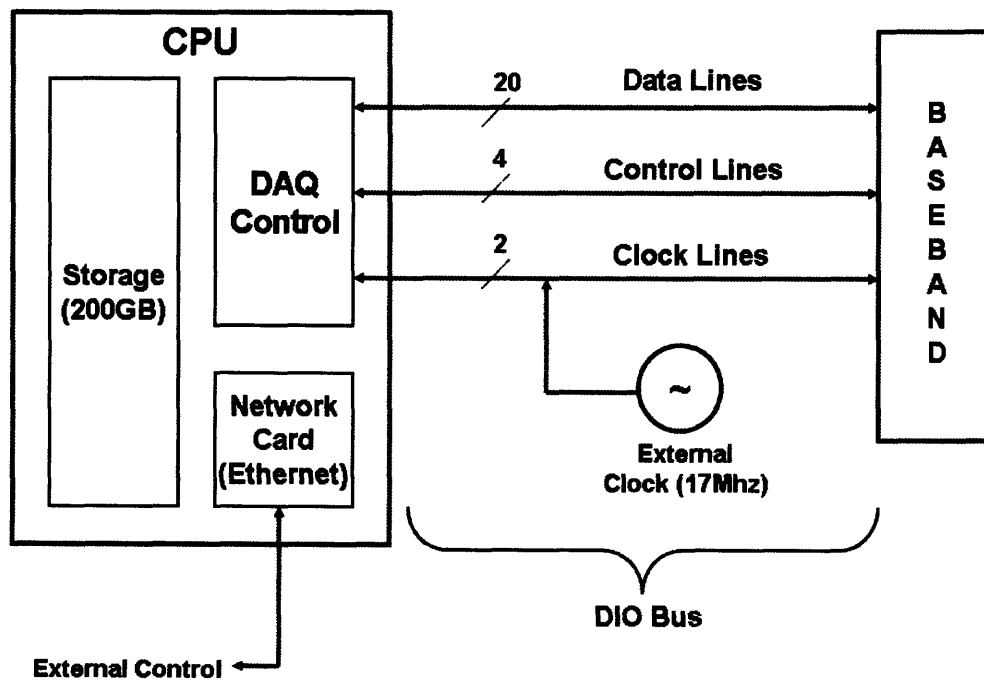
Figure 4-8: The CPU Control/Storage Unit and DIO Bus

DAQ and DIO Bus

The PC communicates with the baseband modules via a NI-6534 Data Acquisition Card (DAQ). The DAQ implements a protocol for communication over a 68-pin bus that the sampling boards have been designed to interface with. The PC interface then is realized by writing software that calls driver functions supplied by the DAQ.

The DAQ and baseband modules are physically connected by a 68-pin SCSI cable. A 1-to-8 bus connecting DAQ to each individual PCB is realized by using one 1-to-8 SCSI cable and eight 1-to-1 SCSI cables.

CPU Controller Software

The DAQ driver used in this implementation is written in C and provides a set of functions for interfacing the computer with the PCBs. The DAQ divides the 32 data lines of the DIO bus into 4 divisions of 8 pins each labeled A-D. As seen in Figure 4-8 our system only requires the use of 20 of these data lines. The protocol is defined so that each division may be individually assigned to at most one of two groups. Each group is then assigned as being dedicated to either input or output operations. Specifically the DAQ-defined Burst Protocol is used here, which is a synchronous clocked protocol. Each group assignment is allocated three control lines, ACK, REQ, CLK. Given that there are two groups, we see in Figure 4-8 there are a total of 4 control lines (ACK1, ACK2, REQ1, REQ2) and two clock lines (CLK1, CLK2). A transfer operation takes place on the first positive CLK edge after the two devices (here DAQ and a baseband module) have exchanged REQ and ACK signals.

The CLK signal can be driven by either an external or internally (DAQ) generated clock with a maximum cycle frequency of 20 Mhz. For this application it was necessary to use an external clock as discussed in Section 4.1.5. The clock cycle of the external clock is 17 Mhz.

Given this interface, the CPU controller software operates by sequentially stepping through the FPGA-defined FSM. Starting at the RESET state the appropriate messages are passed back and forth until the DOWNLOAD state is reached, at which

point the data is downloaded into the PC's memory and then written to the hard disk onboard the CPU.

Operating System

Originally the architecture called for running linux but incompatibilities between the available DAQ drivers resulted in using a stripped-down version of Windows 98 as the operating system. Cygwin, a linux emulator which runs on top of Windows, has been installed for scripting and communication purposes.

Storage

After the channel samples have been retrieved from the PCB FIFO buffers into the PC's memory they are stored to hard disk in a binary format file for temporary storage. A 200-GB hard disk has been installed in the PC for this purpose. With each time snapshot (per receiver) taking 128KB of disk space, this allows room for over 2^{20} snapshots, after accounting for OS/software space, which is more than sufficient.

4.1.5 Timing and Synchronization

The mixers, ADCs, and DIO Bus of the receiver are each driven by external clock sources. In order to meet timing and synchronization constraints each device is driven by the same source. The source operates at 2.406Ghz.

Mixer Source

With the source operating at the correct frequency (2.406Ghz) for the mixers, the source signal is supplied directly to each of eight RF Front-Ends after being split with a 1-to-8 power divider. With each channel running from the same LO the baseband waveforms are phase and frequency locked across each channel.
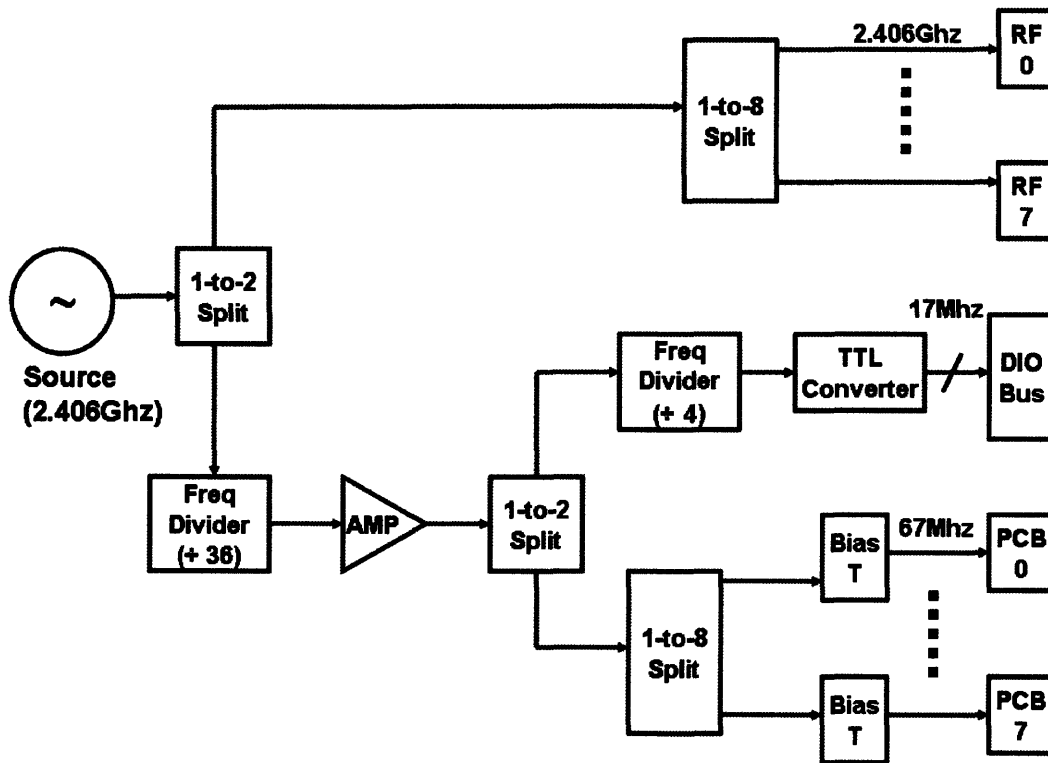
Figure 4-9: Clock Distribution System

Sampling Clocks

The ADCs on the sampling boards are driven by the same LO as the mixers in order to simplify sampling rate correction in the Channel Estimation Software. The source is first fed to a frequency divider (factor 36) to obtain the 67-MHz clock source required by the ADCs. Next the signal is fed to a 1-to-8 power divider providing synchronization between each channel. In order to convert the sources to the 3.3Vpp transistor-transistor logic (TTL) waveforms required by the ADCs, a 20-dB amplifier and bias tees are required.

Digital Input-Output Clock

Communication between the PC's DAQ and sampling boards is carried out using the DAQ-defined Burst Protocol. This is a clocked protocol which can be driven either by an internally generated oscillator on the DAQ card or by an external source. In the

55

original architecture this communication was clocked using the internally generated source.

In the debugging stages of system development, however, it was found that there was a small probability (significant with respect to data accuracy) that the CEXE state of the sampling FSM for two different receive channels would begin at times offset by one sample clock cycle. In other words the snapshot of samples recorded by two different channels would be offset by one sample. The physical length of the DIO bus between PC and each receive channel varies over several inches. With this length variation the INST pins become active at each of the receiver channels at slightly different times. For instance for a five-cm disparity the difference in activation times is $\frac{0.05m}{3\cdot10^8\frac{m}{s}} = 1.67\cdot10^{-10}s$. With this timing variation there was a chance that a sampling clock pulse would arrive at the boards during a point in time where one board had active INST pins and the other did not. In this scenario then the first board would start sampling one clock cycle before the second. With a sampling clock cycle of 67Mhz this probability was $1.67 \cdot 10^{-10}s * 67 \cdot 10^6 \approx 1\%$ which is nontrivial.

The solution then was to drive the DIO with the same source as the sampling clock. This way the two would be synchronized, eliminating this type of error. To do this it was necessary to obtain a signal converter that took the low voltage sine wave input of the LO and converted to the TTL signal required by the DIO bus. Additionally the 67Mhz input had to be converted to a frequency lower than 20Mhz to meet the specs of the DAQ and FPGA, specifically 17 Mhz in this case.

4.1.6 Power Supply

The receiver is designed to be powered by either an AC or DC power source. This is achieved by supplying power to the system with an Uninterrupted Power Supply (UPS). The UPS has two modes of operation. When plugged into a standard wall outlet it supplies AC power and charges its backup battery source. When unplugged the UPS converts the DC power supplied from the backup battery to AC for distribution. Table 4.2 displays the power requirements of the various receiver subsystems and Figure 4-10 the subsystem diagram.
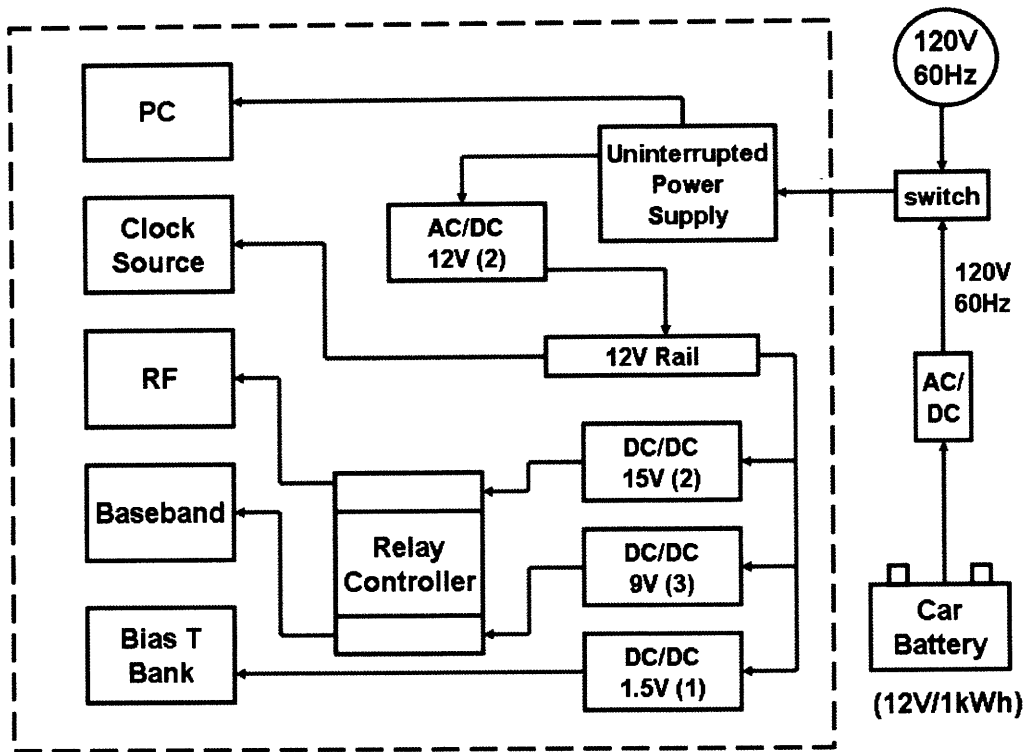
Figure 4-10: Power Distribution System

Table 4.2: Power Requirements

Source	Voltage	Average Amp Draw	Total Power
RF Front-Ends	15V	0.06A	0.9W x 8 = 7.2 W
Baseband PCBs	9V	0.52A	4.7W x 8 = 37.6 W
Clock Source	15V	0.15A	2.25W

The power requirements of the receiver excluding the CPU is 50W. The PC power supply is rated for consumption of at most 150W, but consumes less than this in practice.

DC Power Distribution

The RF Front-Ends and PCBs require 15V and 9V respectfully. To meet these voltage requirements the AC supplied by the UPS is first converted to 12V DC by a pair of AC/DC converters. The DC output is then supplied to a power rail for further distribution. In order to obtain the required voltage levels, a bank of 12V/15V and

12V/9V power supplies are fed to the distribution rail for supplying the individual subsystems.

Relay Controller

An additional layer separates the power supply bank from the various devices in the form of a 16-device relay controller. The relay board is controlled from the PC over a standard serial cable. This allows the PC to individually turn on and off each of the eight RF Front Ends and sampling boards. When running in DC supply mode power can then be conserved during periods of time that the receiver is not sampling the environment. During a typical measurement campaign this results in a very large power savings as much of the time is spent positioning the equipment. The power control is integrated into the scripts that control experiment execution.

4.1.7 Cabling

The hundreds of 50-ohm coax cables used for signal and power distribution in the receiver were each individually assembled for this project. The cable lengths were standardized for each sub-channel of the system in order to keep any propagation delays approximately equal for each.

4.1.8 Channel Filter

In the original architecture the first filter element on each channel was the anti-aliasing low-pass filter preceding the ADCs. This leaves the possibility that the amplifiers in the RF Front-End could be saturated by out-of-band interference that would attenuate any signal in the pass-band. To track this a 30-Mhz band-pass filter specifically designed for 802.11b channel 3 is placed at the antenna lead of one of the receiver channels. This event can then be tracked in the post-processing software. Such a circumstance has been observed to be negligible in practice.

4.2 Channel Sounder

The channel sounder transmits a known waveform in the propagation environment local to the receiver for purposes of measuring the wireless channel between the two devices. Specifically the channel sounder, used by the experiments presented in this thesis, is a modified ROOFNET node. ROOFNET is an experimental 802.11b/g mesh network developed at MIT CSAIL [28]. The channel sounder is configured to continuously transmit an 802.11b packet with arbitrary payload and duration. Figure 4-11 displays a block diagram of the transmission system.
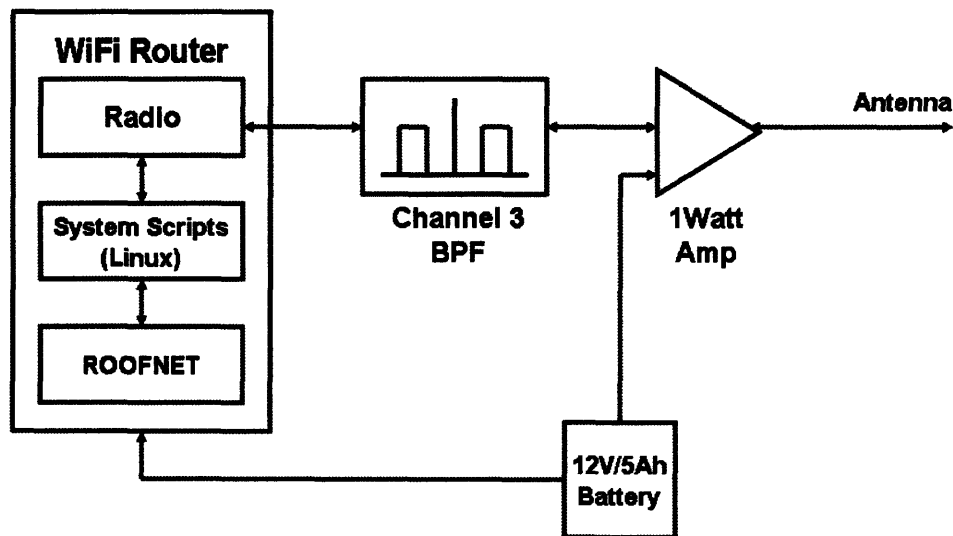
Figure 4-11: The Channel Sounder

4.2.1   802.11b

IEEE 802.11b (WiFi) is a member of the 802.11 suite of standards for Wireless Local Area Networks (WLAN). The 802.11b standard is defined by a two-layer protocol stack, consisting of the Medium Access Control (MAC) and Physical (PHY) Layers, both of which had to be properly managed for integration into the CDCS architecture.

MAC Layer

The MAC Layer is responsible for controlling access to the wireless medium. In particular a protocol known as Carrier Sense Multiple Access with Collision Avoidance (CSMA/CA) is used for medium sharing. Additionally the MAC is in charge of ensuring data is received reliably. This is handled through the addition of header information to each data packet, including address, control, and cyclic redundancy check bits. Additionally a system of Acknowledgement and Request packets are required for ensuring data exchange. A final function of the MAC layer is to add a level of security to the communication link. In 802.11b this comes in the form of an optional encryption standard, Wired Equivalent Privacy (WEP). The payload along with headers and redundancy check bits are packaged into what is referred to as MAC sublayer Protocol Data Units (MPDU) and sent to the physical layer for transmission. Figure 4-12 displays the layout of 802.11b packets.
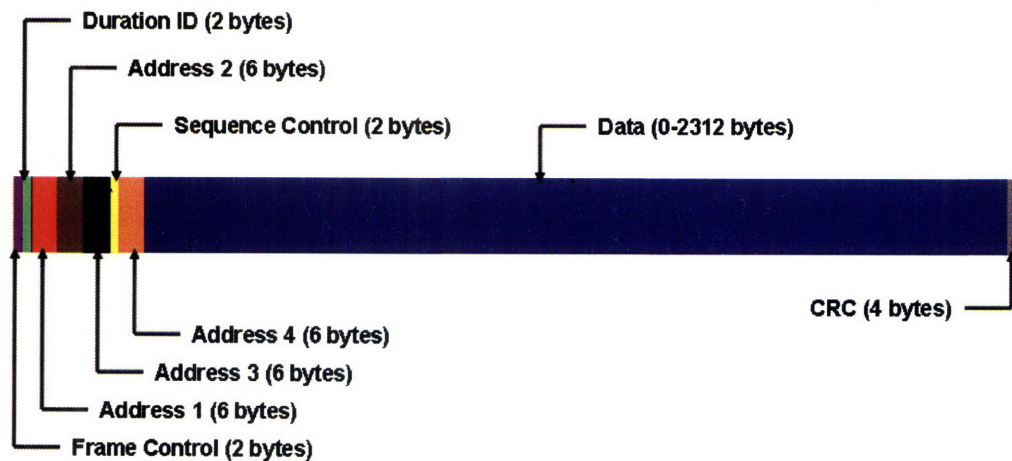
Figure 4-12: 802.11b Packet Structure

Physical Layer (PHY)

The physical layer of 802.11b supports data rates of 1Mbps, 2Mbps, 5.5Mbps, and 11Mbps along with three different PHYs: infrared, Direct Sequence Spread Spectrum (DSSS), and frequency hopping. Here we will discuss the 11-Mbps DSSS Physical

layer of 802.11b, as it is the version used for constructing the channel probing wave-form of the CDCS. The PHY can be broken up into two sub-layers, the Physical Layer Convergence Procedure (PLCP) and the Physical Medium Dependent (PMD) sub-layer. In the PLCP additional header information is added to the MPDU including a synchronization pre-amble and bitmap field for the various signal level options. After the PLCP Preamble and headers are added, the entire sequence of bits referred to as the PLCP Protocol Data Unit (PPDU) is passed to the PMD sub-layer.

The first step of the PMD is to whiten the bit sequence that makes up the PPDU. This is achieved by passing the PPDU through a scrambling filter defined by

$$W(z) = 1 + z^{-4} + z^{-7}$$

That is, the ith bit of the new bit sequence is equal to the bit-wise OR of bits i, i-4, and i-7 of the original bit sequence.

The next step of the PMD is to encode the bit sequence into a stream of constant magnitude complex numbers that will be used to phase modulate the signal carrier. This encoding is carried out by dividing the scrambled PPDU into segments of 8 contiguous bits and sequentially encoding the groups according to,

$$C_0 = e^{j(\phi_1 + \phi_2 + \phi_3 + \phi_4)}$$

$$C_1 = e^{j(\phi_1 + \phi_3 + \phi_4)}$$

$$C_2 = e^{j(\phi_1 + \phi_2 + \phi_4)}$$

$$C_3 = -e^{j(\phi_1 + \phi_4)}$$

$$C_4 = e^{j(\phi_1 + \phi_2 + \phi_3)}$$

$$C_5 = e^{j(\phi_1 + \phi_3)}$$

$$C_6 = -e^{j(\phi_1 + \phi_2)}$$

$$C_7 = e^{j(\phi_1)}$$

Here the phase angles $\phi_1, \phi_2, \phi_3, and\phi_4$ are determined by dividing the 8 bits into 4 groups of 2 (one for each angle) and calculating them according to the mapping in Table 4.3.

Table 4.3: 802.11b Phase Mapping

bits	Phase Angle
00	0
01	$\frac{\pi}{2}$
10	π
11	$\frac{3\pi}{2}$

In addition ϕ_1 is adjusted according to the value of ϕ_1 calculated from the previous group of 8 bits,

$$\phi_1^i = \phi_1^{i-1} + \delta^i$$

where ϕ_1^i is the value of ϕ_1 calculated for the ith byte and δ_i is the phase (from 4.3) associated with the first two bits of the ith byte. Lastly all odd numbered groups of eight bits are given an additional 180° phase shift.

The PMD is additionally responsible for phase modulating the appropriate carrier according this complex sequence. Before transmission the waveform is passed through a filter that meets the 802.11b spectral mask.
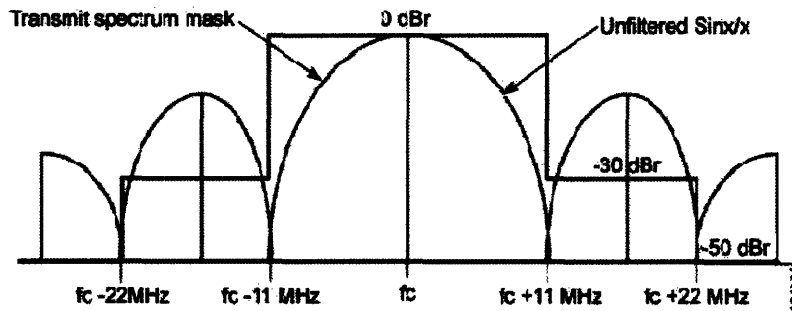
Figure 4-13: 802.11b Spectral Mask

802.11b calls for the spectrum to be divided into 11 overlapping channels (North America standard) each having a bandwidth of 22Mhz. Given the spectral mask

above there will be interference even across orthogonal channels. The channel used in the experiments of this thesis is channel 3 centered at 2.422Ghz.
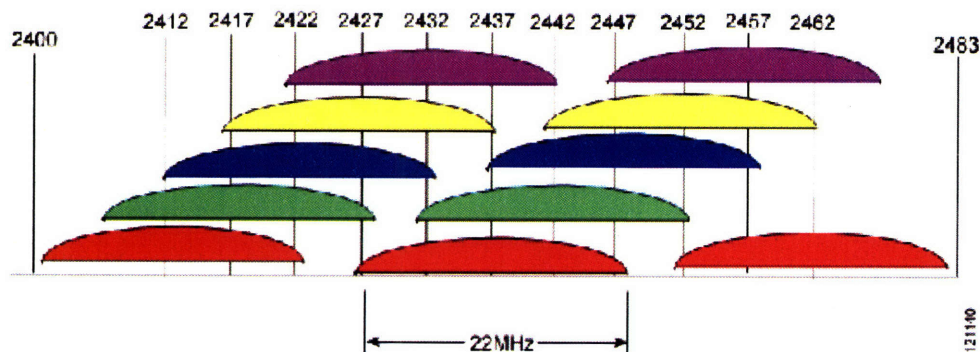
Figure 4-14: 802.11b Channel Allocation

4.2.2 CPU and Waveform Generation

The channel sounder itself is a Netgear WGT634U Wireless Router. The router contains a 200MHz Processor, 32MB RAM, and an Atheros AR5212 802.11b/g WiFi radio. The router runs Linux 2.4.20. Adding the ROOFNET software to the router allows the user to remotely login to the router over the mesh network that it deploys. A script on-board the router makes use of the ROOFNET software to continuously send 802.11b broadcast packets. Broadcast packets are ideal for this application as they do not require any acknowledgment/request packets by the 802.11b protocol. This script specifies the number of broadcast packets to be sent to the radio queue and the bit sequence that makes up the payload of the packet.

4.2.3 RF Front-End

The Netgear router that makes up the channel sounder is shipped with a 2.2dBi "rubber duck" antenna element that is directly soldered the the Atheros WiFi radio. In order to increase the maximum link radius for the wireless experiments to follow, a new more powerful RF Front-End was added to the router. First the rubber duck

63

antenna was removed along with the original Atheros WiFi radio. A new Atheros radio was installed with U.fl connectors. A U.fl-to-SMA pigtail then was added to give an external SMA lead for the RF Front-End. The RF Front-End itself consists of a band-pass filter (802.11b Channel 3) and a 1-W amplifier with lead for a configurable antenna. Transmit power in this band is limited to 30dbm (1W) for an isotropic antenna. In addition the law allows for use of up to a 6dB gain in the antenna element. All of our experiments were set up to fall within these limits. Table 4.4 outlines the specifications for the components of the RF front-end.

Table 4.4: Channel Sounder:RF Front-End Part Descriptions

Part	Specs
Band Pass filter	center: 2.422Ghz
	attenuation: > 60dB +- 25Mhz
Amplifier	frequency: 2.4Ghz
	output power: 1W (30dBm)
	input power: 0.1mW (-10dBm)

4.2.4 Power Supply

The 1W amplifier and the router each require a 12V DC supply. For this purpose a 12V rechargeable battery supplying 5ah is used. It has been found to be sufficient to supply the router and amplifier for greater than 5 hours.

4.3 Antennas

The antenna leads coming from the receiver are standard female coax connectors allowing for each receive channel to be independently linked to an arbitrary antenna element. The same holds for the channel sounder. We have chosen several antenna types for use in the various experiments of this thesis. Table 4.5 outlines the specifications of the various antenna elements utilized in our experiments.

Table 4.5: Antenna Specifications

Part	Gain	Directional	Polarization	# Available
Hyperlink Dipole	8dBi	no	single	9
Rubber Duck	2.2dBi	no	single	8
Hyperlink Dish	20.5 dBi	yes	single	1
RadioWaves Dish	21.1 dBi	yes	dual	1

4.4 GPS Tracking System

For many of our experiments it is of interest to keep track of link lengths for studying any relationships between link length and various other propagation parameters. To do this we have put together a GPS tracking system that records the GPS coordinates of the transmitter and receiver location for each snapshot of our data sets. The link length for each snapshot can then be calculated later in software utilizing the GPS coordinate data and eventually used in our analysis.

The GPS tracking system itself consists of a GPS receiver, laptop, and GPS driver/utility software. The GPS receiver is powered from the USB port of the laptop. Data received from the laptop is continually passed to the laptop over a USB cable. Third party GPS software then converts the raw GPS data into high resolution latitude/longitude coordinates. The software is configured to only store coordinate data when requested by the user. This way the user can specifically request storage of a GPS coordinate for each individual snapshot location.

4.5 System Control

Transmitter and receiver operation is controlled remotely by a Dell Latitude D620 Laptop Computer. This helps minimize the impact of the individual collecting the data on the channel environment.
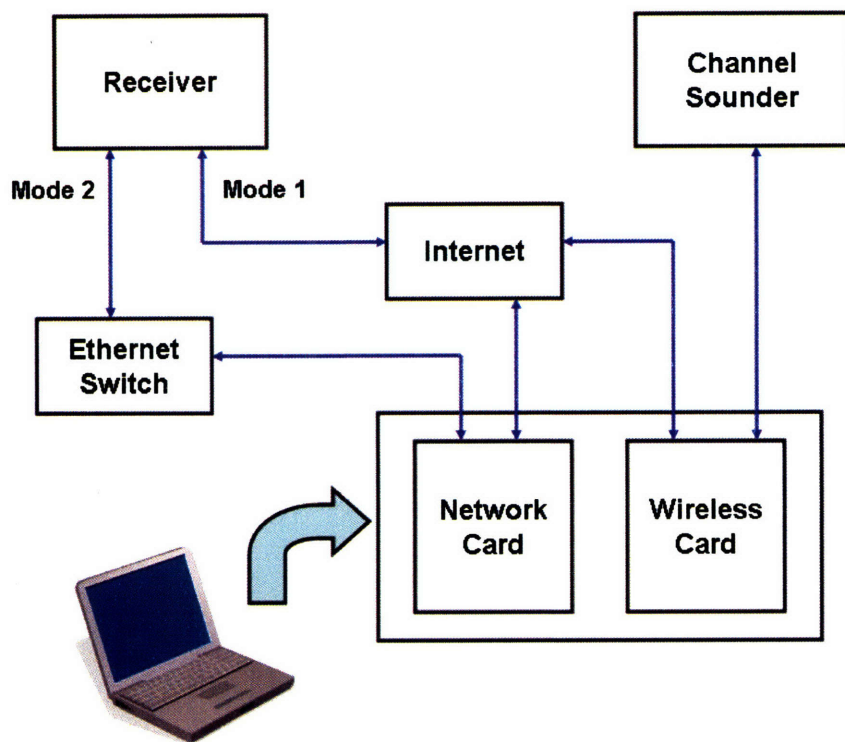
Figure 4-15: System Communication and Control

4.5.1 Receiver Control

The PC on-board the receiver contains a Linksys 100Mbps ethernet card. The communication link between receiver and controlling device is configured for two modes of operation. In the first mode of operation the communication takes place over the internet. This mode is used for downloading data from the receiver to the final database. Additionally this mode is used for on-site (MIT) experiments where it is useful for the controlling device (laptop) to be greater than 10 meters from the receiver. In this mode the laptop is either tethered or not dependent on the local availability of WiFi. The second mode of operation deploys the communication link over a stand-alone LAN between laptop and receiver. This mode of operation allows for mobile experiments and those sites where no internet is available. The receiver PC is assigned a dual IP address, a static MIT network IP for mode I, and a LAN IP for mode II.

Unlike the channel sounder which is in automated operation over the duration of

the field experiment, the receiver requires command input from the user for instruction on when and how to sample the environment. A system of bash shell and perl scripts has been implemented on both laptop and receiver PC to define and control this communication. For a given control sequence the interface to the user has been reduced to executing a single shell command. This shell command takes as input argument a data set name and experiment number for referencing its appropriate execution parameters in its template file. These parameters are then sent to the receiver PC to commence the sampling sequence that they define.

Data Set Templates

Each sampling sequence issued by the user is indexed by data set name and experiment number. The data set name is by date of collection with each individual sampling sequence given a unique experiment number. The execution for the 15th sampling sequence taken on January 29th from the laptop shell window is,

$$\% \quad go \quad 1 - 29 \quad 15$$

where go is the alias given to the shell script wrapper. The data set name and experiment number is then used to reference the line of the appropriate data set template file where the experiment's sampling parameters are stored. The format of this template file is as follows

$$N \quad \# \quad r0 \quad r1 \quad r2 \quad r3 \quad r4 \quad r5 \quad r6 \quad r7 \quad \# \quad T \quad \# \quad i$$

$$N \quad \# \quad r0 \quad r1 \quad r2 \quad r3 \quad r4 \quad r5 \quad r6 \quad r7 \quad \# \quad T \quad \# \quad i+1$$

$$N \quad \# \quad r0 \quad r1 \quad r2 \quad r3 \quad r4 \quad r5 \quad r6 \quad r7 \quad \# \quad T \quad \# \quad i+2$$

$$N \quad \# \quad r0 \quad r1 \quad r2 \quad r3 \quad r4 \quad r5 \quad r6 \quad r7 \quad \# \quad T \quad \# \quad i+3$$

$$\cdot \qquad \cdot \qquad \cdot \qquad \cdot \qquad \cdot \qquad \cdot$$

$$\cdot \qquad \cdot \qquad \cdot \qquad \cdot \qquad \cdot \qquad \cdot$$

where N is the number of time snapshots (complete 1ms bursts) per receiver channel, $r_j \epsilon \{0, 1\}$ is the bitmap for signifying which receiver chains to sample, T is the number of milliseconds to pause between each time snapshot, and i denotes the experiment number. A MATLAB script has been created to automatically generate these template files with the appropriate parameters for each collection session.

4.5.2 Transmitter Control

The ROOFNET software [28] running on the channel sounder creates a wireless peer-to-peer network allowing direct communication to take place between transmitter and laptop over the wireless medium. With this in place the laptop user can remotely login into the transmitter over this network and initiate the scripts for placing the transmitter in experiment mode. This initiation is reduced to issuing one shell command whose function is to adjust the transmitter's radio to the proper settings (11Mbps data rate, 2.422Ghz center frequency, Network mode), disable unnecessary system processes freeing most CPU cycles, and executing the channel probing script. This includes disabling the peer-to-peer network to remove channel conflicts, which results in loss of communication with the transmitter until the next power cycle (physical detachment from power supply). Since each session of data collection is taken over one power cycle, this expedites the time required in the field.

4.6 Real-Time Verification

An additional feature was added to the collection system to allow for Real-Time Verification of the channel data during field measurements. This feature is helpful in diagnosing battery exhaustion and other routine failures that might occur while in the field and thus helping to avoid collecting bad data. The implementation comes in the form of passing an additional parameter to the sampling execution script on the laptop which tells the receiver whether or not to pass back a set of snapshots

to the laptop for inspection. If this extra parameter is set to active, a single time snapshot from each of the receiver channels is sent back to the laptop, at which point MATLAB scripts are in place to display the resulting data in both the time and frequency domains for visual inspection by the user. Additionally the power received is plotted for each receive channel so that the user can adjust the attenuation level on the channel sounder for optimal placement within the dynamic range of the receiver.

4.7   Database Management

In addition to the sampling sequence parameters, the data set name and experiment number are also sent to the receiver PC. Again each sampling sequence will contain N time snapshots from at most 8 receiver channels, with each time snapshot containing 65k 2-byte samples. This data is organized on the hard disk of the receiver PC by assigning each 128kB snapshot file a filename according to:

$$D - E - S - R$$

where D is the data set name (collection date), E the experiment number, S the snapshot number, and R the receiver number. The snapshot files are stored in this format until the end of the field experiment, at which point the entire collection of data is downloaded to the database housed in the laboratory where the post processing will take place. The downloading process consists of first placing all snapshot files associated with each experiment number into a single archive file from which it is then sent to a compression engine. A filesystem is then created on the network store according to data set name and experiment number, and the compressed archives are then downloaded to it. The location and file

$$network/1 - 29/1 - 29 - 5/1 - 29 - 5.tar.gz$$

then refers to the 5th such archive collected on January 29th. This organizing mechanism then interfaces with the post-processing software that follows.

4.8 Receiver System – Model and Performance

Here we present the receiver system model that relates system input to system output along with their relevant time and frequency parameters. With this model we then present a series of experiments that were carried out to measure system performance and summarize the results.

4.8.1 System Model

Given the system description above, the data collected by the receiver system comes in the form of a time series of snapshots, y, for each receiver channel being recorded. Each snapshot (per channel), is comprised of 65K samples (FIFO capacity) sampled at a rate of 67Mhz. In the frequency domain this corresponds to the 33Mhz band centered at ≈ 2.422Ghz. The receiver system model is displayed in Figure 4-16. Here s(t) corresponds to the system input (antenna lead), n(t) represents all signal noise due to the system, and y the output (snapshot) of the system.
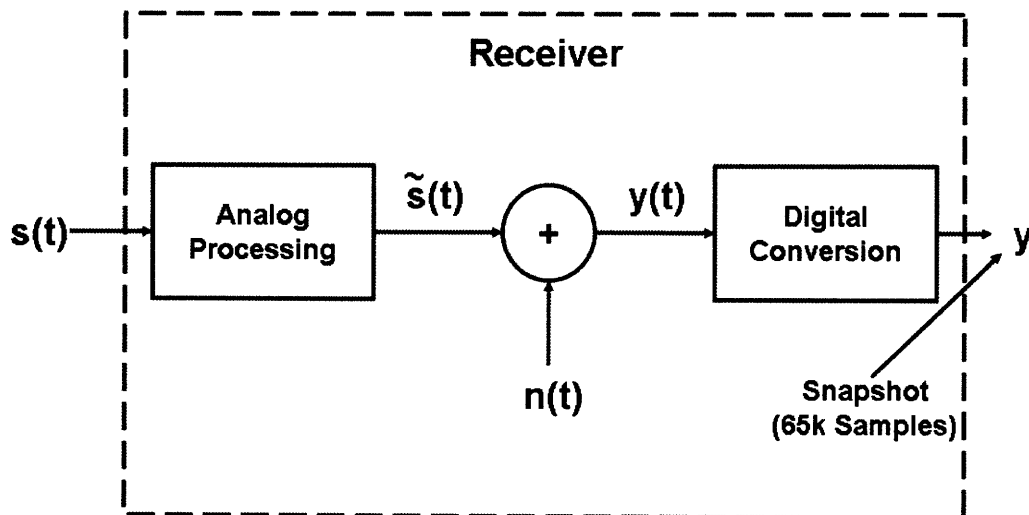
Figure 4-16: Receiver System Model

4.8.2 Dynamic Range

The first metric of interest with respect to system performance is the dynamic range of the system. By dynamic range we refer to the range of powers associated with the input signal, s(t), for which the system response is linear. This range is bounded above by the system saturation point, S. There is theoretically no lower bound on this range, however, we will define a lower bound as the system noise floor.

An experiment was devised for measuring this range for each receiver channel. The experiment proceeds by,

1. Connect the output of an RF signal generator to the input lead (where the antenna is normally connected to the RF front-end) of each receive channel.

2. Use the signal generator to produce a narrow-band signal in the center of the receivers pass-band (2.422Ghz) at a set of power levels that span the dynamic range of the receiver.

3. For each power level record and store several snapshots.

4. Calculate the variance of the sampled waveforms at each input power. Having done this we obtain a relationship between system input power and system output power. With this we obtain several points along the system response curve, see Figure 4-17.

   Here we note that this curve is linear with non-linearity behavior at each end point. The objective is to find the dynamic range of this linear region for each receiver chain. Here we define the dynamic range as the range between the 1dB compression point and the noise floor, which we define later in this section.

5. To accomplish this we first fit a line to the linear portion of the curve to approximate what the system response would be if it was entirely linear. Recall the linear input-output system model,

$$y(t) = s(t) + n(t)$$

71
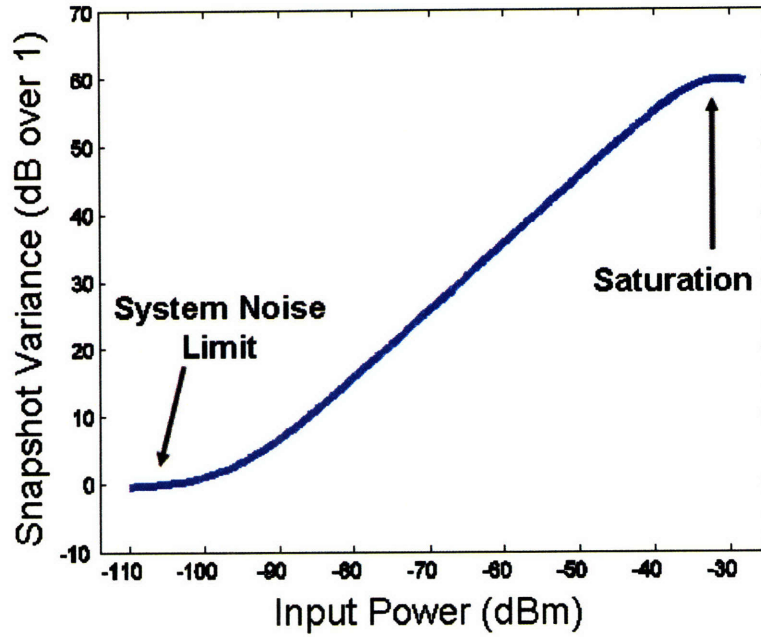
Figure 4-17: An example response curve calculated during dynamic range calibration

With system input, s(t), and system noise, n(t), uncorrelated the input-output power relation is,

$$P_y = P_s + P_n$$

On a dB scale this relation can be approximated as,

$$P_y^{dB} \approx P_s^{dB}$$

whenever $P_s >> P_n$. This relation holds for values of P_s over the linear portion of the response curve. Finding the linear approximation then can be done by performing Ordinary Least Squares (OLS) regression using only the data points on the linear portion of the curve,

$$P_y^{dB} = \alpha + \beta \cdot P_s^{dB} + \epsilon$$

$$[\widehat{\alpha}, \widehat{\beta}]^T = (S^T S)^{-1} S^T Y$$

where,

$$S = \begin{pmatrix} P_s^{dB}[\text{linear}_{min}] & 1 \\ P_s^{dB}[\text{linear}_{min} + 1] & 1 \\ \vdots & \vdots \\ P_s^{dB}[\text{linear}_{max}] & 1 \end{pmatrix}$$

$$Y = \begin{pmatrix} P_y^{dB}[\text{linear}_{min}] \\ P_y^{dB}[\text{linear}_{min} + 1] \\ \vdots \\ P_y^{dB}[\text{linear}_{max}] \end{pmatrix}$$

where linear_{min} and linear_{max} are the indices of the first and last points of the linear region of the data respectfully. $\widehat{\beta}$ should be close to unity while $\widehat{\alpha}$ is the unit conversion factor between input and output units. The calculated values for each receive channel are in the Table 4.6.

Table 4.6: OLS Regression Estimates

Rx No.	$\widehat{\alpha}$	$\widehat{\beta}$
0	143.49	.9907
1	143.68	.9908
2	142.71	.9903
3	143.01	.9902
4	145.25	.9916
5	143.57	.9905
6	142.27	.9901
7	143.34	.9917

Here we note that the regression estimates of the slope are $\approx$ .99 for each channel

73

due to the finite data set over which the estimation is calculated.

6. The 1dB compression point is defined as the point on the response curve at which the output power is attenuated by 1dB with respect to the linear approximation to the curve. Using the regression calculated above the 1dB compression point is calculated for each receive chain. Table 4.7 displays the 1dB compression points calculated for each channel.

Table 4.7: 1dB Compression Points, Noise Floors, and Dynamic Ranges (10Mhz)

Rx No.	Compression Point	Noise Floor (dBm/Hz)	Dynamic Range
0	-37dBm	-167.93	60.93dB
1	-37dBm	-168.35	61.35dB
2	-36dBm	-168.45	62.45dB
3	-36dBm	-167.93	61.93dB
4	-38dBm	-168.86	60.85dB
5	-36dBm	-168.44	62.44dB
6	-36dBm	-168.21	62.21dB
7	-36dBm	-168.36	62.35dB

7. Thermal noise is the intrinsic system noise cause by the random movement of electrons due to thermal agitation. To measure the thermal noise floor one can again make use of the system response curve. The input power that increases the output power by 3dB from its zero input response is a good estimate of the power due to thermal noise. The thermal noise floor is then estimated for each channel by locating this 3dB point on each channel's response curve. Table 4.7 lists the calculated noise floor for each receiver.

8. The dynamic range for each channel then is calculated as the range between the estimated 1dB compression points and thermal noise floors. Note that the thermal noise power scales with bandwidth. To give a representative dynamic range then we make this calculation over 10Mhz which we will later define as the bandwidth of our channel estimation software. The dynamic ranges calculated for each channel are found in Table 4.7.
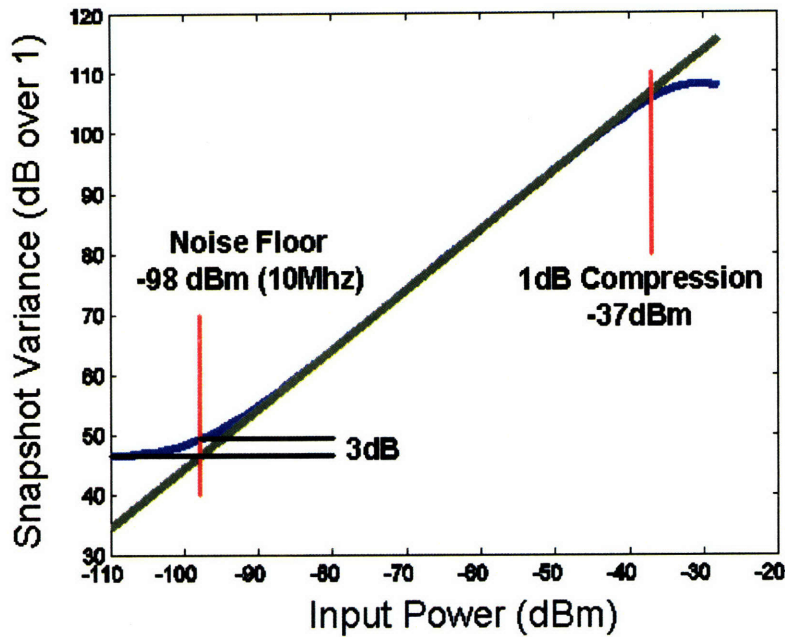
Figure 4-18: A representative channel's calibration curve (channel 0)

4.8.3   System Noise – Power Spectral Density

We would like to be able to model the system noise (thermal) as being white (equal power across frequency). However we must validate this assumption which we do through the following experiment:

1. Each channel is first terminated with a 50 ohm matched load (at the antenna terminal).

2. A number of time snapshots were recorded on each channel.

3. Calculate the PSD of each channel by averaging over the snapshots.

The resulting PSDs were found to be flat across frequency with the only variation across frequency being on the order of 1dB. However this was a smooth variation due to pass band ripple from the bandpass filters.
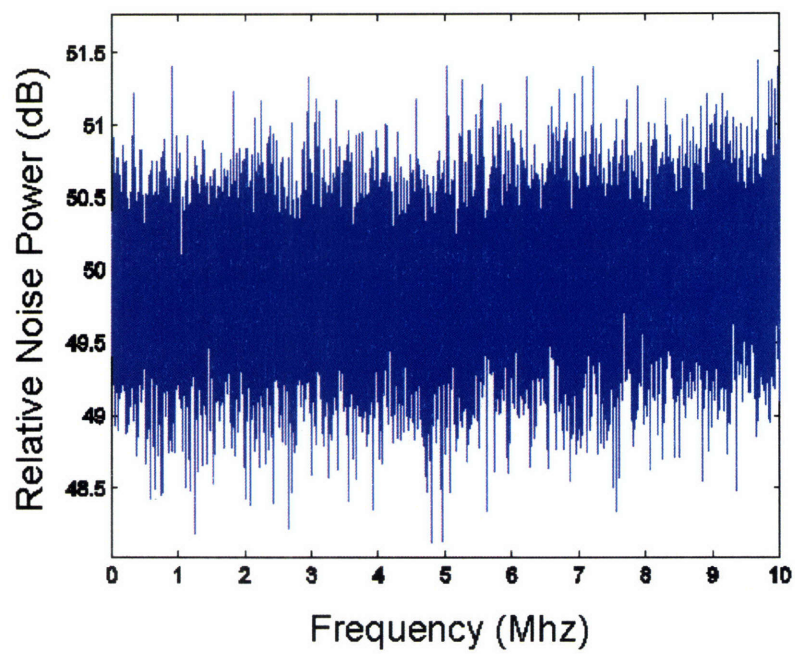
Figure 4-19: Power Spectral Density of a representative channel terminated by a matched load

Figure 4-19 displays the power spectral density for a representative channel when terminated with a matched load. The experiment validates the white noise assumption with respect to system noise.

4.8.4 Synchronization

Another important measure of receiver system performance is the level of synchronization between the eight channels. For the multiple antenna experiments to follow it is crucial that each channel remain synchronized with the others. With slight differences in cable lengths from channel to channel there will not be exact phase synchronization but this does not matter so long as the phase differences between channels are approximately constant over time. To directly measure the differential phase stability between channels a lab experiment was devised,

1. First a RF signal generator supplying a sinusoid in the middle of the pass band (2.422Ghz) was split with a 1-to-8 power divider and fed to each of the eight antenna leads.

2. This sinusoid was then sampled on each channel simultaneously over a long time interval composed of many snapshots.

3. Next the data was processed to find the phase of the sampled sinusoid for each channel as a function of time snapshot.

4. The phases over time were then compared between channels giving a differential phase function between each channel and a reference channel (rx0). Figures 4-20 and 4-21 display the resulting figures for two channels.

Here we see that the channel synchronization is quite stable with jitter over this test set on the order of hundredths of a radian.

4.8.5 Snapshot Rate

Additionally system performance is measured by how many snapshots can be recorded per second. Recall that a snapshot involves filling the 65KSample FIFO buffer at a
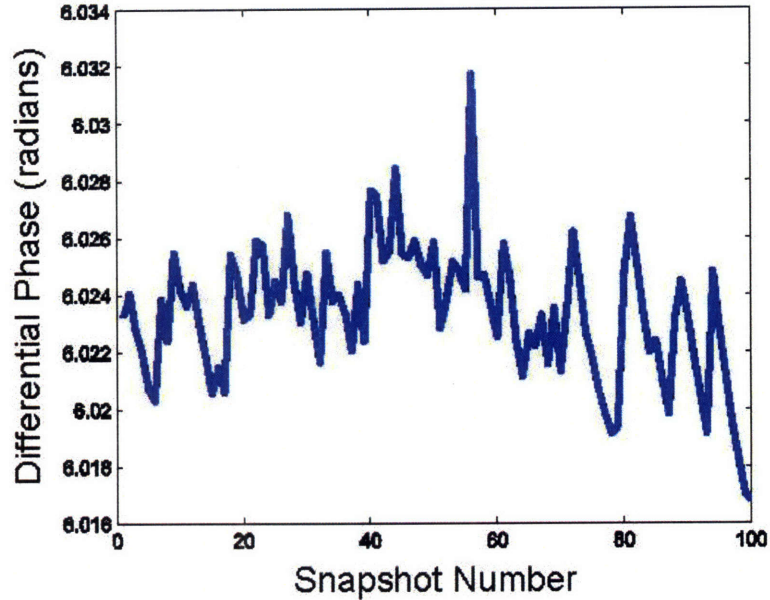
Figure 4-20: Differential Phase between rx0 and rx1 over 100 time snapshots

rate of 67MSps. This gives a continuous burst length of 1msec. Between snapshots the data in the FIFOs must be downloaded to the PC sequentially over a 16MSps bus. If the download time comprised the total time loss between snapshots then the time resolution would be,

$$\frac{65}{16 \cdot 1024} \approx .0037 \; \frac{\text{seconds}}{\text{receiver}} = .03 \; \frac{\text{seconds}}{8 \; \text{receivers}}$$

To measure the realized time resolution the following experiment was performed first using one channel and then using all eight channels,

1. Take 100 time snapshots on the channels being considered.

2. Record in software the time elapsed in seconds since the first time snapshot.

3. Find the time resolution as the total time elapsed divided by the total number snapshots. Below are the results.
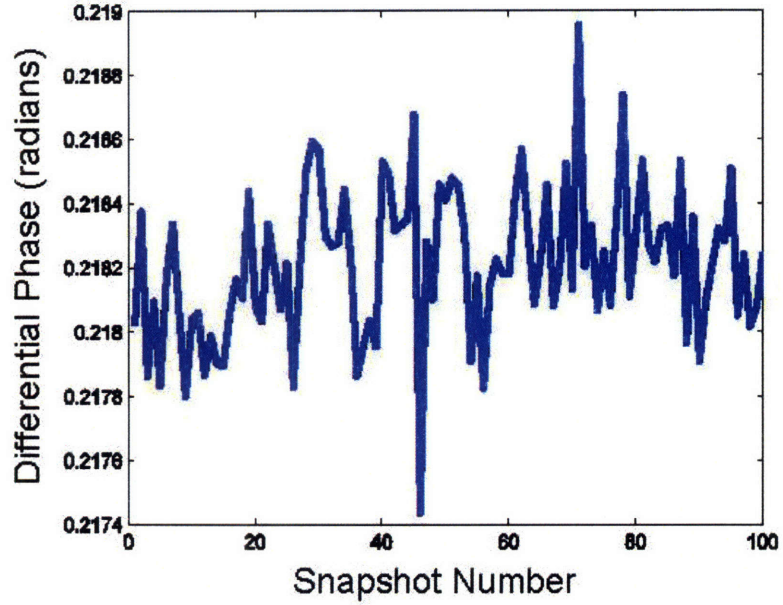
Figure 4-21: Differential Phase between rx0 and rx6 over 100 time snapshots

Given this procedure we found the snapshot rates to be 25 $\frac{\text{snapshots}}{\text{sec}}$ and 3 $\frac{\text{snapshots}}{\text{sec}}$ when utilizing 1 and 8 receive channels respectively. Here we see that the time resolution is ten times worse than what would be expected from the data download loss. This shows that the software execution time and writing the data from memory to disk dominates the snapshot rate.
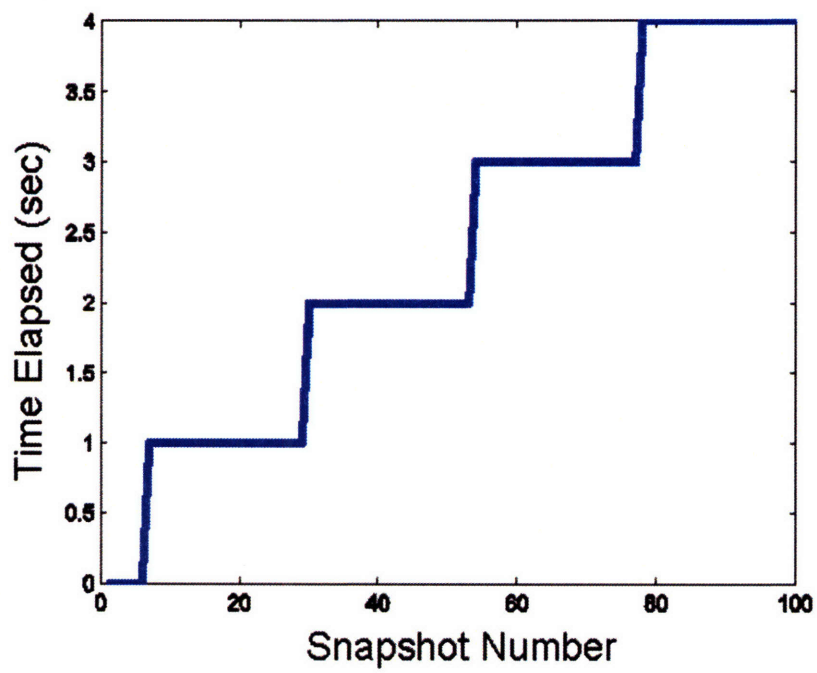
Figure 4-22: Time Resolution Experiment, 1 channel
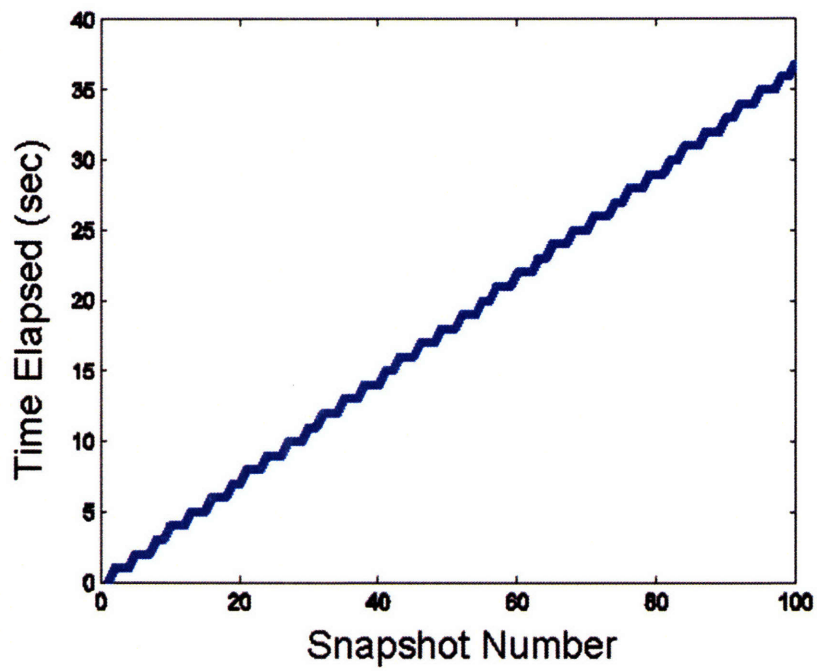
Figure 4-23: Time Resolution Experiment, 8 channels

Chapter 5

Channel Extraction and Estimation

The Channel Extractor is a collection of algorithms implemented in MATLAB that are used to estimate the complex channel information, representing the link between transmitter and receiver, from the raw channel data collected by the system (CDCS) described in the previous chapter. It was developed specifically for this purpose. The channel estimates provided by the channel extractor are used as the base measurement for the multiple antenna propagation analysis and experiments to follow. The software can be broken into the following functional blocks: Matched-Filter Construction, Front-End Processing, Detection, Time-Frequency Correction, and Channel Estimation.

5.1   Channel Estimation Model and Problem Definition

The wireless channel can be generally described as a time-varying linear system representing the superposition of time-varying propagation paths between transmitter and receiver,

$$y(t) = h(t, \tau) * x(t) + n(t)$$

Here y(t), x(t), and n(t) represent the output, input, and noise of the channel respectively. The channel impulse response, h(t,τ), varies slowly with τ. The instantaneous channel, h(t), can be expressed as a sum of P propagation paths,

$$h(t) = \sum_{i=1}^{P} \alpha_i \delta(t - d_i)$$

where α_i and d_i are the attenuation and delay of the ith path. Here we model the channel as having additive white gaussian noise,

$$n(t) \sim \mathcal{CN}(0, \sigma_n^2)$$

if no prior information is available with respect to this parameter.
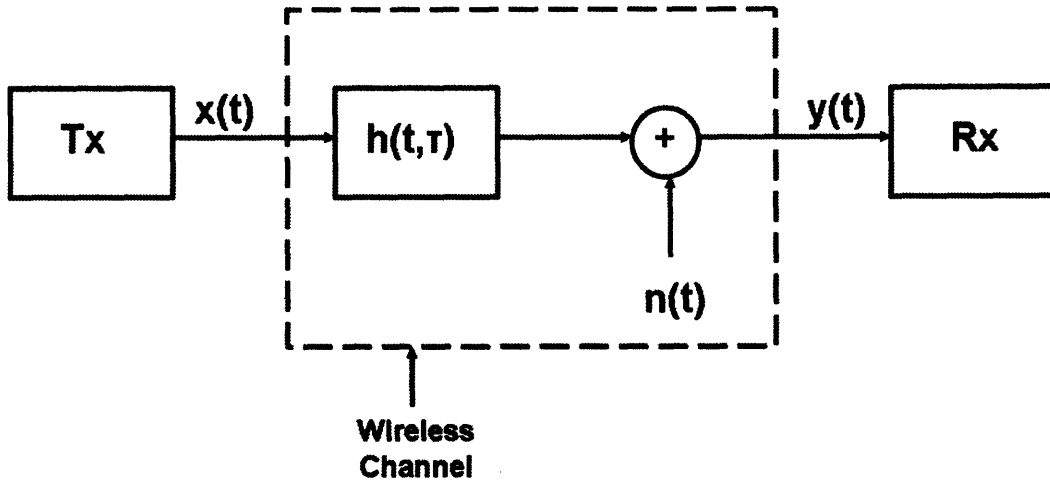
Figure 5-1: Wireless Channel between a single pair of antennas (SISO) as time-varying linear system

The problem of channel estimation then can be defined as estimating the unknown channel h(t,τ), given the white-noise-corrupted channel output y(t) and channel probing waveform x(t). However, in order to carry out channel estimation using the data collected by our system (CDCS) we must expand this model to reflect all relevant system behavior.

5.1.1 System Extraction Model

The data set collected by the system (CDCS) is composed of a time series of snapshots. Each snapshot (per antenna), y, is a vector of N=65K samples recorded at the system sampling rate of 67Mhz representing the noise corrupted signal received at the receiver over a 1ms continuous window of time. The snapshot y can be expressed as,

$$y = s + n$$

with y,s,n ϵ $\mathcal{C}^N$, and

$$n \sim \mathcal{CN}(0, \sigma_n^2 \cdot \mathbf{I}_N)$$

Here s represents all contributions to the snapshot, y, due to signal received from the transmitter and n represents both channel and system noise. In order to carry out channel estimation from a snapshot, y, we must relate the channel $h(t,\tau)$ to the sampled signal at the receiver, s.

First recall from Section 4.2 that the transmitter operates by continuously broadcasting packets whose payload is the channel probing waveform, x(t). These transmissions are not coherent with the receiver snapshot window. This results in random timing alignment for each snapshot y and the channel-filtered packet, $h(t,\tau)*x(t)$, that it contains. For now assume that the length of x(t) and $h(t,\tau)$ is $\frac{M}{B}$sec and $\frac{L}{B}$sec respectfully where B=67Mhz is the system sampling rate, and M/L are the sample lengths of x(t)/h(t). See Section 5.8.3 for the actual values of M and L used in our system. Additionally for this analysis we will assume that the signal arrival window (length $\frac{M+L}{B}$ sec) is less than the snapshot window (length $\frac{N}{B}$ sec) and the random alignment is such that the entire arrival window is contained in the snapshot. The significance of these two assumptions will be explored later in this chapter.

We will consider the channel, $h(t,\tau)$, to be constant over the duration of a snapshot (1msec) leaving the channel as h(t). That said, the contribution of the channel probing signal x(t) to the snapshot y before sampling is:
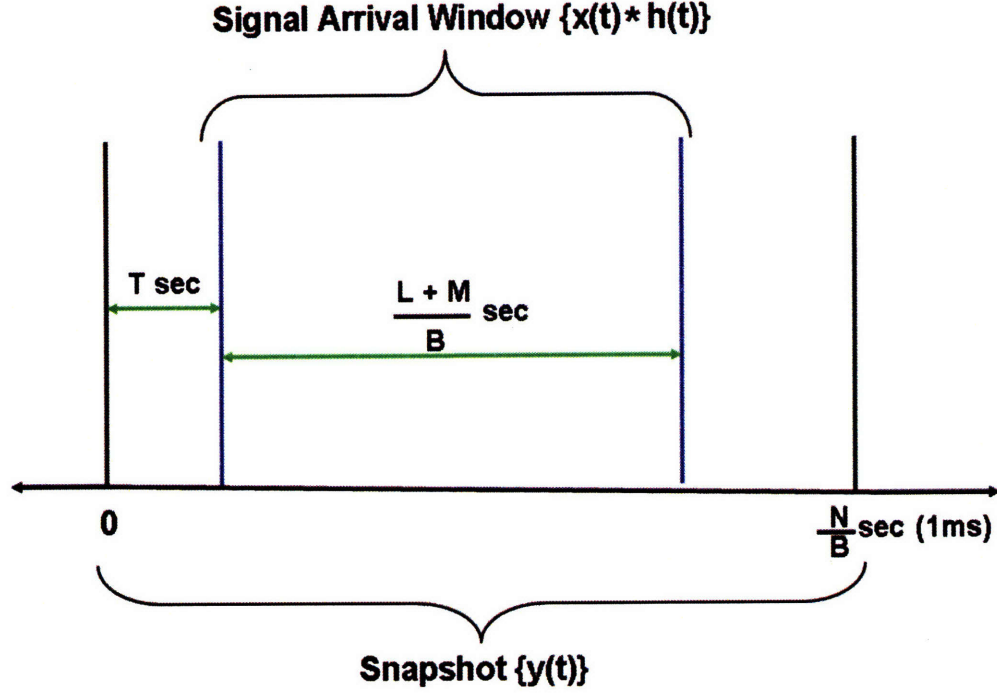
Figure 5-2: The Snapshot

$$s(t) = \begin{cases} h(t) * x(t - \tau) & \text{for } t\epsilon[\tau, \tau + \frac{M+L}{B}] \\ 0 & \text{otherwise} \end{cases} \qquad (5.1)$$

Here $[\tau, \tau + \frac{M+L}{B}]$ represents the sub-interval of the snapshot that contains signal contribution from the transmitter. Note any contribution from packet headers has been ignored here but will be discussed later. The parameter τ represents the random timing alignment between the window of signal arrival (legnth $= \frac{L+M}{B}$) and the snapshot (length $\frac{N}{B}$).

Recalling Section 5.1, the channel impulse response h(t) can be modeled as an impulse train corresponding to the individual signal paths between transmitter and receiver,

$$h(t) = \sum_{i=1}^{P} \alpha_i \cdot \delta(t - d_i) \qquad t\epsilon[0, \frac{L}{B}] \qquad (5.2)$$

where α_i, d_i represent the amplitude and delay of the ith of P paths. We can substitute

86

5.2 into 5.1 to obtain,

$$s(t) = \begin{cases} \sum_{i=1}^{P} \alpha_i \cdot x(t - \tau - d_i) & \text{for } t\epsilon[\tau, \tau + \frac{M+L}{B}] \\ 0 & \text{otherwise} \end{cases} \tag{5.3}$$

Applying the sampling theorem to x(t) we have,

$$x(t - \tau) = \sum_{m=0}^{M-1} x_m \cdot \text{sinc}(B \cdot (t - \tau) - m) \tag{5.4}$$

where,

$$x_m = x(\frac{m}{B})$$

Substituting 5.4 into 5.3 we obtain,

$$s(t) = \begin{cases} \sum_{i=1}^{P} \alpha_i \sum_{m=0}^{M-1} x_m \cdot \text{sinc}(B \cdot (t - \tau - d_i) - m) & \text{for } t\epsilon[\tau, \tau + \frac{M+L}{B}] \\ 0 & \text{otherwise} \end{cases}$$

After sampling s(t) at $\{t = \frac{n}{B}\}_{n=0}^{N-1}$ we have,

$$s_n = s(\frac{n}{B}) = \begin{cases} \sum_{m=0}^{M-1} x_m \sum_{i=1}^{P} \alpha_i \cdot \text{sinc}[n - m - B(\tau + \cdot d_i)] & \text{for } n\epsilon[\lceil \frac{\tau}{B} \rceil, \lceil \frac{\tau}{B} \rceil + L + M - 2] \\ 0 & \text{otherwise} \end{cases}$$

$$\tag{5.5}$$

In section 5.1 we defined the channel vector, h ϵ $\mathcal{C}^L$, as the discrete-time-domain representation of the channel impulse response, h(t). The lth tap is defined as:

$$\{h_l\}_{l=0}^{L-1} = \sum_{i=1}^{P} \alpha_i \cdot \text{sinc}[l - B \cdot d_i]$$

With this definition we can simplify equation 5.5 to,

$$s_n = \begin{cases} \sum_{m=0}^{M} x_m \cdot \tilde{h}_{n-m-\lceil \frac{\tau}{B} \rceil} & \text{for } n\epsilon[\lceil \frac{\tau}{B} \rceil, \lceil \frac{\tau}{B} \rceil + L + M - 2] \\ 0 & \text{otherwise} \end{cases} \tag{5.6}$$

where,

$$\{\tilde{h}_l\}_{l=0}^{L-1} = \sum_{i=1}^{P} \alpha_i \cdot \text{sinc}[l - B \cdot (d_i + \tau - \lceil \tfrac{\tau}{B} \rceil \cdot B]$$

Here note that h and $\tilde{h}$ differ only by the delay term $\tau - \lceil \tfrac{\tau}{B} \rceil \cdot B$. This is due to the random alignment between the signal arrival window and the samples of the snapshot. This delay is arbitrary in defining the discrete-time channel impulse response, h, but must be accounted for when comparing channel estimates taken across different snapshots, an issue discussed in the analysis to follow. Equation 5.6 can be then expressed as,

$$\{s_n\}_{n=\lceil \tfrac{\tau}{B} \rceil}^{\lceil \tfrac{\tau}{B} \rceil + L + M - 1} = x * h$$

Thus the snapshot, y, is equal to the sampled probing waveform, x, convolved with the discrete-time channel impulse response h with a random sample offset of $\lceil \tfrac{\tau}{B} \rceil$ (plus noise). The channel estimation problem can now be defined as that of estimating the discrete-time channel impulse response, h ϵ C^L, given the noisy snapshot, y ϵ C^N, and sampled channel probing waveform x ϵ C^M.

5.2 Matched Filter Construction

In the problem formulation above we have assumed that the sampled channel probing waveform, x, is known to the estimator. Recalling section 4.2, the waveform, x, is the payload of an 801.11b packet generated by a script on board the channel sounder. The bit sequence that comprises the payload is configurable to the user.

Two methods for obtaining the probing signal, x were explored. The first was to use the known bit sequence to simulate the construction of the waveform in software. The disadvantage of this method is that each WiFi implementation has subtle differences in the way that it constructs packets making it difficult to exactly replicate the waveform produced by the WiFi radio in our sounder. Given that the estimation performance is heavily dependent on the accuracy of this construction an alternative method was pursued.

The alternative method is to directly sample the the transmitted waveform at

the receiver over a wired channel. In this case the system impulse response from transmitter output to receiver output is approximately a single impulse. That said the waveform sampled at the receiver will be approximately equal to a scaled version of the probing waveform. This method then allows us a way to directly measure the probing waveform.
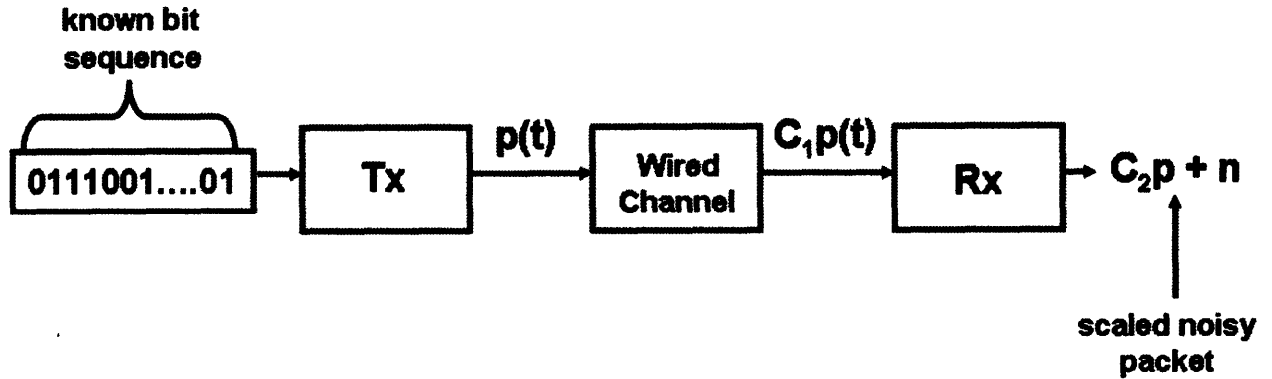
Figure 5-3: Measuring the Channel Probing Waveform

5.2.1 Packet Structure

From section 4.2.1, the 802.11b packet, p(t), has the following structure,

$$
p(t) = \begin{cases} p_{header}^{front} & \text{for } 0 \leq t \leq h_1 \\ x(t - h_1) & \text{for } h_1 < t < h_2 \\ p_{header}^{back} & \text{else} \end{cases}
$$

This states that there is a header at the front (p_{header}^{front}) and back (p_{header}^{back}) of the packet with the channel probing waveform, x(t), as its payload. With the two header components changing from packet to packet they will be unknown in general and can be considered as noise. It is then necessary that we exclude these two sections of the packet when constructing the matched filters. To do this it is necessary to estimate h_1 and h_2, the position of the payload within the packet.

5.2.2 The Number 128

Recall from Section 4.2.1 that the entire (including header bits) bit sequence in 802.11b is passed to a scrambler described by the equation,

$$W(z) = 1 + z^{-4} + z^{-7}$$

where the + operator represents the bit-wise OR operation. Here we see that the ith bit of scrambled sequence is determined by bits i, i-4, and i-7 of the original sequence. With this in mind, the scrambled bit payload is completely determined by the original bit payload and the 7-bits that precede it in the original complete bit sequence (including headers bits). With the original payload known to the user, the last 7 bits of the front header determine the waveform that will be transmitted. Experimentally it was found that these 7 header bits are equally likely to take on any of the $2^7 = 128$ possible 7-bit words. Since these 7 bits are not configurable to the user this means that the channel sounding waveform for any particular transmission are selected with equal probability from a set of 128 possible waveforms. This adds an extra level of complexity to the channel estimation algorithm as it is now necessary to decode which of 128 waveforms was sent.

5.2.3 Packet Size

As discussed in section 5.1.1, the packet size is constrained to be less than the length of the snapshot window. Further, in section 5.4 a snapshot will be defined as being acceptable for channel estimation only if it contains a complete signal arrival window. That said, there is a tradeoff between shortening the packet length whereby the probability of meeting this constraint increases and lengthening it which leads to a longer training sequence and hence improved estimation performance.

5.2.4 Construction Algorithm

Given this background the problem of matched filter construction involves obtaining all 128 channel probing waveforms from a series of T snapshots, $\{y_i\}_{i=1}^{T}$, taken of the wired channel described above. To implement this construction the following algorithm was built,

$$\{y_i\}_1^T \rightarrow \boxed{\begin{array}{c}\textbf{Payload}\\\textbf{Locater}\end{array}} \rightarrow \boxed{\begin{array}{c}\textbf{Equiv Class}\\\textbf{Sorter}\end{array}} \rightarrow \boxed{\begin{array}{c}\textbf{Reduction-}\\\textbf{Normalize}\end{array}} \rightarrow \{x_i\}_1^{128}$$

Figure 5-4: Matched Filter Construction Algorithm

Payload Location (good SNR)

The first step of the construction algorithm is to locate the payload, x, within each snapshot y_i window. Recalling the previous section, the channel sounder and receiver are non-coherent in that the transmitter continuously transmits one of 128 waveforms (plus random headers) while the receiver independently records snapshots. We must then find the position of the waveform in the snapshot window and then use this knowledge to remove all excess samples including headers. To accomplish this the snapshot is scanned starting from the first sample for a silent period defined as an interval of samples when no packet is being received. The beginning of a packet then is found as the end of this silent period. With a packet located in the snapshot we use our knowledge of the header sizes to strip out only those samples corresponding to the payload x. The payload x, from snapshot y_i is then passed on to the next stage of the construction algorithm.

Equivalence Class Sorting

After the channel probing waveforms have been stripped from the snapshots they must be sorted into equivalence classes, i.e. each snapshot's waveform is placed in exactly one class. Each equivalence class represents one of the possible 128 probing waveforms. The sorter operates by,

1. Start with one class whose only member is the waveform from the first snapshot.

2. Cross-correlate the waveform from the current snapshot with one member from each existing class to determine whether its class has been found yet.

3. If its class has been found then add it as a new member to its corresponding class and return to step 2 for the next snapshot.

4. If its class has not been found yet then create a new class whose only member is the waveform from the current snapshot. Return to step 2 for the next snapshot.

The algorithm should end in there being exactly 128 equivalence classes each with at least one member waveform. This was found to be the case.

Reduction and Normalization

The last stage of the construction algorithm reduces these classes into the set of matched filters, $\{x_i\}_{i=1}^{128}$, by selecting one member waveform from each class. Lastly the matched filters are normalized to be zero-mean and unit-variance.

5.2.5   Matched Filter Error

It must be noted that this method of obtaining the 128 matched filters is not exact. Having sampled these waveforms with the CDCS, system noise is added unavoidably to the library of matched filters. In order to minimize this source of error the transmission power was set such that the waveforms are transmitted at the upper end of the dynamic range of the receiving system. This gives an optimal Signal-to-Noise ratio for the resulting matched filters. In practice this source of error is small and is discussed further in the performance analysis section at the end of the chapter.

5.3   Front-End Processing

Some digital front-end signal processing is carried out on both the raw snapshots, y, and matched filters, x before they are passed on to the various extraction algorithm

blocks. The processing is used to remove out-of-band noise from the raw data, which increases the accuracy of the time domain processing that follows. Additionally we obtain the complex analytic representation of the signal through this processing to facilitate the frequency correction component of the algorithm.
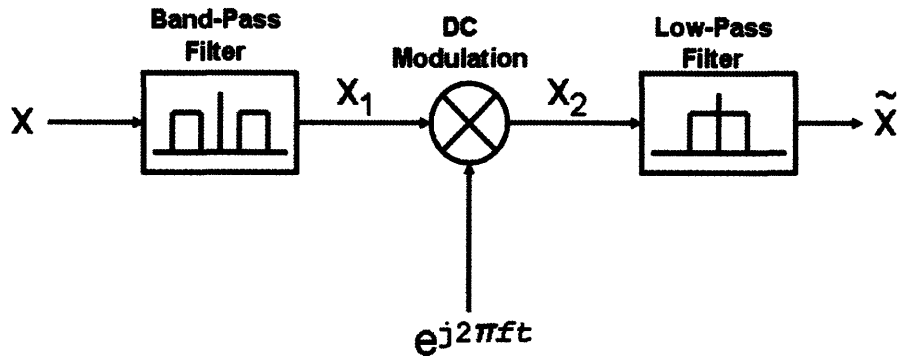
Figure 5-5: Front-End Processing Block

Band-Pass Filter

From Section 4.2.1, the 802.11b spectral mask is such that the power transmitted at ± 11Mhz from the center of the band is attenuated by at least 30dB. Additionally the LO frequency of our receiver is 2.406 Ghz, the channel sounding band (802.11b channel 3) is centered at 2.422Ghz, and the receiver sampling rate at 67Mhz. Given this information the baseband frequency region containing signal useful for channel estimation is [5Mhz, 27Mhz]. The first step of the Front-End Processor is to digitally band-pass filter the snapshot to this frequency band. This removes any out-of-band noise for the time-domain processing. Figure 5-6 displays the gain (in frequency domain) of the band-pass filter.

DC Modulation

Next we obtain the analytic representation of the data. To do this we first modulate the data with a complex exponential with frequency such that the right half of the signal spectrum is re-centered at zero frequency. See Figure 5-7 for the corresponding spectrum.
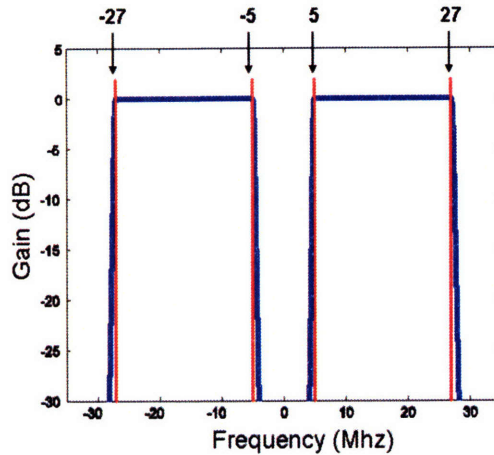
Figure 5-6: Gain of band-pass filter

Low-Pass Filter

The last step is to low-pass filter the data, leaving the analytic signal. See Figure 5-8 for the corresponding spectrum.

5.4 Detection Block

Every snapshot, y, obtained at the receiver must be classified as either being useful for channel estimation or not. To be considered useful for channel estimation the snapshot window must overlap with the arrival of a packet from the channel sounder. This is not guaranteed given the asynchronous relationship between receiver and channel sounder. To reduce computation time, decrease the implementation complexity, and provide consistent performance, the snapshot is considered good only if it contains an entire signal arrival window. This classification boundary increases the number of unsuitable snapshots but at an acceptable cost given the high probability (≈ 0.8) of containing an entire arrival window. The function of the Detection Block is to make this classification. In order to do this more information is needed regarding the channel filtered waveform contained in the snapshot, including its waveform number (128 possible) and frequency information. The classification of a sample snapshot as
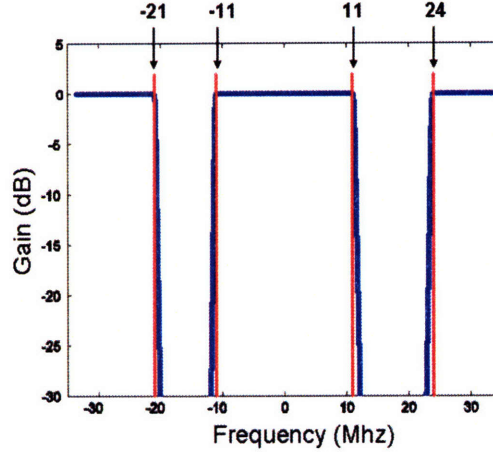
Figure 5-7: Spectrum of Modulated Data x_2

useful for estimation or not will be denoted by the outcomes $\mathcal{H}_0$ and $\mathcal{H}_1$ respectfully.

5.4.1   Oscillator Drift

Consider a waveform, x(t), transmitted at the carrier frequency,

$$x_c(t) = x(t) \cdot \cos\left(2\pi f^T \cdot t + \theta_T\right)$$

where f^T and θ_T are the oscillator frequency and phase at the transmitter respectfully. At the receiver this waveform is mixed down to a baseband frequency and low pass filtered to obtain,

$$x_{IF}(t) = x(t) \cdot \cos\left(2\pi(f^T - f^R) \cdot t + (\theta_T - \theta_R)\right)$$

where f^R and θ_R are the oscillator frequency and phase at the receiver respectfully.

Ideally oscillator frequency at both ends of the link is constant over time. However in real systems temperature variation and power supply fluctuation cause the oscillator frequency to change. This drifting process can be modeled as,

$$x_{IF}(t) = x(t) \cdot \cos\left(2\pi f_{IF}(t) \cdot t + (\theta_T - \theta_R)\right)$$

95
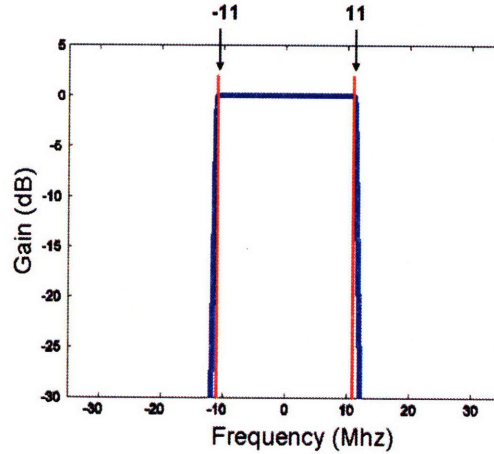
Figure 5-8: Spectrum of Front-End Processed Data $\tilde{x}$

$$f_{IF}(t) = f^T(t) - f^R(t)$$

where the baseband frequency, $f_{IF}(t)$, of the waveform is now a function of time. Specifically this function can be considered to be unknown in general and modeled stochastically as a random walk. Given this formulation we can expect there to be a frequency offset between the matched filters and snapshot as they are obtained under different conditions and time. We will find that this offset must be estimated for both Detection and final Channel Estimation.

5.4.2 Detection Model

Consider a snapshot y. This snapshot maps to a unique member of the following set,

$$y \to s_y \in \{(T, F, W), \phi\}$$

where

$$T = [1, 2, 3, ..., N - M - L + 1]$$

$$F = [F_{min}, F_{max}]$$

$$W = \{w_1, w_2, w_3, ..., w_{128}\}$$

96

This description formalizes the classification of y as being either suitable for channel estimation ($\mathcal{H}_0$), in which case it maps to a point $s_y = (\tau, \rho, \text{w})$ in the space (T,F,W), or unsuitable ($\mathcal{H}_1$) for which y maps to the null element ϕ. Here T represents the set of all possible alignments between snapshot and signal arrival window such that the snapshot contains the entire arrival window. Note that the maximum such value is N-M-L+1[1]. F is the set of all possible baseband frequencies for the channel filtered probing waveform, x, contained in y where F_{min} and F_{max} represent the limits of combined oscillator drift at transmitter and receiver. Lastly W represents the 128-element set of distinct channel sounding waveforms.

5.4.3 Detection Algorithm

In order to realize this classification of the snapshots an algorithm was developed that iteratively searches for a point $\widehat{s}_y = (\tau^d, \rho^d, \text{w})$ that sufficiently approximates the true position $s_y = (\tau, \rho, \text{w})$ of each snapshot in the detection model space. Additionally the algorithm outlines stopping conditions for which the search is aborted resulting in the waveform being classified as unsuitable for estimation, $\widehat{s}_y = \phi$. An iteration of the algorithm completely searches the finite dimensional time-waveform subspace of the detection model space corresponding to a particular frequency. The algorithm is outlined below,

1. **Down-Sample:** The first step in the detection algorithm is to down-sample both the snapshot, y, and the set of 128 matched filters, X (factor of 3). Recall after Front-End Processing both are bandlimited to 11 Mhz while sampled at a rate of 67 Mhz, making them oversampled by a factor of 3. As will be discussed shortly the detection block is the most computationally expensive block of the entire extraction algorithm. This data reduction leads to a large savings in the overall computation of the algorithm. In the final estimation blocks, however, we will not want to make this reduction for several reasons, including aliasing noise and loss of time resolution. However in this stage we are concerned with

---

[1]The signal arrival window and snapshot are of length (samples) M+L and N respectively. Number of integer sample phases between two vectors of size A and B, B < A, is A - B + 1.
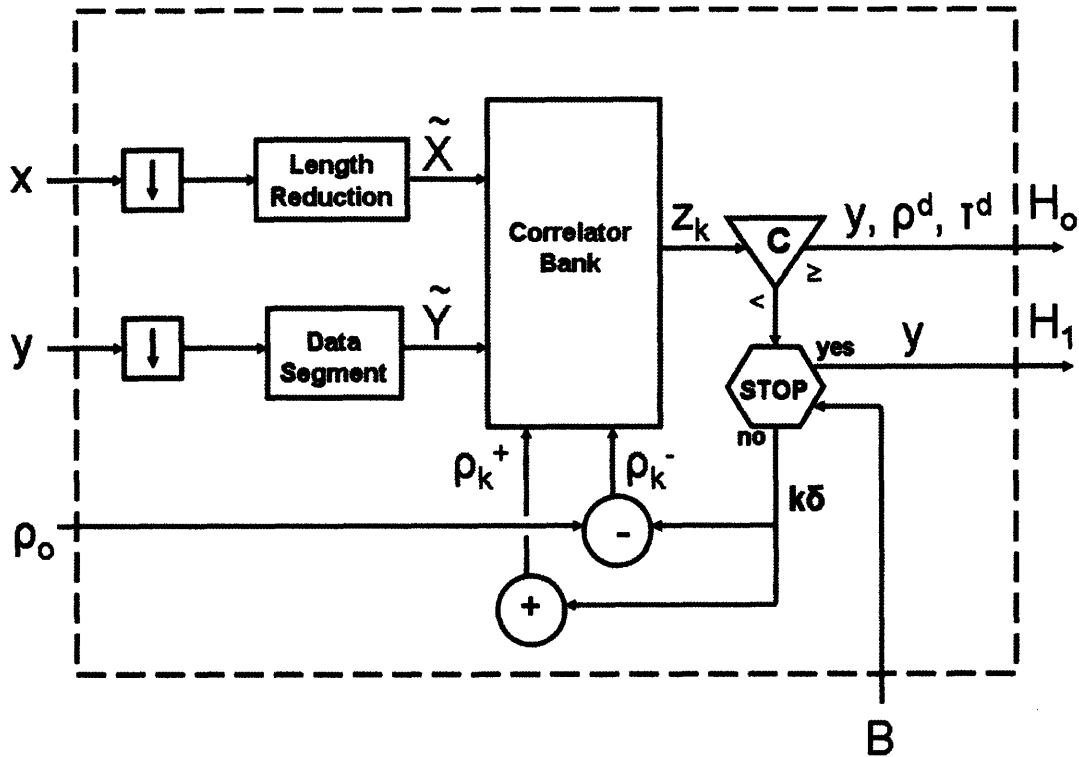
Figure 5-9: The Detection Algorithm

classifying the snapshot and such error sources are negligible in comparison to the computational savings.

2. **Matched Filter Length Reduction:** The next step is to reduce the length of the 128 correlators, X , from a length of M to a length of $\tilde{M} <$ M.

   (a) Operation Count Reduction: The first reason behind reducing the correlator lengths is to reduce the number of complex addition and multiplication operations required for the large number of correlations to follow.

   (b) Frequency Resolution: The second reason is that decreasing the length (time domain) of the correlators (X) also decreases their resolution in the frequency domain. Recalling that the baseband frequencies of the snapshot will be in general offset from that of the correlators implies that the higher the resolution in the frequency domain, the smaller in real frequency this offset needs to be in order to meet a correlation threshold. Consider two
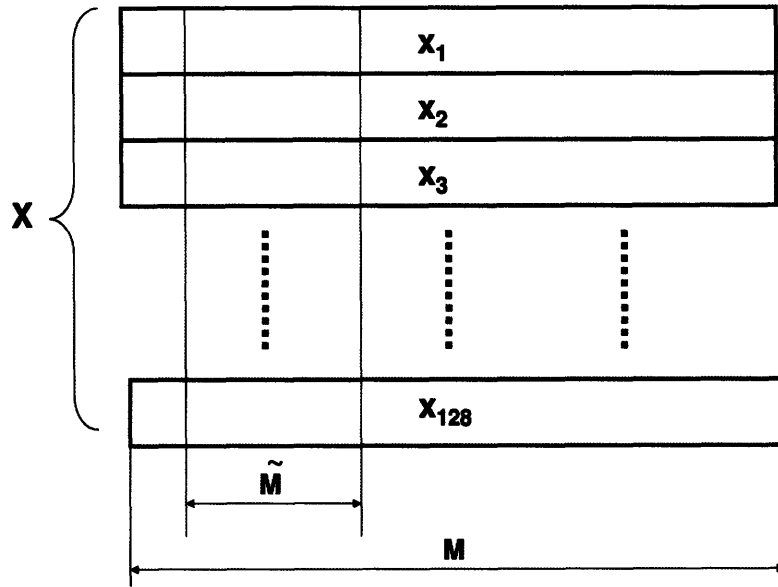
Figure 5-10: Matched Filter Length Reduction

sampled signals a and b of length N such that,

$$b = a \odot \{ e^{j \cdot 2\pi \cdot f_{offset} \cdot \frac{k}{N}} \}_{k=0}^{N-1}$$

where f_{offset} indicates the bin offset in their baseband frequencies, "bin" refers to the sample period of the Discrete Fourier Transform (DFT), which is $\frac{f_{sample}}{N}$ where f_{sample} is the sample frequency of the waveforms. Then their cross-correlation is defined as:

$$\sum_{k=0}^{N-1} a_k^* \cdot b_k = \sum_{k=0}^{N-1} a_k^* \cdot a_k \cdot e^{j \cdot 2\pi \cdot f_{offset} \cdot \frac{k}{N}}$$

If we further model a ϵC^N as a zero-mean, unit-variance discrete stochastic process, which is an accurate representation of the probing waveform, we obtain

$$\mathrm{E}[\sum_{k=0}^{N-1} a_k^* \cdot b_k] = \mathrm{E}[\sum_{k=0}^{N-1} |a_k|^2 \cdot e^{j \cdot 2\pi \cdot f_{offset} \cdot \frac{k}{N}}]$$

$$= \sum_{k=0}^{N-1} \mathrm{E}[|a_k|^2] \cdot e^{j \cdot 2\pi \cdot f_{offset} \cdot \frac{k}{N}}$$

$$= \sum_{k=0}^{N-1} e^{j \cdot 2\pi \cdot f_{offset} \cdot \frac{k}{N}}$$

The magnitude of which is:

$$|\mathrm{E}[\sum_{k=0}^{N-1} a_k^* \cdot b_k]| = |\sum_{k=0}^{N-1} e^{j \cdot 2\pi \cdot f_{offset} \cdot \frac{k}{N}}|$$

$$= |\frac{\sin (\pi \cdot f_{offset})}{\sin (\frac{\pi \cdot f_{offset}}{N})}|$$

$$= N \cdot \mathrm{sinc}(f_{offset})$$

where:

$$sinc(n) = \begin{cases} \frac{\sin(\pi \cdot n)}{\pi \cdot n} & \text{for } n \neq 0 \\ 1 & \text{for } n = 0 \end{cases} \tag{5.7}$$

Thus the correlation between the two signals dampens as a function of baseband frequency offset in DFT bin space. Here we see then that for a constant real frequency offset, the lower the frequency resolution, the higher the correlation will be between the two signals. This then reduces the resolution needed in the frequency search to follow. The reduction in resolution greatly reduces the computation required in the search.

3. **Data Segmenting:** The following step is to segment the snapshot, y, into sections that have the same length as the shortened correlators, $\tilde{X}$. This is simply to save on computation time. As will be explained, the computation bottleneck of the Correlator involves taking the FFT and inverse FFT of the snapshot and matched filters. The FFT is an $\mathcal{O}(N \cdot \log N)$ operation where N

is the sample size of the data. Then,

$$\sum_{i=1}^{T} \frac{N}{T} \cdot \log(\frac{N}{T}) < N \cdot \log(N)$$

$$\Rightarrow N \cdot \log(\frac{N}{T}) < N \cdot \log(N)$$

for T > 1, where T is the number of segments. The set of data burst segments then is denoted as $\tilde{Y} = \{\tilde{y}_t\}_{t=1}^{T}$.
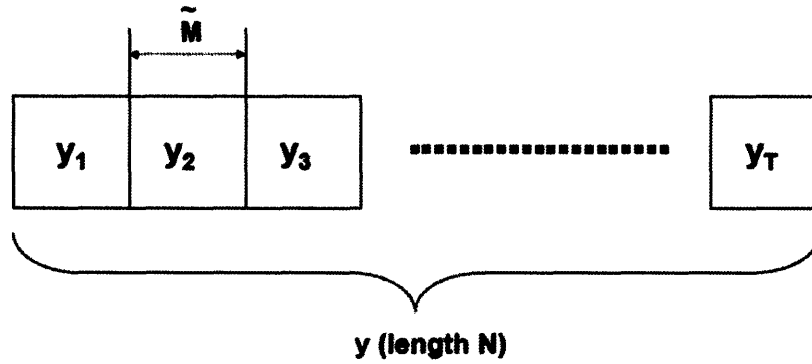
Figure 5-11: Data Segmenting

4. **Correlator:** With 128 matched filters and the snapshot broken into T segments a total of $128 \cdot T$ correlations must be performed for each frequency iteration of the algorithm. A correlation here is defined as a convolution (matched filtering) of a shortened template waveform, $\tilde{x}\epsilon\tilde{X} = \{\tilde{x}_w\}_{w=1}^{128}$ with a data burst segment $\tilde{y}\epsilon\tilde{Y} = \{\tilde{y}_t\}_{t=1}^{T}$,

$$z = \tilde{x} * \tilde{y}$$

where z is the output of the correlator. Convolution is an $\mathcal{O}(n^2)$ operation. So alternatively the operation is performed in the frequency domain as,

$$z = \mathfrak{F}^{-1}\{\mathfrak{F}\{A\} \odot \mathfrak{F}\{B\}\}$$

101

where: where,

$$A = [\tilde{y}^1, \tilde{y}^2, ..., \tilde{y}^{\tilde{M}}, 0, 0, ...0]$$

$$B = [\tilde{x}^{\tilde{M}}, \tilde{x}^{\tilde{M}-1}, ..., \tilde{x}^1, 0, 0, ...0]$$

where the number of zeros padded to the end of A and B is calculated as the smallest number greater than or equal to $\tilde{M}$-1 that makes the total length of A and B a power of two. The $\tilde{M}$-1 minimum is for conversion of the discrete circular convolution to a linear convolution. The power-of-two constraint maximizes the efficiency of the FFT algorithm. Here the computation can be broken down into 3 FFT/IFFT operations with $\mathcal{O}(N \cdot \log N)$ computation and an element-wise vector multiplication of $\mathcal{O}(N)$ computations, resulting in an overall operation count of $\mathcal{O}(N \cdot \log N)$. This is an improvement from the $\mathcal{O}(N^2)$ operations required here for the time domain convolution.

5. **Frequency Search:** As mentioned above, at each iteration i of the detection algorithm a particular frequency, ρ_i, is assumed for the channel-filtered data contained in the snapshot being processed. For this frequency the entire space of possible waveform numbers and time alignments are searched. It is computationally important to search the frequency space efficiently as each iteration requires a large number of correlations. The heuristic used here is to first start at a frequency offset, a seed (ρ_o), that is fed to the detection block. This seed is chosen either according to a priori information on the distribution of the offset or at the very least chosen in the center of the frequency domain, F. The true frequency, ρ, lies in a one-dimensional space corresponding to F= $[F_{min}, F_{max}]$. If subsequent iterations are necessary then this space is searched by moving away from the seed frequency in both directions. The two frequencies checked at iteration k are denoted as:

$$\rho_k^+ = \rho_o + k\delta$$

$$\rho_k^- = \rho_o - k\delta$$

With this search strategy all that remains is the choice of a step size (δ) for the search.

Recalling Equation 5.7, the correlation between two identical sampled signals offset in frequency is a decreasing function of DFT bin offset. The step size then must be chosen in units of DFT bin size such that the correlation for that bin size is acceptably high so as to not step past the real offset. A tradeoff follows though, as choosing smaller step sizes requires more iterations per run, resulting in many more computations. The optimal choice balances both of these concerns and takes into account the system constraints. We found a step size of 0.4 DFT bins works well.

6. **Stopping Conditions:** There are two possible outcomes of the detection algorithm. In the first, $\mathcal{H}_0$, an approximation $\widehat{s}_y = (\tau^d, \rho^d, w)$ to the actual point $s_y = (\tau, \rho, w)$ corresponding to the snapshot y is found, resulting in it being passed on to the next block of the channel extractor. The second outcome is that it is mapped to the null element ϕ (outcome $\mathcal{H}_1$) and discarded. The last component of the algorithm then is to define the rules that determine when conditions have been met resulting in an outcome $\mathcal{H} \epsilon \{\mathcal{H}_0, \mathcal{H}_1\}$ and the termination of the detection block.

(a) **Positive Detection Condition ($\mathcal{H}_0$)**

    i. **Sub-Problem Formulation**

       Each iteration of the algorithm can be considered as a collection of $128 \cdot T_{max}$, ($T_{max} = $ N - L - M + 1), sub-detection problems corresponding to the correlator outputs for each point in the discrete time-waveform space for the current frequency estimate, ρ_k. Each of these sub-problems can be defined as,

$$\tilde{\mathcal{H}}^i = \begin{cases} \tilde{\mathcal{H}}_0 & \text{for } z_i \geq C \\ \tilde{\mathcal{H}}_1 & \text{otherwise} \end{cases}$$

where z_i is the correlation statistic from the ith subproblem, $\tilde{\mathcal{H}}_i$ is the outcome of the ith subproblem, and C is a constant threshold that is fixed according to the requirements of the system. The ith (where i indexes the delay domain) statistic can be expressed as,

$$z_i = \tilde{x}_w^H \cdot \tilde{y}_{(\tau,\rho,w')}$$

where w and w' are the waveform numbers of the template and data respectfully. Additionally (τ, ρ) represent the offset between the channel-filtered waveform contained in y and the corresponding template in time-frequency space. The possibility space can be broken into two cases namely,

ii. **Case I Distribution** (w $\neq$ w')

Here the statistic, z, can be expressed as,

$$z = \tilde{x}_w^H \cdot \tilde{y}_{(\tau,\rho,w')}$$

$$= \tilde{x}_w^H \cdot s + \tilde{x}_w^H \cdot n$$

where $\tilde{x}_w^H$, s, and n are uncorrelated and,

$$E[\tilde{x}] = E[s] = E[n] = 0$$

$$E[|\tilde{x}|^2] = 1$$

$$E[|s|^2] = \sigma_s^2$$

$$E[|n|^2] = \sigma_n^2$$

Here s refers to the contributions of all incoming multipaths of the probing sequence. Using the law of large numbers (LLN) and inde-

pendence of signal and noise we obtain,

$$z \sim \tilde{M} \cdot (\mathcal{CN}(0, \sigma_s^2) + \mathcal{CN}(0, \sigma_n^2))$$

$$\Rightarrow z \sim \mathcal{CN}(0, \tilde{M}(\sigma_s^2 + \sigma_n^2))$$

as the distribution for the statistic in Case I. The variance of this distribution is actually an upper bound as each multipath component may be partially or completely absent from this time window of samples.

iii. **Case II Distribution** (w = w'):

Here the statistic z can be expressed as:

$$z = \tilde{x}^H \cdot \tilde{y}_{(\tau, \rho)}$$

$$= \tilde{x}^H \cdot h \cdot \tilde{x}_\rho + \tilde{x}^H \cdot s + \tilde{x}^H \cdot n$$

where $\tilde{x}$, s, and n have the same marginal distributions as Case I and $|h|^2$ represents the power of the multipath contribution at $\tau=0$. Here s represents all the multipath contributions from taps other than $\tau = 0$, which for the purposes of this analysis can be approximated as being orthogonal to $\tilde{x}$ as the probing sequence is approximately white. Again using the LLN and independence we can re-express this as:

$$z \sim \tilde{M} \cdot (h \cdot \text{sinc}(\rho) + \mathcal{CN}(0, \sigma_s^2) + \mathcal{CN}(0, \sigma_n^2))$$

$$\Rightarrow z \sim \mathcal{CN}(\tilde{M} \cdot h \cdot \text{sinc}(\rho), \tilde{M} \cdot (\sigma_s^2 + \sigma_n^2)) \tag{5.8}$$

Here again this is an upper bound on the variance of the statistic.

iv. **Stopping Rule**

Now recall that we will have $128 \cdot T_{max}$ of these statistics per algorithm iteration corresponding to a particular frequency offset, ρ, between matched filter and snapshot. The function of the positive stopping

condition is to define a rule on these statistics whereby the algorithm terminates in the outcome $\mathcal{H}_0$. Using the sub-problem detection formulation outlined above, each statistic z_i is classified according to the detection rule. There are two outcomes to the stopping rule

A. **Continue**

If all $128 \cdot T_{max}$ statistics are classed as belonging to $\tilde{\mathcal{H}}_1$ then the positive stopping condition is not met and the algorithm continues on to the next stage of execution.

B. **Stop**

If at least one of the $128 \cdot T_{max}$ statistics are classed as belonging to $\tilde{\mathcal{H}}_0$ then the positive stopping condition is met.

v. **Choosing the Detection Threshold** (C)

The last component to completely defining the positive stopping condition is to choose the detection threshold, C. This choice should be dependent on the statistic distributions derived above (see equation 5.8) and the system performance criteria. With the statistic distributions already derived we must then define what the system preferences are. Within this framework there are two kinds of detection error namely,

A. Miss (False Negative)

B. False Alarm (False Positive)

In this system having some misses is acceptable. For every experiment configuration several time snapshots will be taken so that retaining even only 50 percent of the dataset is acceptable as this burden is merely a factor-of-2 computation and storage loss. False Alarms however are not tolerable as the detection stage needs to reliably filter the dataset according to its utility in channel estimation. If even a small percentage of snapshots are false alarms then this can have a large effect on the data analysis to follow. That said, the Maximum

Likelihood detection rule for minimizing the total probability of error is,

$$\tilde{\mathcal{H}}_{ML}^{i} = \begin{cases} \tilde{\mathcal{H}}_0 & \text{for } L(z_i) \geq 1 \\ \tilde{\mathcal{H}}_1 & \text{otherwise} \end{cases}$$

where,

$$L(z_i) = \frac{f(z_i|\tilde{\mathcal{H}}_0)}{f(z_i|\tilde{\mathcal{H}}_1)}$$

$$= \frac{\mathcal{CN}(\tilde{M} \cdot h \cdot \text{sinc}(\rho_{max}), \tilde{M} \cdot (\sigma_s^2 + \sigma_n^2))|z_i}{\mathcal{CN}(0, \tilde{M} \cdot (\sigma_s^2 + \sigma_n^2))|z_i}$$

where ρ_{max} refers to the upper bound frequency offset between template and data at the minimal offset point of the search. This is equal to half the search step. This can be reduced to,

$$= e^{-\frac{(z_i - \tilde{M} \cdot h \cdot \text{sinc}(\rho_{max}))^2}{2\tilde{M} \cdot (\sigma_s^2 + \sigma_n^2)} + \frac{z_i^2}{2\tilde{M} \cdot (\sigma_s^2 + \sigma_n^2)}}$$

Here we see that,

$$L(z_i) > 1$$

$$\Rightarrow e^{-\frac{(z_i - \tilde{M} \cdot h \cdot \text{sinc}(\rho_{max}))^2}{2\tilde{M} \cdot (\sigma_s^2 + \sigma_n^2)} + \frac{z_i^2}{2\tilde{M} \cdot (\sigma_s^2 + \sigma_n^2)}} > 1$$

$$\Rightarrow -(z_i - \tilde{M} \cdot h \cdot \text{sinc}(\rho_{max}))^2 + z_i^2 > 0$$

$$\Rightarrow 2 \cdot z_i \tilde{M} \cdot h \cdot \text{sinc}(\rho_{max}) - (\tilde{M} \cdot h \cdot \text{sinc}(\rho_{max}))^2 > 0$$

$$\Rightarrow z_i > \frac{1}{2} \cdot \tilde{M} \cdot h \cdot \text{sinc}(\rho_{max})$$

The threshold then for the ML detection rule is

$$C = \frac{1}{2} \cdot \tilde{M} \cdot h \cdot \text{sinc}(\rho_{max})$$

This is simply the mid-point between the means of the two distributions corresponding to the two possible cases.

Here we would in theory actually choose a larger threshold given the system constraint that requires low probability of false alarm. However

the realized correlation length $\tilde{M}$ is large enough so that the error of misclassification is already acceptably low that a simple ML detection rule suffices.

(b) Negative Detection Condition $(\mathcal{H}_1)$:

Similarly a stopping rule must be defined for abandoning the search for the point s_y, corresponding to the current snapshot y, resulting in the outcome $(\mathcal{H}_1)$. The idea here is that once the range of plausible frequencies, B= $[B_{min}, B_{max}]$, has been searched it is likely that y does not contain a complete arrival window and hence should be discarded. A definition then is required for what constitutes the range of plausible frequencies. Recall that the drift between oscillators and hence frequency offset between template and data burst can be modeled as a random walk. More specifically this can be expressed as,

$$\rho_n = \rho_{n-1} + \epsilon_n$$

where,

$$\epsilon_n \sim \mathcal{N}(0, \sigma_n^2)$$

$$\sigma_n^2 \sim t_n - t_{n-1}$$

Here ρ_{n-1} corresponds to the most recent frequency offset estimate. This models the current frequency offset, ρ_n, as being equal to the most recently estimated offset plus a gaussian noise term whose variance is proportional to the elapsed time since the transmission of the current data burst and last one to be detected. Given this model we can divide the problem into two cases,

  i. **Case I** $(t_n - t_{n-1} < \tau)$: In the first case the time since the last frequency estimate is small so that the current frequency offset is likely contained in a small interval centered around the last offset.

  ii. **Case II** $(t_n - t_{n-1} >> \tau)$: Here a large amount of time has elapsed

since the last frequency estimate so that the current frequency offset can be expected to be anywhere over the interval $[F_{min}, F_{max}]$ corresponding to the set of realizable frequency offsets.

The following heuristic is then used to choose the initial frequency guess at the beginning of the estimation algorithm,

$$\rho_o = \begin{cases} \rho_{n-1} & \text{for Case I} \\ \frac{F_{max}-F_{min}}{2} & \text{Case II} \end{cases}$$

Similarly the interval of plausible frequencies is defined as,

$$B = \begin{cases} [\rho_{n-1} - \frac{L}{2}, \rho_{n-1} + \frac{L}{2}] & \text{for Case I} \\ [F_{min}, F_{max}] & \text{Case II} \end{cases}$$

The negative stopping condition is invoked when this set of frequencies has been searched.

5.5 Time-Frequency Correction Block

After the detection block those snapshots, y, that meet criteria $\mathcal{H}_0$ are passed to the Time-Frequency Correction Block (TFCB) for further processing. Recall, the detection block provides a point $\widehat{s}_y = (\tau^d, \rho^d, \mathbf{w})$ that approximates the true point $s_y = (\tau, \rho, \mathbf{w})$ corresponding to the snapshot in the unknown time-frequency-waveform space. This space has now been reduced to two degrees of freedom, namely time and frequency, given that the detection stage provides the waveform number exactly (with high probability). The objective of the TFCB then is to improve the time-frequency estimate, (τ^f, ρ^f), using the information provided by the detection block, (τ^d, ρ^d).

5.5.1 Time-Frequency Model

Recalling the extraction model of section 5.1.1, the snapshot, y, can be expressed as,

$$y = s + n$$

where,

$$s_n = \begin{cases} \sum_{m=0}^{M} x_m \cdot h_{n-m-\lceil \frac{\tau}{B} \rceil} & \text{for } n \epsilon [\lceil \frac{\tau}{B} \rceil, \lceil \frac{\tau}{B} \rceil + L + M - 2] \\ 0 & \text{otherwise} \end{cases}$$

in the case of perfect frequency alignment. If we restrict the snapshot to the window $[\lceil \frac{\tau}{B} \rceil, \lceil \frac{\tau}{B} \rceil + L + M - 2]$, we have:

$$y_\tau = y[\lceil \frac{\tau}{B} \rceil, \lceil \frac{\tau}{B} \rceil + L + M - 2] = x * h + n$$

Adding to this model the offset in frequency, ρ, between snapshot and matched filter, we obtain:

$$y_\tau = \sum_{k=0}^{M+L-1} (x * h)_k \cdot e^{2 \cdot \pi \rho \frac{k}{M+L-1}} + n$$

Given this model the goal of the TFCB is to estimate $\tau = \lceil \frac{\tau}{B} \rceil$ and ρ.

5.5.2 Maximum Likelihood Formulation

Consider then the conditional distribution,

$$f_{y_i}(y_i | h_i, x, \rho) \sim \mathcal{CN}(h_i \cdot x_\rho, \sigma_s^2 + \sigma_n^2 \cdot I_M)$$

where,

$$y_i = [y[i], y[i+1], ..., y[i+M-1]] \qquad i \epsilon [\tau_d, \tau_d + L - 1]$$

$$x_\rho = \sum_{k=0}^{M} x_k \cdot e^{2 \cdot \pi \rho \frac{k}{M}}$$

Here, y_i refers to the length-M interval of the snapshot starting at sample i, and h_i, refers to the discrete-time channel tap at that sample. Additionally x_ρ refers to the matched filter contained in the snapshot offset by ρ in frequency. Lastly σ_s^2, σ_n^2 are the powers associated with the total signal and noise respectfully. The maximum likelihood estimator of ρ given y_i, h_i, and x is:

110

$$\widehat{\rho}_{ML} = arg \max_{\tilde{\rho}} f_{y_i}(y_i | h_i, x, \tilde{\rho})$$

$$= arg \max_{\tilde{\rho}} \frac{1}{(2 \cdot \pi)^{\frac{M}{2}} \cdot (\sigma_s^2 + \sigma_n^2)^{\frac{M}{2}}} \cdot e^{-\frac{1}{2}(y_i - h_i \cdot x_{\tilde{\rho}})^H \cdot (I_M(\sigma_s^2 + \sigma_n^2))^{-1} \cdot (y_i - h_i \cdot x_{\tilde{\rho}})}$$

Noting that $\tilde{\rho}$ is contained only in the exponent and that the normal distribution monotonically increases with decreasing exponent absolute value, we have:

$$\widehat{\rho}_{ML} = arg \min_{\tilde{\rho}}(y_i - h_i \cdot x_{\tilde{\rho}})^H \cdot (I_M(\sigma_s^2 + \sigma_n^2))^{-1} \cdot (y_i - h_i \cdot x_{\tilde{\rho}})$$

$$= arg \min_{\tilde{\rho}}(y_i - h_i \cdot x_{\tilde{\rho}})^H \cdot (y_i - h_i \cdot x_{\tilde{\rho}})$$

$$= arg \min_{\tilde{\rho}}[y_i^H y_i - 2y_i^H h_i \cdot x_{\tilde{\rho}} + |h_i|^2 \cdot x_{\tilde{\rho}}^H x_{\tilde{\rho}}]$$

Noting that the first term does not depend on $\tilde{\rho}$ and the last term is a constant, we have:

$$\widehat{\rho}_{ML} = arg \min_{\tilde{\rho}} -2y_i^H h_i \cdot x_{\tilde{\rho}}$$

Note that this objective function is still constrained to be real as the two terms that were dropped are real and the overall cost function is real.

$$\widehat{\rho}_{ML} = arg \max_{\tilde{\rho}} y_i^H \cdot h_i x_{\tilde{\rho}}$$

$$= arg \max_{\tilde{\rho}}[(h_i x_{\rho})^H \cdot h_i x_{\tilde{\rho}} + (s + n) \cdot h_i x_{\tilde{\rho}}]$$

$$= arg \max_{\tilde{\rho}}[\|h_i\|^2 x_{\rho}^H \cdot x_{\tilde{\rho}} + h_i \cdot (s + n) \cdot x_{\tilde{\rho}}]$$

Here note that by the CLT the last term will be approximately gaussian distributed leading to,

$$\widehat{\rho}_{ML} = arg \max_{\tilde{\rho}}(M|h_i|^2 \text{sinc}|\rho - \tilde{\rho}| + \mathcal{N}(0, M|h_i|^2(\sigma_s^2 + \sigma_s\sigma_n))$$

Given that sinc(x) is uniquely maximized at x=0, we see that the first term is maximized for $\tilde{\rho} = \rho$. The second term simply adds noise to the objective function. The SNR of the ML estimator then can be approximated as:

$$SNR_{ML} = \frac{M^2|h_i|^4}{M|h_i|^2(\sigma_s^2 + \sigma_s\sigma_n)}$$

$$= \frac{M|h_i|^2}{\sigma_s^2 + \sigma_s\sigma_n}$$

which results in:

$$\widehat{\rho}_{ML} = \rho + \mathcal{N}(0, \frac{|\rho|^2(\sigma_s^2 + \sigma_s\sigma_n)}{M|h_i|^2})$$

Here we see that the ML estimator of the frequency offset, ρ, is unbiased. Now in this derivation we have implicitly assumed that the tap h_i is known to the estimator. This will not be the case as the channel itself is the unknown parameter of interest for the overall estimation algorithm. Consider instead maximizing over the statistic obtained by correlating y_i with $x_{\tilde{\rho}}$ instead of $h_i x_{\tilde{\rho}}$,

$$= arg \max_{\tilde{\rho}} y_i^H \cdot x_{\tilde{\rho}}$$

The effect of not knowing the channel coefficient is simply a phase rotation of the statistic being maximized. The realized frequency estimator, $\widehat{\rho}$ can then be defined as,

$$\widehat{\rho} = arg \max_{\tilde{\rho}} z(\tilde{\rho})$$

where,

$$z(\tilde{\rho}) = \max(\Re(y_i^H \cdot x_{\tilde{\rho}}), \Im(y_i^H \cdot x_{\tilde{\rho}}))$$

This says find the frequency offset that maximizes the real part of the statistic and additionally find the different frequency offset that maximizes the imaginary part of

the statistic. Then assign the frequency estimate as the one whose statistic is largest. In the worst case the unknown channel tap, h_i, adds a phase shift such that the signal in the statistic has equal energy in both the Real and Imaginary space. In this worst case the SNR of the estimator is half of the ML estimator, leaving:

$$\widehat{\rho} = \rho + \mathcal{N}(0, \frac{2|\rho|^2\sigma_s^2 + \sigma_s\sigma_n}{M|h_i|^2})$$

as the frequency offset estimator distribution.

5.5.3 Defining the Channel Reference Point

Up to this point we have defined the timing of the signal arrival window within the snapshot in such a way that $\tau = \lceil \frac{\tau}{B} \rceil$ is the sample of the snapshot that contains the start of the signal arrival window. The exact reference point for defining the position of the signal arrival window within the snapshot is arbitrary. Referencing according to the beginning of the signal arrival window is not the best as this is difficult to determine with any accuracy. Instead we define the channel reference point (τ) as the snapshot sample that corresponds to the tap, h_l, with the largest magnitude. Namely,

$$\tau = arg\max_l y_l^H \cdot x_{|\rho^d - \rho|}$$

Note that the inner product here is between the snapshot and the matched filter, x, offset in frequency by $|\rho^d - \rho|$. This offset does not affect the maximization as each element, l, is attenuated by the same factor of sinc($|\rho^d - \rho|$). This does decrease the SNR of the statistics being maximized over but at an acceptable level given the level of accuracy provided by the detection block, ρ^d.

5.5.4 Correction Algorithm

Given the above formulation the correction algorithm estimates τ and ρ as (τ^f, ρ^f) by,
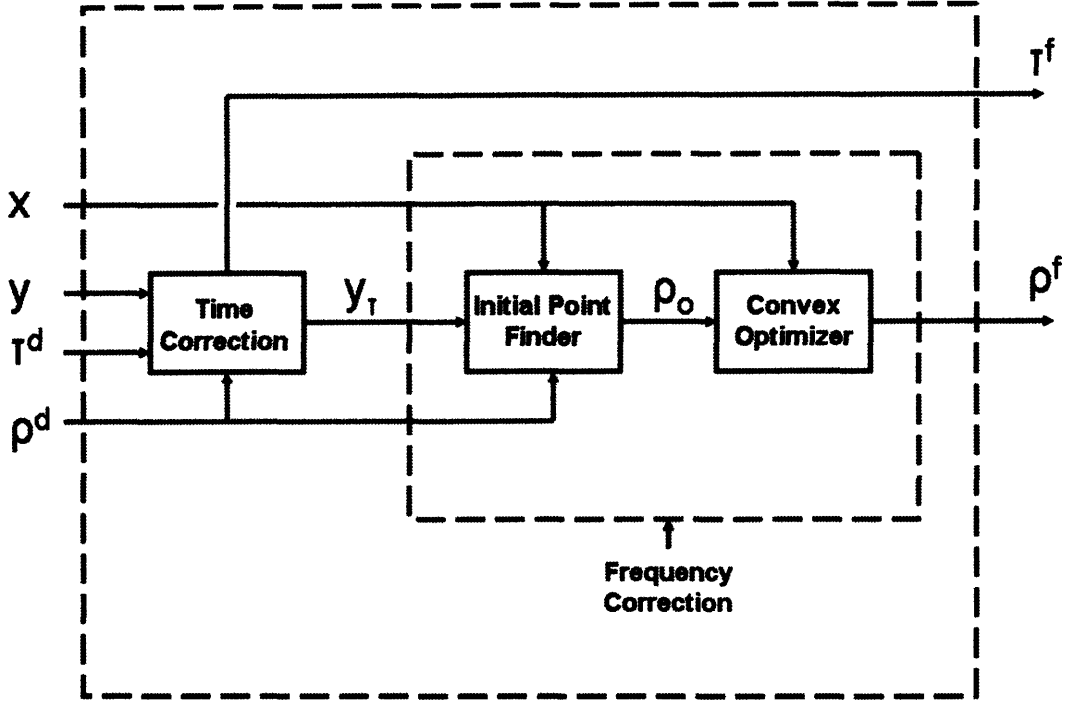
Figure 5-12: The Time-Frequency Correction Algorithm

1. **Time Correction:** The first step of the correction algorithm is to estimate the alignment, τ between snapshot and arrival window as,

$$\tau^f = arg \max_l y_l^H \cdot x_{|\rho^d - \rho|}$$

An interval of the snapshot, y^τ, then is passed on to the next block of the algorithm according to this alignment estimate.

2. **Frequency Correction:** The final step of the correction algorithm is to improve the frequency estimate, ρ^d, by applying the ML estimator derived above. Recall the ML estimator,

$$\hat{\rho}_{ML} = (arg \max_{\tilde{\rho}} M|h_i|^2 \mathrm{sinc}|\rho - \tilde{\rho}|) + \mathcal{CN}(0, M|h_i|^2(\sigma_s^2 + \sigma_s\sigma_n))$$

The ML estimate is found by maximizing over $\tilde{\rho}$ the objective function,

$$c(\tilde{\rho}) = \mathrm{sinc}|\rho - \tilde{\rho}| + \beta(\tilde{\rho})$$

114

where $\beta(\tilde{\rho})$ is a noise term dependent on the choice of $\tilde{\rho}$. This function is concave over the interval [-1 1] (at a resolution on the order of the SNR). The frequency correction algorithm then is composed of two stages. In the first stage an initial estimate ρ_o s.t. $(\rho - \rho_o)\epsilon$ [-1 1] is found. In the second stage a numerical convex optimization algorithm is applied to finish the optimization. The algorithm is,

(a) **Initial Point Finder:** The frequency estimate (ρ^d) from the detection block, the search step size (δ), and detection threshold (C) are used to calculate an interval, F, such that $\rho \epsilon$ F with probability 1.

The objective function, $c(\tilde{\rho})$, is over-sampled by a factor of 2 on the interval F at $\{\tilde{\rho}_i\}_{i=1}^T$

A new parameter estimate is calculated as $\rho_o = \max_i c(\tilde{\rho}_i) \epsilon$ [-1 1] with probability 1.

(b) **Convex Optimization:** Apply the convex optimization algorithm with starting point ρ_o to finish the estimate.

5.6   Channel Estimator

The Channel Estimation block uses the information provided by the detection and correction blocks to complete the estimation of the unknown discrete-time channel vector, h.

5.6.1   Channel Estimation Model – Frequency Domain

Here we now assume that the timing, frequency, and waveform information are known exactly and that the snapshot, y, has been corrected accordingly. The discrete-time channel model now is,

$$y = h * x + n$$

where y ϵ C^{M+L-1}, x ϵ C^M, h ϵ C^L Similarly we can consider this model in the frequency

domain as,

$$\mathfrak{F}(y) = \mathfrak{F}(h * x + n)$$

$$\Rightarrow Y = H \odot X + N$$

where, $\mathfrak{F}(\cdot)$ is the discrete fourier transform (DFT). We can now equivalently define the channel estimation problem as that of estimating the channel frequency response H, given Y and X.

5.6.2 Model Adjustment – Packet Headers

The Channel Data Collection System (CDCS) forces a slightly different model than above. The probing sequence, x, is a standard 802.11b packet which includes an unknown header on the front and back of the waveform,

$$p = [h_{front} \quad | \quad x \quad | \quad h_{back}]$$

where, h_{front}, h_{back} are the unknown fixed-length header components of the packet, p. The headers here can be treated as noise so we would like to minimize their effect on the channel estimation. To do this the timing information obtained from the detection/correction blocks is used to limit the estimation over a time interval that does not contain the main contributions of these headers. In this framework the channel model becomes:

$$y = Ah + n$$

where,

$$A = \begin{pmatrix} x_L & x_{L-1} & x_{L-2} & \cdots & x_1 \\ x_{L+1} & x_L & x_{L-1} & \cdots & x_2 \\ \vdots & \vdots & \vdots & \vdots & \vdots \\ x_{L+\tilde{M}-1} & x_{L+\tilde{M}-2} & x_{L+\tilde{M}-3} & \cdots & x_{\tilde{M}} \end{pmatrix}$$

with $y, n \epsilon \mathcal{C}^M$ and $h \epsilon \mathcal{C}^L$. Here $\tilde{M}$=M - L +1 is the adjusted correlator length due to decreasing the time window to remove all header contributions. Equivalently we can

116

convert this model to the frequency domain by noting that y is a linear combination of noise and the columns of A, we obtain:

$$\mathfrak{F}(y) = \mathfrak{F}(A)h + \mathfrak{F}(n)$$

,

$$\Rightarrow Y = fA \cdot h + N$$

where fA denotes the column-wise DFT of A,

$$fA = \begin{pmatrix} X_L & X_{L-1} & X_{L-2} & \ldots & X_1 \\ X_{L+1} & X_L & X_{L-1} & \ldots & X_2 \\ \vdots & \vdots & \vdots & \vdots & \vdots \\ X_{L+\tilde{M}-1} & X_{L+\tilde{M}-2} & X_{L+\tilde{M}-3} & \ldots & X_{\tilde{M}} \end{pmatrix}$$

5.6.3 Least-Squares Estimator (OLS)

Given the above model the least squares estimator of the discrete channel impulse response is,

$$\widehat{h}_{OLS} = ((fA)^H fA)^{-1}(fA)^H Y$$

The noise, N, can be approximated as having a gaussian distribution in both the time and frequency domain. That said, the OLS estimator, $\widehat{h}_{OLS}$, is the minimum variance estimator of h in this model.

5.6.4 Frequency Resolution

The resolution of the channel estimate in the frequency domain is limited by $\frac{B}{L}$ where B is the bandwidth of the system and L the length of the estimate of the channel vector, h. There is a tradeoff between the resolution of the estimate and its accuracy. The higher the resolution the higher the variance in the estimation. The need for resolution though is determined by the propagation characteristics of the channel environment being measured. So long as the resolution of the estimator is smaller

than the coherence bandwidth of the channel, the channel over a frequency window with that resolution can be approximated as being flat (constant). The method used then here is to reduce the frequency resolution by an integer factor K such that $\frac{B}{L \cdot K}$ is larger than the coherence bandwidth of the channel being measured.

5.6.5 Sub-Problem Formulation

Let K denote the integer factor of resolution reduction in the frequency domain. Consider then the estimation model over a frequency window of length K starting at sample i in the frequency domain,

$$Y_i^K = f A_i^K \cdot h_i + N_i^K$$

$$\Rightarrow \begin{pmatrix} Y_i \\ Y_{i+1} \\ \vdots \\ Y_{i+K-1} \end{pmatrix} = \begin{pmatrix} X_{L+i-1} & X_{L+i-2} & \cdots & X_i \\ X_{L+i} & X_{L+i-1} & \cdots & X_{i+1} \\ \vdots & \vdots & \vdots & \vdots \\ X_{L+i+K-2} & X_{L+i+K-3} & \cdots & X_{i+K-1} \end{pmatrix} \cdot \begin{pmatrix} h_i^1 \\ h_i^2 \\ \vdots \\ h_i^L \end{pmatrix}$$

$$+ \begin{pmatrix} N_i \\ N_{i+1} \\ \vdots \\ N_{i+K-1} \end{pmatrix}$$

Here h_i denotes the discrete-time channel impulse response over this limited bandwidth. If we assume that K is sufficiently small that the channel is flat over this bandwidth we can reduce this to:

$$Y_i^K = X_i^K \cdot H_i + N_i^K$$

where, $Y_i^K, X_i^K, N_i^K \epsilon \mathcal{C}^K$ and $H_i \epsilon \mathcal{C}^1$ corresponds to the channel frequency response of this narrow bandwidth. The least-squares (OLS) estimator of the ith frequency tap,

118

H_i, is then,

$$\widehat{H}_i^{OLS} = ((X_i^K)^H X_i^K)^{-1}(X_i^K)^H Y_i^K$$

5.6.6 Channel Estimation Algorithm
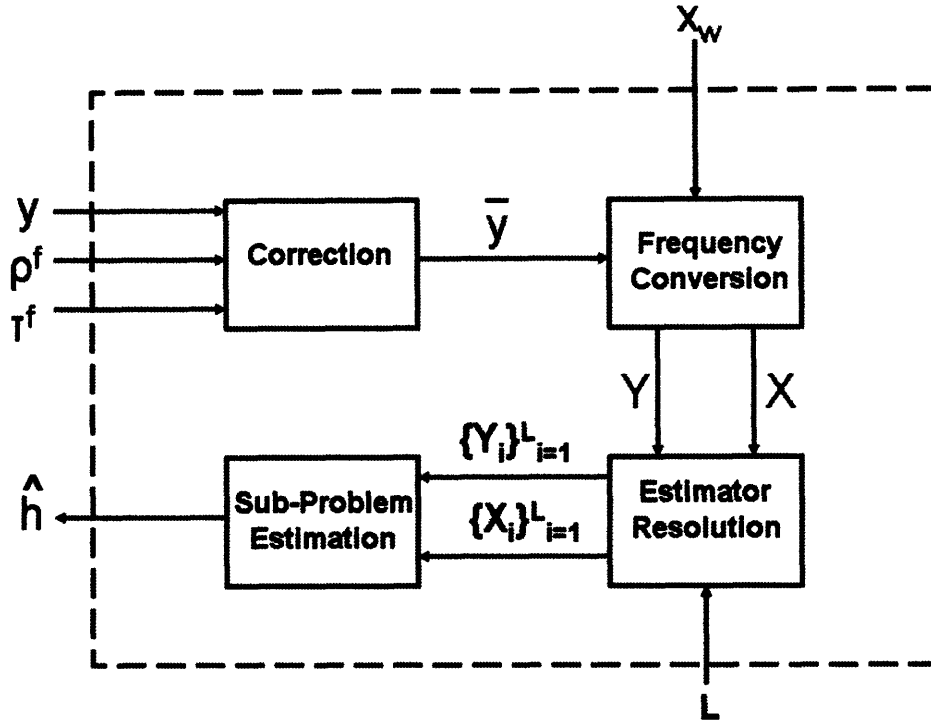
Figure 5-13: The Channel Estimation Block

With the above formulation the channel estimation algorithm then operates by,

1. **Correction:** First the snapshot, y, is corrected using the time-frequency esti-
   mates provided by the correction block (τ^f, ρ^f) to obtain $\bar{y}$.

2. **Frequency Correction:** The corrected snapshot, $\bar{y}$, and appropriate matched
   filter x_w are converted to their frequency-domain counterparts Y and X.

3. **Estimator Resolution:** The snapshot and matched filter are partitioned into
   narrow-band segments according to the desired frequency resolution for the
   estimator.

119

4. **Estimator Resolution:** The channel frequency response, $H=\mathfrak{h}$, is estimated by applying the least-squares estimator derived above to each narrow-band partition.

5.7 Iterative Estimation Algorithm

We now combine all of these components into a complete algorithm that, given a set of raw channel data, $\{y_k\}_{k=1}^{T}$ (T= number of snapshots), extracts the channels h_k corresponding to those snapshots y_k that meet the sufficiency criteria. Note that the snapshots from each receiver channel are processed together as the timing, frequency, and waveform information of each channel is related. The extraction algorithm proceeds by,
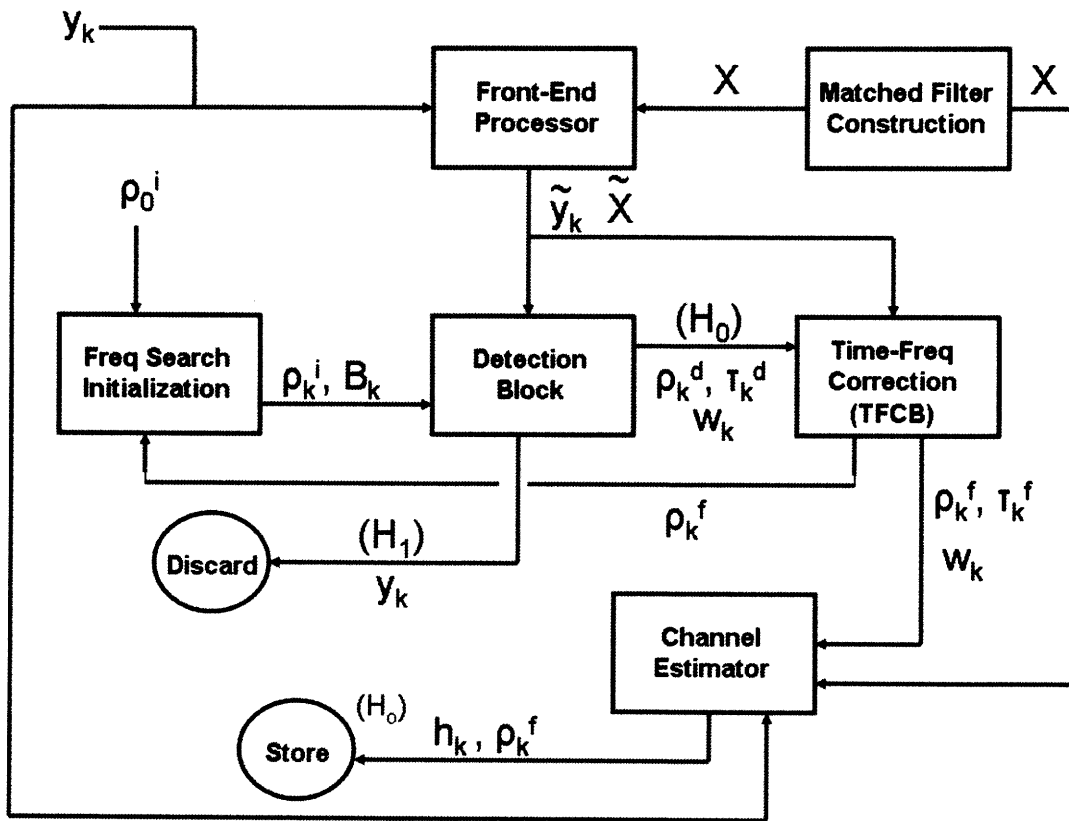
Figure 5-14: Full Extraction-Estimation Algorithm

1. Initial Preprocessing (Performed Once)

Table 5.1: Estimator Symbol Definitions

Parameter	Definition
y_k	snapshot (k^{th} of T)
X	128 Matched Filters
$\tilde{y}_k$	Front-End processed snapshot
$\tilde{X}$	Front-End processed matched filters
ρ_k^i	Initial Frequency Estimate
B_k	Frequency Search Window (k^{th})
τ_k	True Timing Offset
τ_k^d	Detection Block Timing Estimate
τ_k^f	TFCB Timing Estimate
ρ_k	True Frequency Offset
ρ_k^d	Detection Block Frequency Estimate
ρ_k^f	TFCB Frequency Estimate
w_k	True Waveform Number
h_k	channel estimate (k^{th})

   (a) The 128 matched filters, X, are constructed

   (b) The default initial frequency estimate, ρ_0^i, is chosen.

2. The initial frequency estimate (ρ_k^i) and search window (B_k) for the current snapshot, y_k, is chosen according to the Frequency Initialization Block.

3. The current snapshot y_k and set of 128 matched filters X are processed by the Front-End Processor to obtain $\tilde{y}_k, \tilde{X}$.

4. Given the matched filter set $\tilde{X}$, the Detection Block filters the current snapshot ($\tilde{y}_k$) according to,

   (a) $\mathcal{H}_0$: The snapshot(y_k), Detection Block frequency offset estimate (ρ_k^d), detection block timing estimate (τ_k^d), and waveform number estimate (w_k) are passed to the time-frequency correction block.

   (b) $\mathcal{H}_1$: The snapshot (y_k) is discarded and the algorithm returns to step 2 of iteration k+1.

5. Given the matched filters and information provided by the Detection Block, the final frequency (ρ_k^f) and timing (τ_k^f) estimates are computed by the Time-

Frequency Correction Block. These estimates along with the current snapshot (y_k) and correct matched filter (x_w) (w= waveform number) are passed to the Channel Estimation Block. Additionally the final frequency offset estimate (ρ_k^f) is passed to the Frequency Initialization Block for use in subsequent iterations.

6. The Channel Estimation Block estimates the channel (h_k) corresponding to the current snapshot. This estimate along with the final frequency offset estimate (ρ_k^f) are stored to disk. The algorithm then returns to step 2 for iteration k+1.

5.8 Channel Extraction Performance Analysis

In this section we define and measure the performance of the channel extraction algorithm. First an upper bound on performance is obtained corresponding to ideal system conditions. Next an experiment is presented for measuring the performance of the algorithm, the results of which are then compared to the upper bound. Lastly the difference between realized and ideal performance is analyzed.

5.8.1 Performance Upper Bound

The collection system and extraction algorithm are considered to display ideal behavior if at the channel estimation block of the algorithm, the model,

$$\Rightarrow Y = fA \cdot h + N$$

holds exactly, where,

$$N \ \mathcal{CN}(0, \sigma_N^2)$$

For this to be the case the following must be true,

1. The system is perfectly linear over the pass-band.

2. The channel and system noise can be modeled as additive white gaussian noise.

3. The correction algorithm estimates perfectly the waveform number, time alignment offset, and frequency offset.

Recalling the sub-problem formulation, the ith frequency tap of the channel is estimated as,

$$\widehat{H}_i^{OLS} = (X^H X)^{-1}(X)^H Y$$

where[2] $X, Y \epsilon \mathcal{C}^K$ and K is the frequency resolution reduction factor. Note the subscripts have been dropped from before. This results in:

$$\Rightarrow \widehat{H}_i^{OLS} = (X^H X)^{-1}(X^H X) \cdot H_i + (X^H X)^{-1} X^H N$$

$$= H_i + (X^H X)^{-1} X^H N$$

Here we see that $\widehat{H}_i^{OLS}$ is a linear combination of i.i.d. gaussian distributed random variables and thus also is gaussian distributed. All that remains then to fully describe the estimator distribution is to find the mean and variance,

$$E[\widehat{H}_i^{OLS}] = E[H_i] + E[(X^H X)^{-1} X^H N]$$

$$= H_i + (X^H X)^{-1} X^H E[N]$$

$$= H_i$$

$$Var[\widehat{H}_i^{OLS}] = Var[H_i + (X^H X)^{-1} X^H N]$$

$$= Var[H_i] + Var[(X^H X)^{-1} X^H N]$$

$$= 0 + \frac{\sum_{i=1}^{K} Var[X_i^* N_i]}{(\sum_{i=1}^{K} X_i^* X_i)^2}$$

$$= \frac{\sum_{i=1}^{K} X_i^* X_i \sigma_N^2}{(\sum_{i=1}^{K} X_i^* X_i)^2}$$

$$= \frac{\sigma_N^2}{\sum_{i=1}^{K} X_i^* X_i}$$

---

[2]OLS: Ordinary Least-Squares

which for X normalized is,

$$\approx \frac{\sigma_N^2}{K}$$

The distribution of the estimator is then,

$$\widehat{H}_i^{OLS} \sim \mathcal{CN}(H_i, \frac{\sigma_N^2}{K})$$

The signal-to-noise ratio of which is,

$$SNR_{estimator} = \frac{|H_i|^2 \cdot K}{\sigma_N^2} = K \cdot SNR_{data}$$

This is then an upper bound on the accuracy of the estimator. The upper-bound follows from the additional possibility of frequency correction error.

5.8.2 Measuring Performance

In order to compare the performance of the algorithm to this upper bound an experiment has been devised. The experiment proceeds by,

1. As with the matched filter construction, directly connect the transmitter to each receiver channel via coax cable and an 8-to-1 power divider forming a wired channel.

2. Collect T (≈ 100) snapshots at each of a discrete set of transmit power levels that span the dynamic range of the system.

3. Process this data set with the channel extraction algorithm obtaining the associated channel estimates.

4. Correct the channel estimates associated with each power level. That is, correct for the random linear phase difference (due to sub-sample mis-alignment and tx/rx incoherency) between each snapshot of a given power level.

5. Calculate the variance of the channel estimates for each power level.

6. Calculate the SNR of the estimates for each power level as the the mean power of the estimates divided by the variance calculated in the previous step.

7. Display the SNR of the power level estimates as a function the SNR of the snapshots at that power level and compare to the theoretical upper bound.
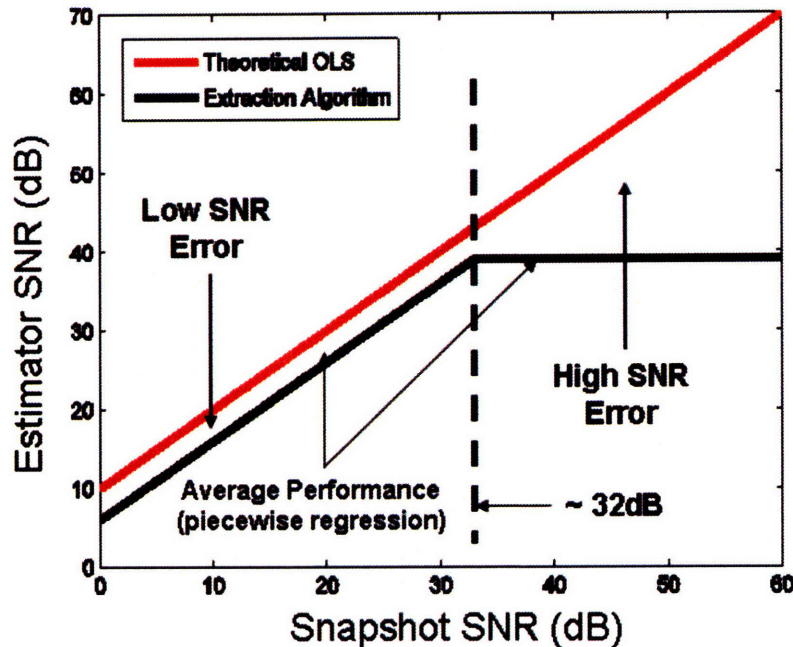
Figure 5-15: Channel Extraction Performance

5.8.3 Error Analysis

Figure 5-15 displays [3] the results of this experiment and Table 5.2 lists the relevant system and estimator parameters. In Table 5.2 we see that the estimator resolution reduction factor (K) is 10, giving an upper bound performance of $SNR_{snapshot}$ + 10dB.

From this analysis we see two sources of divergence between the benchmark OLS performance and that of our extraction algorithm. The first source of divergence dom-

---

[3]Extraction algorithm performance extrapolated from the results of the experiment defined in Section 5.8.2

125

Table 5.2: Channel Estimation System Parameters

Parameter	Value
Estimator Bandwidth	10Mhz
System Frequency Resolution	3.3KHz
Resolution Reduction Factor (K)	10
Estimator Resolution	33.3 KHz
Estimator Delay Window	9km
Estimator Delay Resolution	30m

inates for low-SNR snapshots ($<$ 32dB SNR) and the second for high-SNR snapshots ($>$ 32dB SNR). In the low-SNR snapshot regime our estimation algorithm performs about 3-4dB worse that OLS. This can be attributed to the fact that the matched filters used in our algorithm were measured and thus contain system thermal noise. This essentially reduces the SNR of our data by a factor of 2 (3dB), which helps to explain this behavior. In order to reduce this source of error we could have averaged the matched filters over many snapshot measurements. However this would have required phase, time, and frequency alignment before they could be coherently added. The noise in this process along with other system noise factors made reducing the noise by a few dB not worth the cost.

In the high-SNR snapshot regime our estimation algorithm is limited to approximately 40dB performance. This source of error most likely can be attributed to the limited accuracy in our time and frequency error correction. Additionally given the non-ideal behavior of the oscillators in our system, intra-snapshot frequency jitter limits our performance. That said, the performance of our algorithm is more than sufficient for the purposes of this research.

Chapter 6

Power Attenuation

6.1 Background

Understanding realized path-loss behavior is critical for deploying wireless networks so that tradeoffs can be calculated for such system parameters as transmission power and node spacing. Modeling of path-loss characteristics usually comes in one of three forms, namely: deterministic, stochastic, or empirical models. Deterministic modeling assumes that a large amount of information about the propagation environment is known so that electromagnetic propagation laws can be used to deterministically calculate the power attenuation. The most widely used of these models is in the ray tracing regime [29], [30], [31]. The opposite extreme to deterministic modeling is that of stochastic models. Here we assume that the affect of the environment on the propagation path has a random structure. An example is the log-normal fading model, which models the power attenuation as having a log-normal distribution [8]. Lastly empirical models attempt to model path-loss as following a series of equations based on real channel measurements. The most widely used of which include the Stanford University Interim (SUI) [33], Hata [14] [15], and COST-231 models [34]

The above empirical models either include correction factors for operating frequency or state that their applicability is limited to a specific set of frequencies. Here we are specifically interested in studying the relationship between path-loss and link-length. Our analysis in this regime is independent of operation frequency and

can be combined with any frequency dependence correction model for such specific needs. That said, the r^α attenuation model is widely assumed in the literature [9] and presented as the fundamental model for path-loss as a function of distance in many popular texts on wireless communication [6], [8]. In the empirical models above an average value for α is assumed that, depending on the model, may vary as a function of environment type and antenna heights.

Here we want to first ask under what channel conditions, e.g. link lengths, environments, is the r^α attenuation model an accurate representation of reality? Instead of just assuming an r^α relationship and utilizing a parameter value for α that meets some criteria (e.g. least-squares fit) we want to study what the limitations are of the model and how to best apply it to match real channel behavior.

Additionally, in contrast to empirical models which assume a fixed path-loss coefficient for a given environment type, we want to study the stationarity of the model. The attenuation model is parameterized by a single parameter, α. Model stationarity is then defined as the stability of the path-loss coefficient α over localized propagation environments.

Under non-stationary conditions where α does vary under similar environment types we would like to ask what are the key physical characteristics of the environment that affect α? Given this characterization, can we predict α by observing these physical attributes? Are there simple physical models that predict α? This will help us to understand if we can relax the amount of information required in ray-tracing methods while retaining much of their predictive power. Additionally we look at the applicability of stochastic based models where such predictive capability is not available.

Lastly we divide our link study into two operating regimes, namely: ground-to-ground and air-to-ground. We claim that the majority of wireless applications fall clearly into one of these two categories and given the difference in the physical propagation mechanisms between the two, as explained in the next sections, it is best to study each separately.

6.2 Measurement Campaign and Setup

To facilitate our study we designed the following measurement campaign and system setup for collecting the appropriate wireless channel data.

1. **Transmitter**

    (a) **Antenna Element:** One 8dBi dipole

    (b) **Antenna Polarization:** Vertical

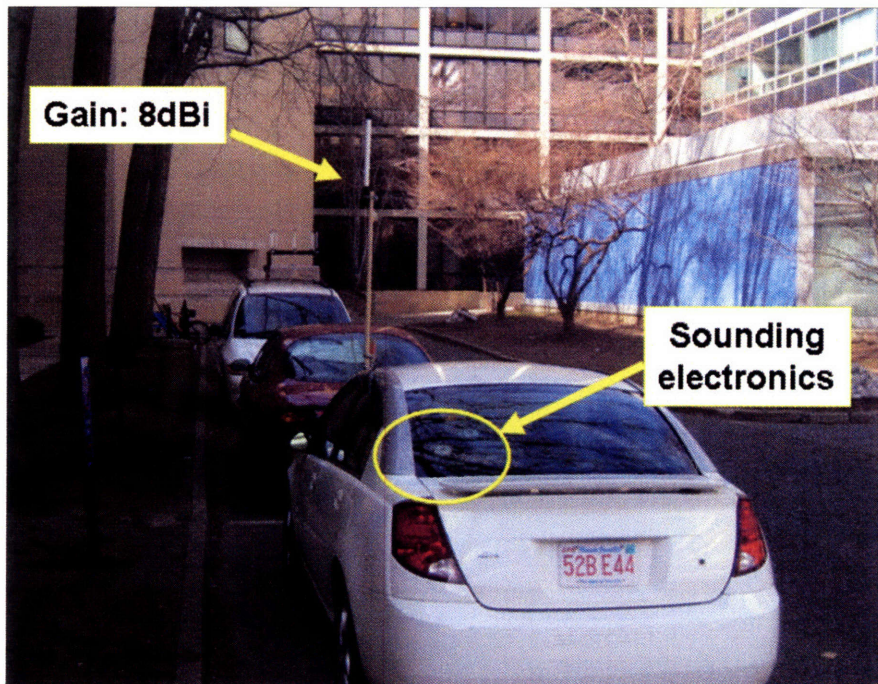Figure 6-1: The mobile transmitter setup for Ground-To-Ground propagation experiments: Signal generation electronics housed in car interior; Roof-Mounted antenna

    (c) **Mounting:** Electronics housed in Saturn ION, with antenna mounted several feet above the roof of the vehicle. See Figure 6-1

2. **Receiver**

    (a) **Antenna Elements:** Eight 8dBi dipoles

    (b) **Antenna Polarizations:** Vertical (All 8)
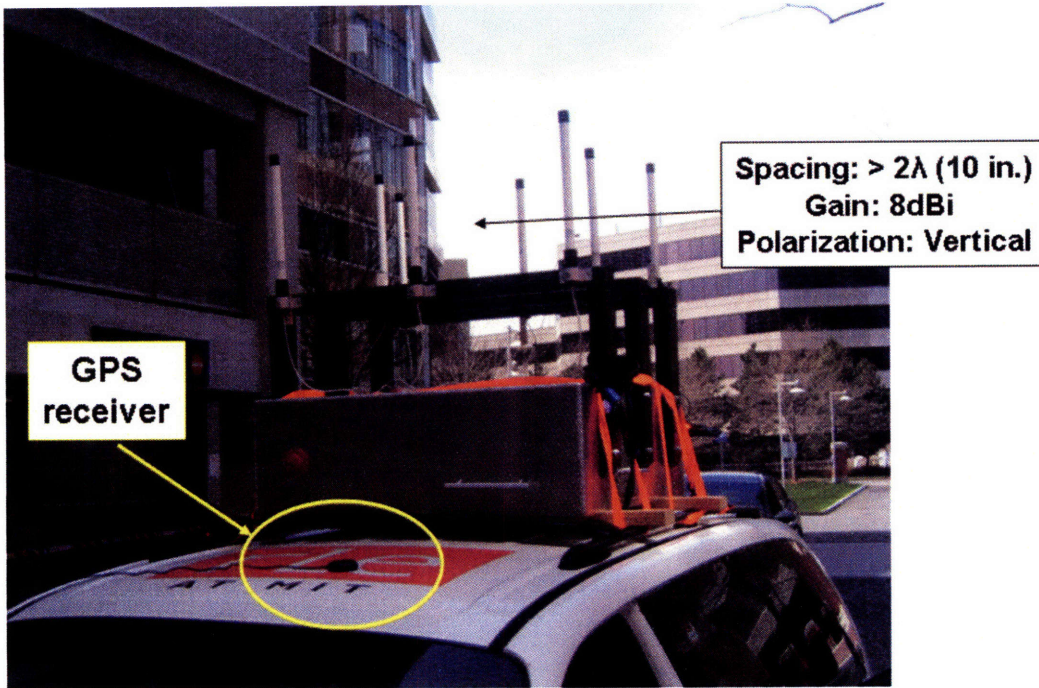
Figure 6-2: Receiver mounted to van – Front view and GPS receiver

    (c) **Antenna Array**: Each element spaced by more than several wavelengths so as to obtain independent channel measurements. See Figure 6-3

    (d) **Mounting**: System installed in van with receiver mounted to the roof of the van. See Figures 6-2, 6-4, and 6-5.

3. **Measurement Procedure:** Car housing transmitter parked and left stationary. Van housing receiver takes measurements around environment local to the transmitter. Van is stationary for each channel snapshot measurement.

4. **Environments:** MIT Campus and parts of Cambridge between MIT and Harvard. See Figure 6-6.

6.3   Performance and Stability of the r^α Model

Our first research objective was to test the performance and stability of the r^α path-loss model. In this study we found that the path-loss coefficient, α, can change dramatically between environments even in cases where they are physically adjacent
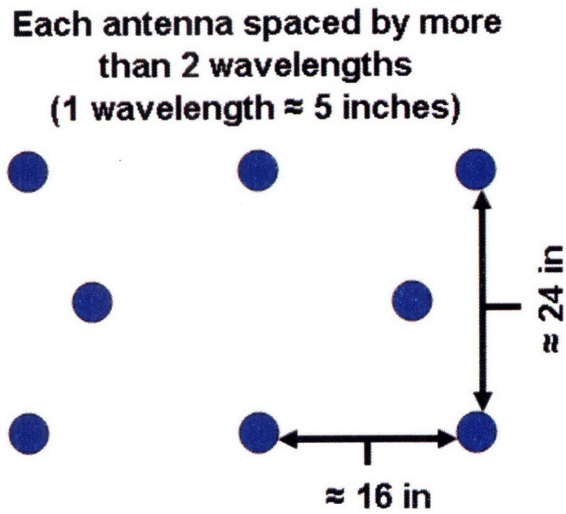
Figure 6-3: Receiving Array Topology

to one another. Figure 6-7 illustrates this non-stationary behavior of α by displaying a scatter plot of power received (dBm) versus link length (on a dB scale relative to one meter) over a typical residential neighborhood.

This data was collected over a radius of several city blocks. The transmitter remained in the same (single) location for the duration of the experiment while the receiver traversed the neighboring streets local to the transmitter location. Here we see a large variance in the relationship between received power and distance as different sections of the neighborhood are reached. This suggests that assuming a specific value for α for a particular environment and set of antenna heights, as is done in the popular empirical models, can lead to large miscalculations. For link lengths of this size ($<$ 1km) this is not surprising as the attenuation is dominated by a few objects in the environment. In such an environment it is common for the number of objects between transmitter and receiver to vary significantly as a function of direction, leading to such fading behavior.

Given this result it is of interest to consider instead path-loss over smaller stationary regions individually. Here by stationary region we are referring to a subregion of the environment where the path-loss is relatively constant. With this approach we can then compare the path-loss coefficient, α, between stationary regions and develop
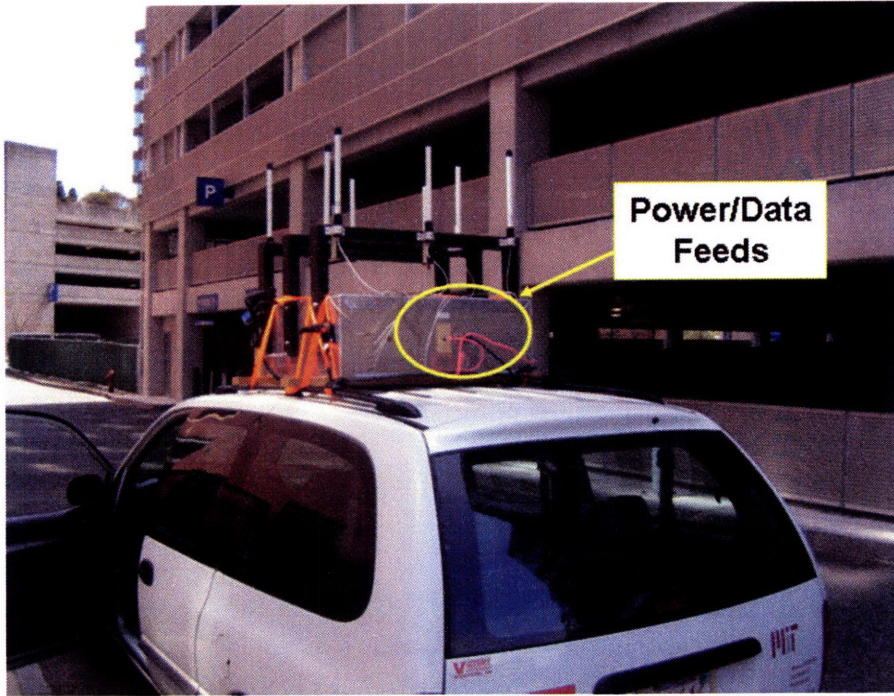
Figure 6-4: Receiver mounted to van – Rear view

physical models for path-loss based on the variation in physical characteristics among regions.

Here we have taken such an approach. The first step is to define a stationary region. In urban areas a single street with homogeneous physical features along its length is a typical environment. To explore the relationship between path-loss and the physical characteristics of such environments, several streets in the MIT and greater Cambridge area were chosen as measurement locations. At each site the transmitter was parked around a corner so that any energy entering the street was forced to do so indirectly by reflecting or scattering from objects in the environment. Given this setup the van housing the receiver was driven down each street with channel snapshots taken at regular intervals. Figures 6-8, 6-9, and 6-10 display measurements taken at three representative street locations.

These figures display the power received as a function of distance (on a dB scale). As displayed in each figure, the path-loss coefficient for each environment was estimated as the least squares linear regression fit to each scatter plot. The calculated
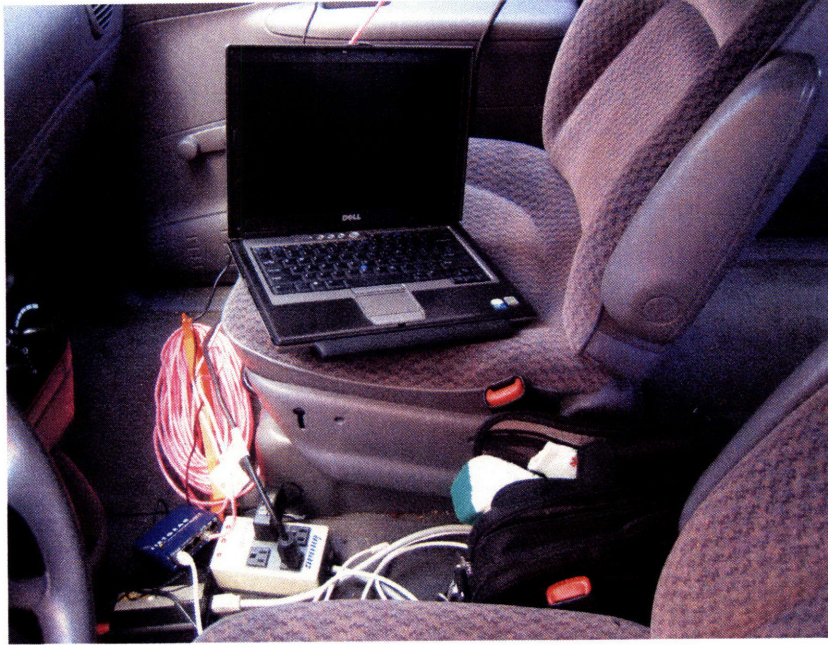
Figure 6-5: Receiver control from van interior.

α's in the environments measured were in the range of 2 to 5. Here we see that the r^α model is quite good for sub-kilometer link lengths when the region is physically homogeneous. However, when used outside of this context the model will likely be quite inaccurate as seen in Figure 6-7.

6.4 Predicting α from the Environment

In Section 6.3 we showed that the r^α model performs well when restricted to physically homogeneous sub-regions of the environment. Given this it would be beneficial if we could predict α for a particular sub-region based on a partial description of its physical characteristics. If prediction is possible then we can use this as a basis for path-loss models.

To test the predictive utility of environmental parameters we return to our data set collected along streets in Cambridge and MIT. Physically the streets can be thought of as behaving as a lossy waveguide for the multipath components (MPCs) between transmitter and receiver. As the receiver moves down the street the signals must

Figure 6-6: Measurement Environments

reflect and scatter off the buildings lining the street in order to reach the receiver. A natural physical parameter for predicting path-loss then would be one that captures the quality of this waveguide. Here we consider two metrics that are based on the amount of gaps along the street. Specifically we define the following function for points x along the street,

$$
\text{Gap(x)} = \begin{cases} 0 & \text{if both sides of street at point x contain buildings} \\ 1 & \text{if exactly one side of the street at point x contains a building} \\ 2 & \text{if neither side contains a building} \end{cases}
$$

where the depth of a building (distance from street to front building surface) must be close (on the order of 10 meters) to the average building depth for that street to be considered in the above calculation, i.e. if a building sits far back from the street relative to the other buildings along the street then it is considered as being a gap. Figures 6-11 and 6-12 display satellite imagery of two example streets and their corresponding evaluations of Gap(x). The two metrics we consider are,

134
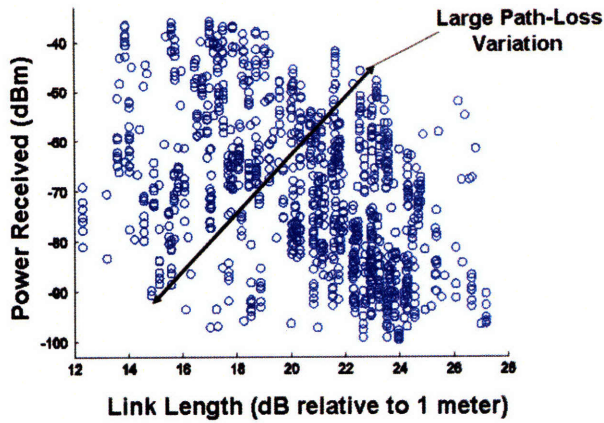
Figure 6-7: Path-Loss: Non-stationarity
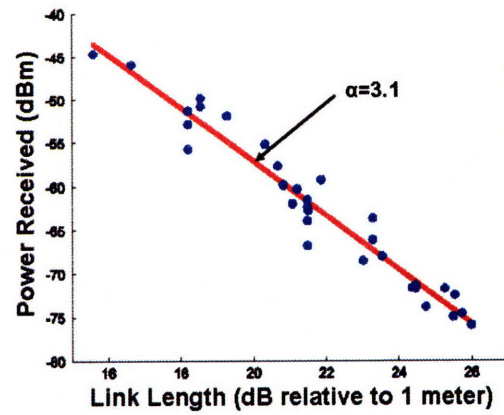
Figure 6-8: Path-Loss over single street
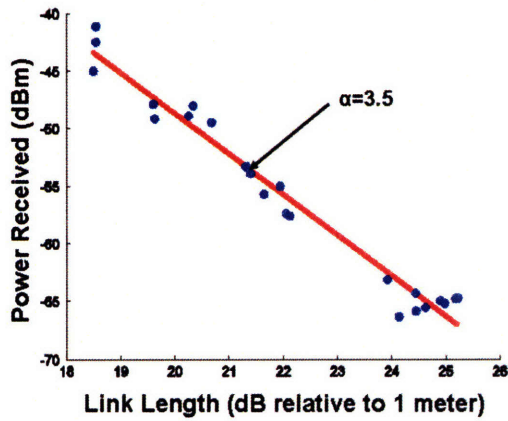
Figure 6-9: Path-Loss over single street
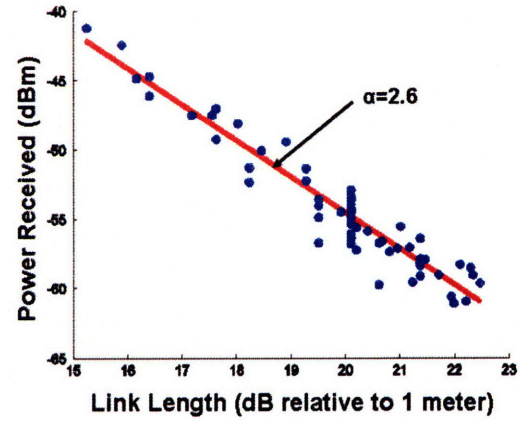
Figure 6-10: Path-Loss over single street

P_1 = Average gap percentage along each side of street

$$= \frac{1}{2|start - end|} \int_{x=start}^{end} Gap(x)dx$$

P_2 = Percentage of points along the street with gap on at least one side of the street

$$= \frac{1}{|start - end|} \int_{x=start}^{end} I(Gap(x) > 0)dx$$

$$I(Gap(x) > 0) = \begin{cases} 1 & \text{if Gap(x) > 0} \\ 0 & \text{else} \end{cases}$$

To test the utility of these two metrics in estimating the path-loss coefficient α we have constructed scatter plots, see Figures 6-13 and 6-14, of α versus each utilizing

135
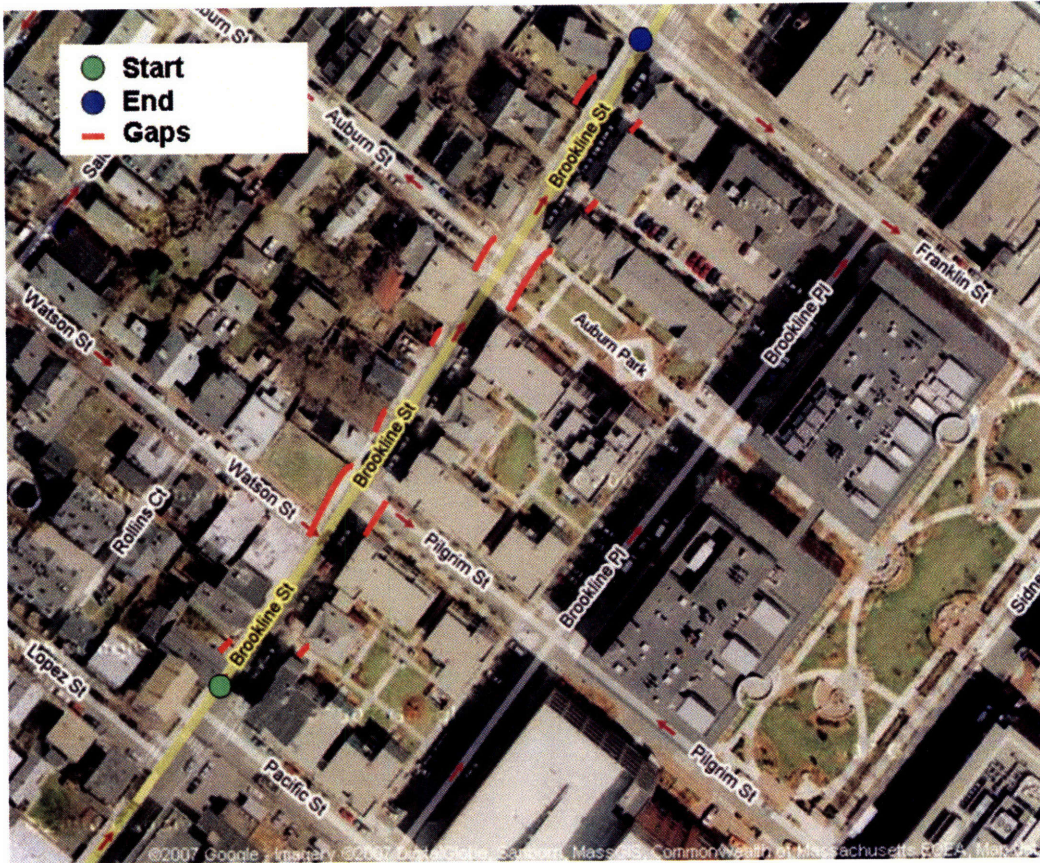
Figure 6-11: Gap Calculation: Example Street 1

the α estimates obtained from each street.

Indeed in Figures 6-13 and 6-14 we observe a linear relationship between the path loss coefficient α and each gap-based metric. Specifically we find linear estimators, $\hat{\alpha}_1$ and $\hat{\alpha}_2$, that predict α with rms errors of 0.47 and 0.27 respectfully,

$$\hat{\alpha}_1 = 5.3 \cdot P_1 + 1.5$$

$$\hat{\alpha}_2 = 3.2 \cdot P_2 + 1.5$$

If we estimate α utilizing both P_1 and P_2 the rms error is reduced to 0.22,

$$\hat{\alpha}_3 = 5.1 \cdot P_2 - 3.7 \cdot P_1 + 1.6$$

Here we note that the estimator based on P_2 tends to perform better. Specifically
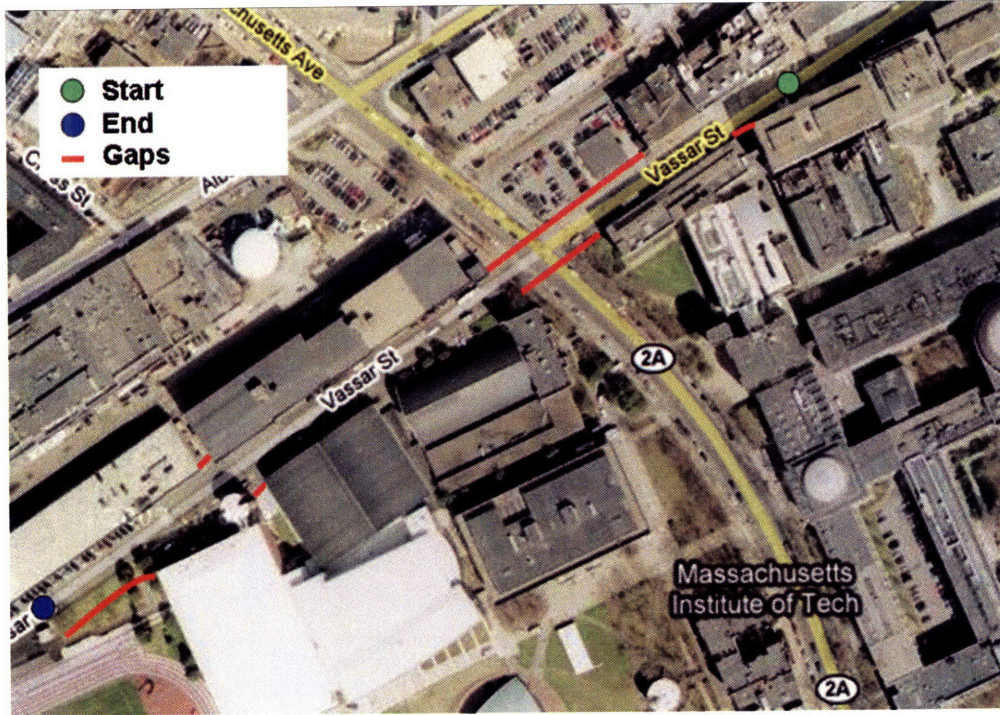
Figure 6-12: Gap Calculation: Example Street 2

this should be the case in streets where there is disproportionate number of gaps on a single side the street. In the extreme case where there are buildings lining only one side of the street and there are no gaps, the metric P_1 will be only 0.5 but the attenuation will be high. The metric P_1 does have utility, as seen in the reduced rms error of the joint estimator, given that in streets where gaps on each side of the street are independent P_2 may overestimate the gap effect. In an extreme case if each side contains a gap if and only if the other does not the metric P_2 will be 0 however 50 percent of the street will be lined with buildings.

6.4.1 Environmental Constant

A more complete model for power attenuation includes a constant factor C, often referred to as the environmental constant,

$$P_r = C(\frac{P_t}{r^\alpha})$$

137
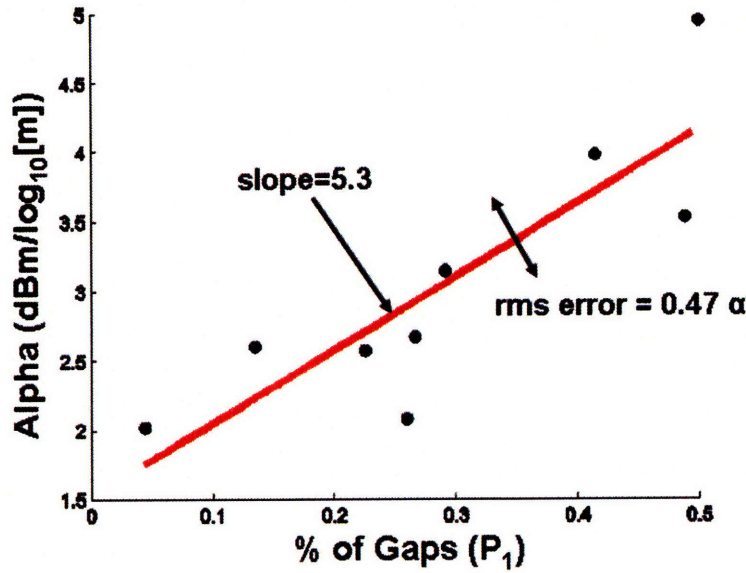
Figure 6-13: Relationship between Alpha and P1

where P_r refers to the average power received at a distance of r given a transmit power of P_t. This factor accounts for fixed power losses due to specific qualities pertaining to the environment. In practice its value can vary widely depending on the environment. In the context of our street propagation environments we can attribute this factor C to the fixed loss associated with propagating around a corner. We can approximate this factor as,

$$\hat{C} = P_t - \hat{\alpha_2} \; [dB]$$

where P_t is the field strength at 1 meter from the transmitter and $\hat{\alpha_2}$ is the regression intercept of power received on link-length (l),

$$\hat{P_r} = \hat{\alpha} \cdot 10 \log_{10}(l) + \hat{\alpha_2}$$

Utilizing the approximation of $P_t = 30$dBm for our system we found $\hat{C}$ to have mean 27dBm and standard deviation 19dBm. A better approximation takes into account the fact that the propagation before the corner is Line-Of-Sight (LOS) for these
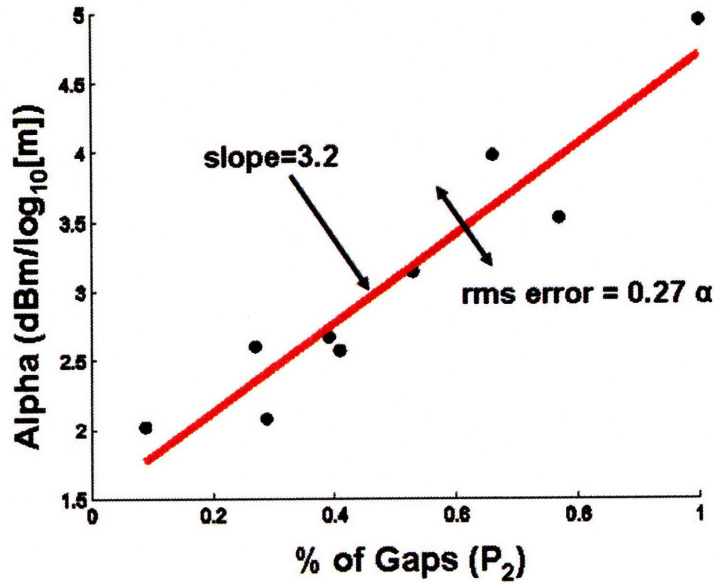
Figure 6-14: Relationship between Alpha and P2

measurements and corrects for this by estimating C as,

$$\hat{C} = P_t - \hat{\alpha_2} + (\hat{\alpha} - 2) \cdot L_c \ [dB]$$

where L_c is the distance (dB over 1 meter) between the transmitter and the furthest point down the street that still contains LOS with the transmitter. Here a correction is added that approximates the attenuation over this first portion of the link as having an alpha of 2. Using this new estimator for C we found a mean of 43 dBm and standard deviation of 5.6dBm. Here note that the corner losses are much more consistent with one another using this new estimator as any deviations due to individual α's and distance to corners (L_c) have been removed. It is also of note that two streets within this calculation had corner losses approximately 10dB higher than the average for the rest of the data set (removing them brings the mean to 40dBm and standard deviation to 2dBm). An interesting feature that stands out with these two streets is that they are the only streets in which the buildings near the corner are constructed primarily with wood (residential houses). In contrast the other streets had buildings made mostly of brick and concrete block. This suggests that a further study on corner

losses looking at features such as building material and building geometry may yield a multi-factor model that improves the prediction accuracy for corner loss.

6.4.2 Polarization

As a final remark we now briefly discuss some preliminary results from the polarization experiments we have conducted. In these experiments we returned to the street environments studied previously and again considered the NLOS around-the-corner channel. Three street locations were included and the channels between different polarization combinations at transmitter and receiver were measured. Both vertical and horizontal polarizations were observed, where the horizontal polarization was orthogonal to the street traversed by the receiver. At the transmitter both vertical and horizontal polarizations were measured, where the horizontal polarization was mounted such that energy was directed optimally for entering the street containing the receiver. The first observation of note is that each channel (h-to-h, v-to-v, h-to-v, v-to-h) had approximately the same power (within 5dB of each other) at a point along the street immediately after the corner. We can interpret this as meaning that the horizontal and vertical channels couple quickly while propagating around the corner. Additionally the stronger of the two channels (h-to-h vs. v-to-v) at this street point varied with each being approximately 5dB stronger in one street and about the same in the third. In addition the α's were calculated for each channel and were found to vary across polarization by as much as 1 over a single street. However, again the more strongly attenuated channel was found to change from street to street. In short, by adding more streets to the data set we may be able to build models utilizing environmental features to predict this behavior.

6.5 Path-Loss Model: Ground-To-Ground Propagation

Here we present a path-loss model for ground-to-ground communication over short link lengths (sub-kilometer) based on the measurements and propagation results presented in Sections 6.3 and 6.4.

Model Assumptions

1. **Stationary Regions:** The first assumption of the model is that the propagation environment over which the communication is taking place can be broken into stationary regions. We define a stationary region as a region of the environment in which signal power attenuates at approximately a constant rate with respect to distance, i.e. a constant α. Physically this refers to a region of the environment that is homogeneous with respect to those environmental characteristics that dominate power attenuation. This behavior was observed in street environments.

2. **Boundary Loss:** The second assumption of the model is that there is a fixed power loss incurred by moving from one stationary region to an adjacent stationary region that is dependent on the physical nature of the boundary.

3. **Dominate Paths:** The final assumption is that power received over short link lengths (sub-kilometer) is dominated by a small number (typically 1 or 2) of physical paths between transmitter and receiver, each of which may comprise of numerous multipath components (MPCs). The justification for which is that over short ground links the signal must traverse over only a small number of stationary regions in order to propagate from transmitter to receiver. Given this, any physical path that requires traversing an additional stationary region or boundary is quickly much weaker than those paths that traverse a minimal number of such features. Such behavior was observed in our street experiments. In these experiments physical propagation paths included traversing

141

several "corners", meaning that the signal had to propagate around several corners in order to reach the receiver. Each of which is considered as crossing a boundary between one stationary region to another. When comparing power received between links of the same length but with varying number of corners we consistently found that those links with the higher number of corners tens of dB weaker.

Link Attenuation Calculation: Street Model Example

We now illustrate how to calculate the power attenuation over an arbitrary communication link utilizing our model. In particular we will illustrate this point by taking the example of the street environment.

1. **Determine Dominant Physical Paths:** The first step in utilizing our model is to identify those physical paths in the environment that will dominate the power received at the receiver. Recalling our previous discussion, it will be common in short link lengths for the number of such paths to be limited to one or two. In particular for street environments we found these to be the paths between transmitter and receiver that require maneuvering the smallest number of corners. Figure 6-15 displays an example of a communication link in a representative street environment. Here the transmitter and receiver are separated by approximately five blocks which for sub-kilometer links is at the upper-end with respect to block separation. Here we see that a single one-corner physical path dominates the communication link given that all alternative paths require the propagation around at least two additional corners. This single physical path though is in general composed of many individual MPCs created by the scattering environment.

2. **Stationary Region Partitioning:** The second step is to break the dominant physical propagation paths into stationary regions. Recall that in general a stationary region is defined as a region a long the propagation path in which the path-loss is relatively constant. In the case of a street environment we

142
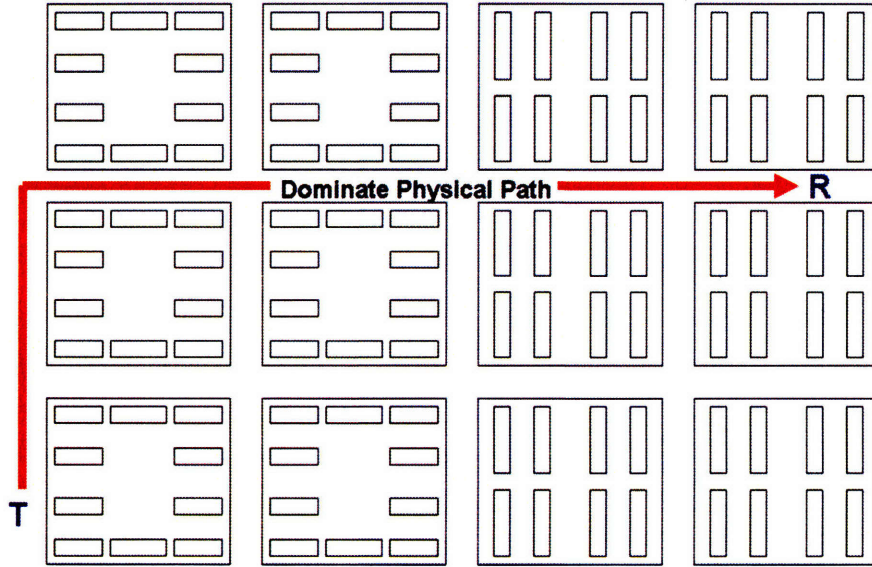
Figure 6-15: Identifying the dominant physical paths

observed that the streets themselves are good candidates for stationary regions. Returning to our example street scenario in Figure 6-16 we see that the dominate physical path can be broken into three distinct stationary sections. Here we see that individual streets correspond to distinct stationary regions as supported by our empirical results. Additionally in this case we illustrate how a single street may be broken into several stationary sections as the propagation environment, here building density, varies along the street.

3. **Stability region path-loss estimation** The third step is to estimate the path-loss coefficient, α, associated with each stability region. Recalling our measurement analysis in Section 6.4 we found that simple physical models can be used to predict α with good accuracy. In particular for street environments we found that a single environmental parameter, building density along the street, can be used to carry out this estimation. Specifically this came in the form of a linear predictor mapping building density to path-loss. Specifically,

$$\hat{\alpha}_3 = 5.1 \cdot P_2 - 3.7 \cdot P_1 + 1.6$$

where P_1 and P_2 are gap-based metrics defined in Section 6.4.
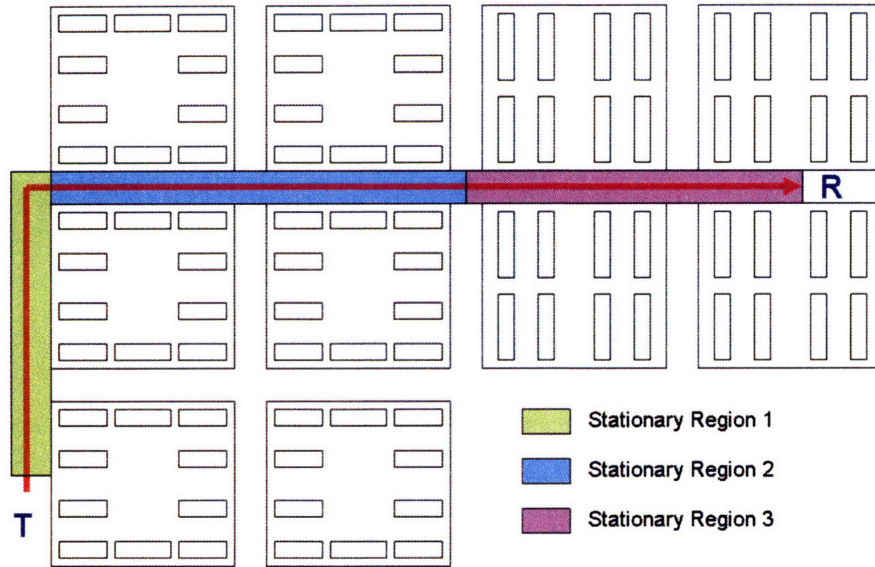
Figure 6-16: Partitioning dominate paths into stationary regions

4. **Boundary loss calculation:** The fourth step is to estimate the losses accrued from propagation across stationary region boundaries. The most promising strategy for accomplishing this is to categorize the boundaries according to their physical structure. Returning to the example of the street environment we can classify such boundaries as being either corners or street transitions where the latter refers to a point a long the street where the building density changes. In Figure 6-16 we see that the boundary between regions 1 and 2 falls in the corner category whereas the boundary between regions 2 and 3 is a street transition. For a street transition we can reasonably assume that no additional power loss is incurred as the propagation mechanisms remain the same. In the case of corner boundaries we can use several different methods to estimate the power loss. We can deterministically estimate the loss by geometric/ray tracing methods or actually take measurements to find the average loss incurred per corner. As stated in Section 6.4.1 we observed an average loss of approximately 43dB with standard deviation 5.3dB.

5. **Calculating Aggregate Loss:** Finally we can calculate the power received P_r (average), at the opposite link end as the superposition of average power

144

obtained from the dominant physical propagation paths,

$$P_r = \sum_{i=1}^{K} P_i$$

where P_i is the average power received from the ith of K dominant physical propagation paths. Note that this relationship is additive given the linearity of the mean operator and the fact that we are considering here the average power received. The average received power due to each propagation path then can be calculated as,

$$\log(P_i) = \log(P_t) - (\sum_{j=1}^{R} \log(d_j^{\alpha_j})) - (\sum_{j=1}^{R-1} b_{j,j+1})$$

The first term in this formulation, P_t, refers to the power at the transmitter. The second term is a summation of the power attenuation over the R stationary regions of the propagation path. The power attenuation due to j^{th} region is approximated as the propagation distance across that region, d_j, taken to the α_j power. Here α_j is the path-loss coefficient corresponding to the jth stationary region of the propagation path. The final term represents the summation over the fixed power losses due to crossing the R-1 boundaries between adjacent stationary regions. Here $b_{j,j+1}$ represents the power loss (dBm) incurred from crossing the boundary between the jth and $j + 1^{st}$ stationary region. Again these boundary losses can vary from 0 to tens of dB depending of the physics of the boundary, as illustrated in the previous example.

6.5.1 Performance

We now consider the performance of this model as compared to traditional empirical models within the framework of street environments. To do this we have developed a simulation that utilizes a set of assumptions that is consistent with our measurements. Specifically we assume the following distributions for the path-loss coefficient (α) and

corner loss (b)[1],

$$\alpha \sim U(2,5)$$

$$b \sim N(43,5.6) \text{ [dBm]}$$

In addition we assume the distribution of our α estimator to be,

$$\hat{\alpha} = \alpha + N(0,0.22)$$

For a single-corner link of length d (dB over 1 meter) we then estimate the path-loss (PL) as,

$$\bar{PL}_{model} = \hat{\alpha} \cdot d + \hat{b} \text{ [dBm]}$$

where,

$$\hat{b} = E[b] = 43$$

As discussed in Section 6.1, empirical path-loss models come in the form of linear predictors that have been trained on various macro environment types, e.g. rural vs. suburban vs urban. For the street environment considered here, the empirical model would utilize a single α that had been derived for its corresponding macro environment type. We then consider comparing our model to the optimal linear predictor,

$$\bar{PL}_{empirical} = \alpha^* \cdot d + b^*$$

where for this simulation $(\alpha^*, b^*) = (3.5, 43)$. Figure 6-17 displays thee results of this simulation. Here we see a 10dB advantage (rms error) in predicting path-loss for our model when compared to the optimal linear estimator over link lengths as short as 100 meters.

---

[1]U(a,b): Uniformly distributed on [a,b]

Path-Loss Estimation Performance

α ~ U[2,5]

Optimal Linear Estimator
Model

≈ 10dB Performance Advantage 100m links

rms error (dBm) vs Link Length (dB over 1 meter)
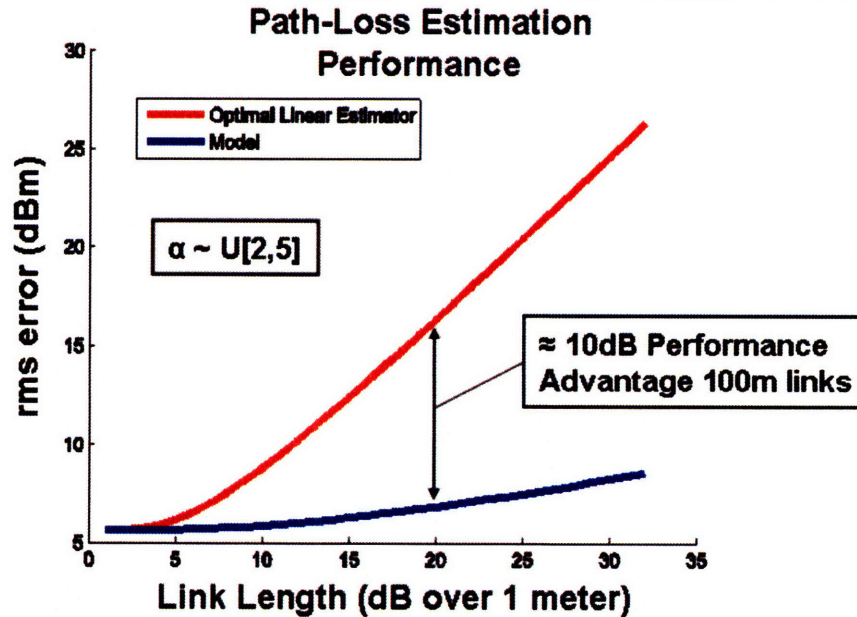
Figure 6-17: Performance Comparison between Path-Loss model and optimal linear (empirical) model

6.6 Air-To-Ground Links

An Air-To-Ground link is defined as a communication link in which one link end is situated at a much higher elevation than the other, with links being both Line-Of-Sight (LOS) and NLOS. This typically comes in the form of one link end at ground level and the other mounted to a tower that rises well above the other objects in the environment. This type of system topology can be found in cell phone and other base station centered networks where mobility is necessary for at most one link end. Here we study separately this class of links, as the physical propagation is quite different than that of ground-to-ground links. Specifically the scattering environment local to the ground node tends to dominate the channel as opposed to the entire scattering environment between transmitter and receiver in the ground-to-ground case.

6.6.1 Measurement Campaign

In order to better understand the realized behavior of such propagation environments we carried out the following measurement campaign.

147

1. **Transmitter**

   (a) **Antenna Element:** One 8dBi dipole

   (b) **Antenna Polarization:** Vertical

Figure 6-18: View from atop Green Building.

   (c) **Mounting:** The transmitter system was mounted on the roof of the Green Building at MIT campus. The Green Building is the tallest building in Cambridge, with a height of approximately 300 feet. See Figures 6-18 and 6-19.

2. **Receiver**

   (a) **Antenna Elements:** Eight 8dBi dipoles

   (b) **Antenna Polarizations:** Vertical

   (c) **Antenna Array:** Each element spaced by more than several wavelengths so as to obtain independent channel measurements.

   (d) **Mounting:** System installed in van with receiver mounted to the roof of the van.

Figure 6-19: Transmitter electronics housing on top of Green Building

3. **Measurement Setup:** The van housing the receiver was driven over a large portion of Cambridge with snapshots taken over a diverse set of physical locations. See Figure 6-20.

4. **Environments:** Cambridge, MA

6.6.2 Experiments and Analysis

Here again we want to study the relationship between link length and power attenuation. In order to do this we carried out the measurement campaign described in Section 6.6.1 which resulted in the collection of a large and diverse set of air-to-ground channel measurements. Figure 6-20 displays an overhead view of the measured links where the fixed transmitter location atop the Green building is marked by a red T. Each marker corresponds to a single receiver position over which the channel between transmitter and receiver was measured across eight independent receiver channels. Here we can see the diversity of physical scenarios measured as many different neighborhoods were included in the data set. Given this collection of channel data we investigated the link-length, power attenuation relationship. Figure 6-21 displays a
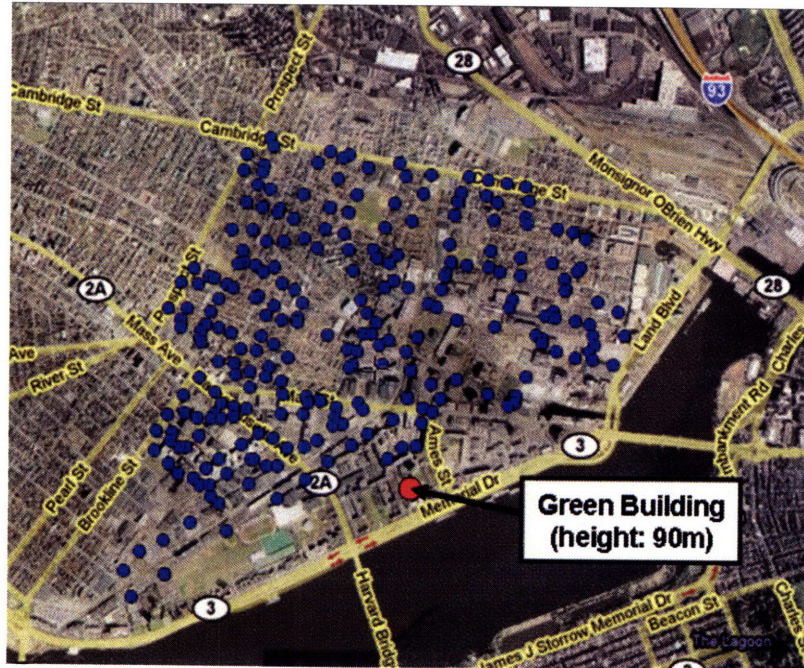
Figure 6-20: The Green Building measurements: Each measurement location is marked by a blue marker.

scatter plot of link-length in dB (relative to 1 meter) versus power received (dBm) for each channel measurement from the data set. Here we observe that the power received tends to decrease for longer link lengths. In order to measure this relationship we have performed a linear regression representing the best linear relationship between the two parameters. The resulting best fit line is displayed in Figure 6-21 in red and was found to have a slope of 1.9 which means that power received decreases approximately proportional to the link length squared on average. By inspection we can see that there are non-trivial deviations from this best-fit line suggesting that there exist additional factors beyond link length that play an important role in determining path-loss for these link types. Specifically we found the standard deviation from the best-fit line to be 8.3 dBm which is significant with respect to link capacity. This phenomenon is additionally observable from the GPS image in Figure 6-20. Here each receiver position is color-coded according to the average power received across each receive channel. By inspection we see that the power attenuation is directionally biased giving rise to these deviations from the mean.
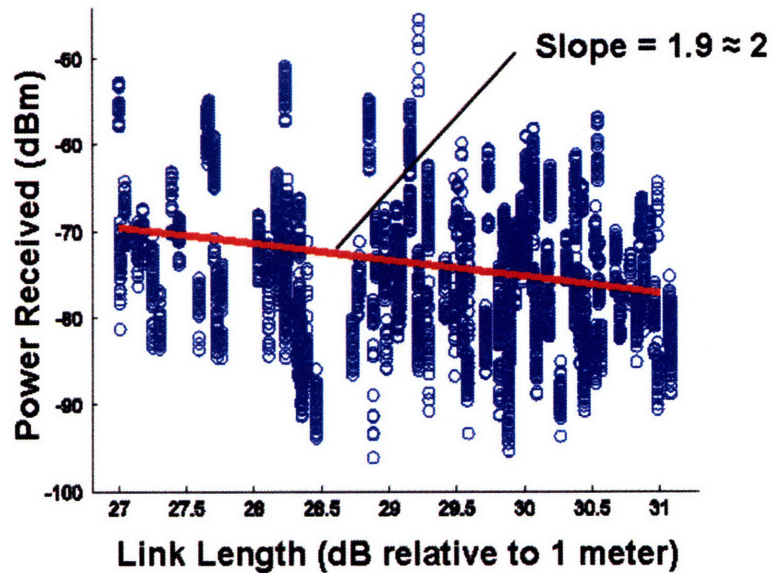
Figure 6-21: Air-To-Ground links: Relationship between link length and power received

6.6.3 Path-Loss Model: Air-To-Ground Propagation

We now consider the physics of air-to-ground links, its relationship to our empirical results, and show how this forms the basis for a path-loss model for air-to-ground communications. For an air-to-ground system we claim that a particular propagation path between transmitter and receiver can be generally broken into two segments. As illustrated in Figure 6-22, the physical propagation path for air-to-ground links is divided into two sections corresponding to the segments above and below the scattering line of the environment. The scattering line is defined as the height of the scatterers local to the ground end of the link. In our measurement environment this was dominated by local building heights and a few trees. The first segment of the propagation path is not obstructed by scatterers and involves Line-Of-Sight (LOS) propagation. The propagation path then enters the second segment as it crosses the scattering line local to the receiver. Here scatters form a potentially rich multipath environment for the final leg of the propagation. Note that local scatters will with high probability dominate the channel as most energy will generally be reflected back up towards

151
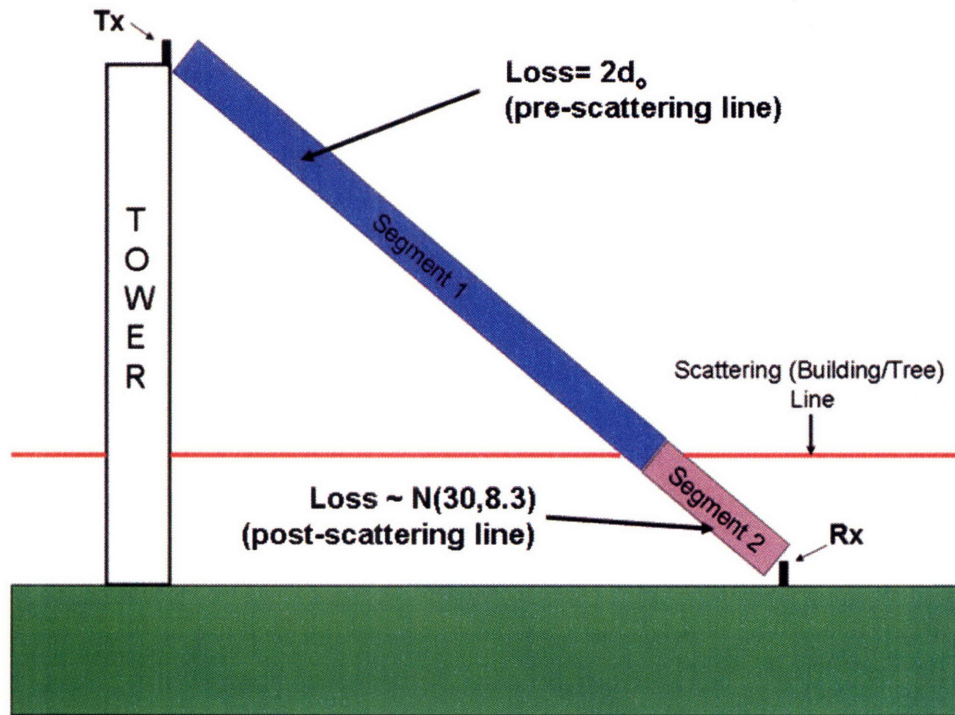
Figure 6-22: Air-To-Ground Links: Two segment model

the sky. Any residual energy scattered parallel to the ground will experience high attenuation, as observed in the ground-to-ground analysis.

We now compare our experimental results with this physical model of air-to-ground propagation. Recall our experimental result that power attenuation was on average proportional to the link length squared. In addition we found that in practice a particular channel can deviate from this relationship by a nontrivial amount, tens of dBm. Now consider the tower propagation model introduced above. The first segment of the propagation path (LOS) will in general dominate the length of the link. This is due to the dominance of the local scattering environment on the channel. With this in mind we can break the attenuation of a particular signal path into two categories corresponding to the two path segments. The first path segment is not obstructed by scatterers so that its attenuation can be predicted accurately using the LOS alpha-distance attenuation model, where for LOS alpha can be approximated as 2. With the length of the second path segment being small relative to the first, the attenuation due to propagation along the second segment will be dominated by its

scattering environment. Formally we can express the relationship between the power received P_r, and transmitted power P_t as,

$$\log(P_r) = \log(P_t) - 2 \cdot \log d - N$$

where d is the propagation length of the first segment and N is the attenuation due to scatterers in the second segment. In this formulation N is the only nondeterministic parameter. We can rewrite this formulation to obtain,

$$\log(P_r) = \log(P_t) - E[N] - 2 \cdot \log(d) - (N - E[N])$$

$$= C - 2 \cdot \log(d) - \tilde{N}$$

where the parameter $\tilde{N}$ is zero-mean and is referred to as the excess loss. In Figure 6-21 the excess loss of a particular channel can be observed as the deviation from the regression line of best fit. By inspection we can see that the excess loss $\tilde{N}$ is uncorrelated with the link length d. Our experimental observations then agree with this model formulation as the calculated regression slope of 1.9 closely matches the slope of 2 predicted by the model.

6.6.4 Excess Loss Model

We now analyze the behavior of the excess loss parameter of the air-to-ground attenuation model experimentally validated above. Figure 6-23 displays a histogram of the excess loss parameter taken from our tower data set. Recall that the excess loss is calculated for each data point according to its deviation from the best fit regression line. Here we observe a gaussian like distribution for this parameter. Physically excess loss within the context of our tower model is derived from the scattering mechanisms along the second section of the propagation path. One can consider the excess attenuation of a particular signal path then as being due to multiple independent interactions with various objects along the path. The central limit theorem then predicts a gaussian distribution for the log of the power attenuation which is supported by our empirical
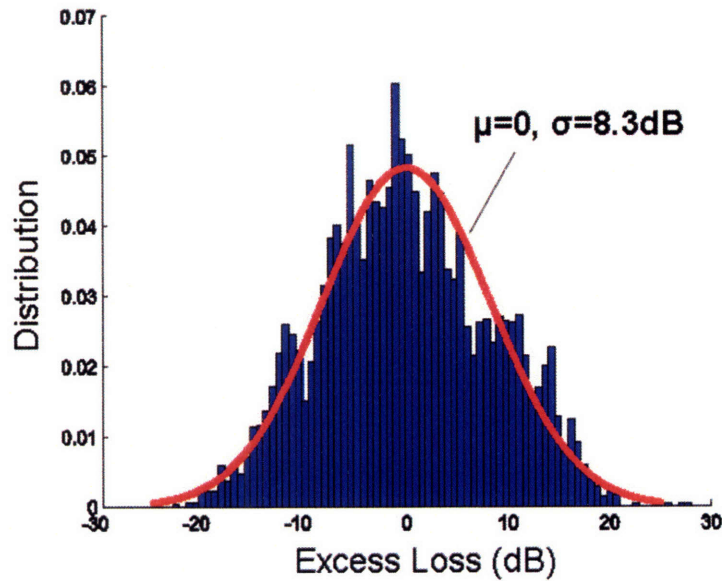
Figure 6-23: Excess Loss of Air-to-Ground Links

result. Given this match of theory and observation, the use of a gaussian distribution for the excess loss parameter, $\tilde{N}$, of our tower attenuation model is well supported. The last component to fully describing this model then is choosing a proper value for the variance of this gaussian distribution. In our measurements we found the standard deviation of the excess loss to be 8.3 dB which serves as a good value for urban and residential environments. However one would expect this value to be much smaller in less densely populated areas where trees and LOS propagation are relatively more dominant.

Lastly we mention the log-normal fading model [8], which is a description for the shadowing characteristics of wireless communication. Here the same physical arguments as utilized above are argued to predict a log-normal distribution for the power received in such a communication regime. In a ground-to-ground regime the dominant propagation paths are typically influenced by more scattering objects over longer path lengths so that one would expect the fading characteristics to converge more quickly to a gaussian distribution. However our observation in air-to-ground regimes, where fewer local objects are dominant, that fading behavior converges to a

gaussian-like distribution helps validate the log-normal shadowing model.

Chapter 7

Frequency/Multipath Characteristics

7.1 Background

Understanding the small-scale fading behavior of the wireless channel is an important component to system design. In particular in Orthogonal Frequency Division Multiplexing (OFDM) systems it is a direct indicator of the appropriate bandwidth allocation for each sub-channel. In the context of MIMO it determines the spatial coding rate in the frequency domain and is an indicator of the computational complexity of such systems. Having good models then for this channel behavior is again crucial for optimal signal and system design.

Modeling of channel multipath structure typically comes in one of two forms, namely: stochastic or deterministic. Similar to path-loss, multipath deterministic modeling is carried out by utilizing ray-tracing techniques [30], [32] where a large amount of information about the propagation environment is required. In the stochastic domain however, small-scale fading is most often modeled as either Rayleigh or Rician [8], [6]. Here it is assumed that the magnitude of the channel over a narrow bandwidth, having been normalized for large-scale fading/shadowing, has a Rayleigh or Rician distribution. More specifically it is assumed to be Rayleigh for Non-Line-Of-Sight (NLOS) links and Rician in the LOS case. Even with the ubiquity of these

models there is relatively little empirical work that validates their use. Both [10] and [11] each reported NLOS channel data as approximately fitting the Rayleigh distribution in their indoor experiments. However we are not aware of any work that has taken a comprehensive look at the accuracy of the Rayleigh fading model in outdoor environments.
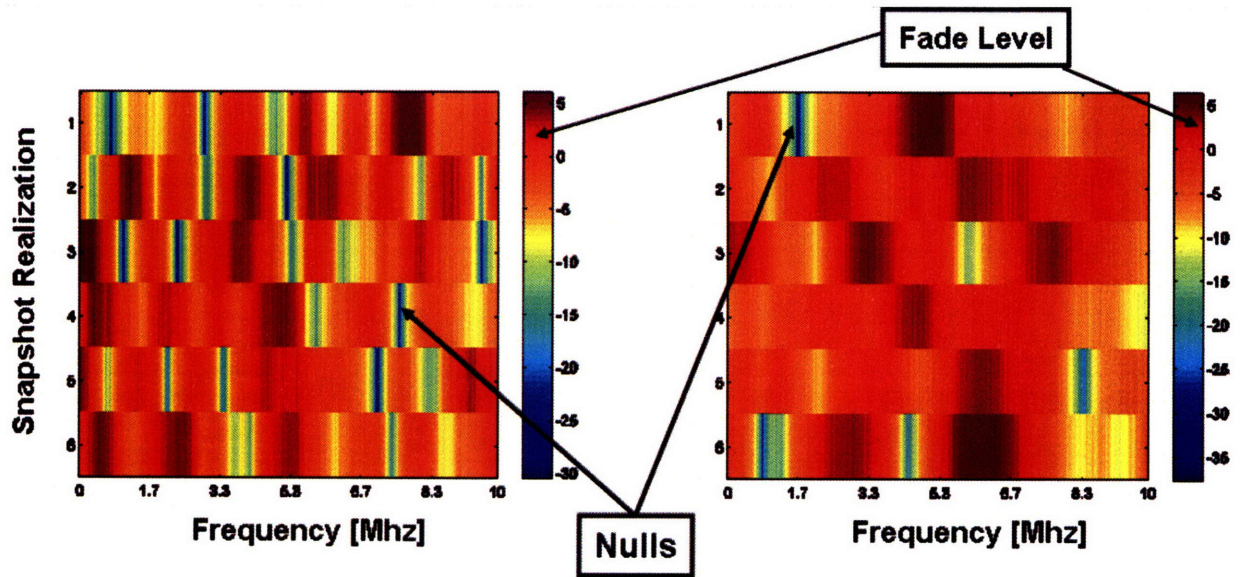
Figure 7-1: Fade Distribution and Fade Width

In addition to the fading distribution induced by multipath environments the coherence bandwidth and equivalently delay-spread of the channel quantifies the level of multipath in the channel. Having a model that predicts these parameters based on a partial environmental/link description, as opposed to the full description required by ray tracing techniques, would allow us to efficiently predict the channel multipath. References [12] and [13] reported some linear correlation between link-length and these channel parameters for indoor environments. Here we test for correlation between multipath and link-length in both outdoor link regimes. Additionally we test for any other environmental parameters that maybe be used in predicting the multipath behavior of the channel.

7.2 Small-Scale Fading Distribution

In this section we explore experimentally the fading distribution induced by multipath environments. Here we specifically concentrate on fading in the frequency domain. The most common model for predicting this behavior is the Rayleigh fading model. In this model it is assumed that the instantaneous narrowband channel, h, has a zero-mean circular symmetric complex gaussian distribution,

$$h \sim \mathcal{CN}(0, \sigma^2)$$

Physically this model is derived from the notion that in rich multipath environments the channel, h, is comprised of the superposition of many independent propagation paths. The gaussian distribution then follows from the central limit theorem. Consequently the channel amplitude and phase are modeled as having Rayleigh and uniform distributions respectfully,

$$|h| \sim \frac{|h|}{\sigma^2} \exp \frac{|h|^2}{2\sigma^2}, |h| > 0$$

$$\angle h \sim \frac{1}{2\pi}, 0 \leq \angle h \leq 2\pi$$

In the case of a single dominant multipath component (MPC) the channel is more accurately modeled as having non-zero mean,

$$h \sim \mathcal{CN}(h_o, \sigma^2)$$

where $h_o \epsilon \mathcal{C}$ denotes the channel response of the dominant MPC. In this case the channel fading takes on a Rician distribution. The Rayleigh distribution is then a special case of the Rician for $h_o = 0$.

Here we compare the empirical fading distributions of our channel data over a variety of environments to the Rayleigh and Rician models. To do this we utilize the data sets collected in Section 6 from both link operating regimes. The first set of environments were in the ground-to-ground regime and included typical urban/suburban

environments such as city streets, parking lots, alleys, and residential neighborhoods. Each of the snapshots included only NLOS channel conditions matching the assumptions of the Rayleigh model.

In order to test the performance of these fading models each snapshot had to be normalized in such a way as to remove the affect of large-scale fading, i.e. path-loss due to link-length and shadowing. In order to do this each set of snapshots (across receiver channel and frequency) corresponding to a single transmitter/receiver location were individually normalized removing any large-scale affects,

$$\hat{h}_{r,t,f,n} = \frac{h_{r,t,f,n}}{\bar{h}_r}$$

$$\bar{h}_r = \sum_{t=1}^{T} \sum_{f=1}^{F} \sum_{n=1}^{N} \frac{|h_{r,t,f,n}|^2}{T \cdot F \cdot N}$$

where each channel snapshot realization $h_{r,t,f,n}$ has been normalized by the average power across T ($\approx$ 10) snapshots, F (300) frequencies, and N (8) receive antennas. For each data set we measure the performance of both fading models as the difference between observed and predicted fading distributions,

$$\text{Error (E)} = \int_0^\infty |f_e(x) - f_r(x, \hat{K})|^2 \cdot f_e(x) \cdot dx$$

where $f_e(x)$ and $f_r(x, K)$ denote the empirical and rician (K=0 for rayleigh) distributions respectfully. The rician distribution however is a function of the ratio between the fixed and random component (K-factor, see Section 8.3), making it necessary to estimate this parameter when carrying out distribution analysis. To estimate the K-factor implied by the data we utilize a standard moment-based estimator [36],

$$\hat{K} = \frac{-2\mu_2^2 + \mu_4 - \mu_2 \cdot \sqrt{2\mu_2^2 - \mu_4}}{\mu_2^2 - \mu_4}$$

$$\mu_2 = \sum_{r=1}^{R} \sum_{t=1}^{T} \frac{|\hat{h}_{r,t}|^2}{R \cdot T}$$

$$\mu_4 = \sum_{r=1}^{R} \sum_{t=1}^{T} \frac{|\hat{h}_{r,t}|^4}{R \cdot T}$$

Table 7.1 displays the results of this analysis applied to nine different environments. Similarly Table 7.2 contains the results applied to the aggregate set of ground-to-ground data stratified into 4 sets of link lengths. Additionally the empirical fading distributions of 6 examples from this set of data are displayed figures 7-2, 7-3, and, 7-4 along with their Rayleigh and Rician counterparts.

Table 7.1: Rayleigh and Rician Fading Model Performance: By Environment

No.	Environment Type	$\hat{K}$	$10\log_{10}(E_{rician})$	$10\log_{10}(E_{rayleigh})$
1	Alley	0.3	-31	-28
2	Campus Street	0.3	-33	-31
3	Alley	0.7	-33	-24
4	Campus Street	0.6	-39	-29
5	Air-to-Ground	1.0	-30	-20
6	Parking Lot	0.1	-35	-35
7	Residential	0.2	-33	-34
8	Residential	0.1	-32	-31
9	Residential	0.5	-33	-28

Table 7.2: Rayleigh and Rician Fading Model Performance: By Link Length

Link Length	$\hat{K}$	$10\log_{10}(E_{rician})$	$10\log_{10}(E_{rayleigh})$
50-100m	0.5	-33	-31
100-200m	0.2	-36	-38
200-400m	0.1	-34	-34
400m	0.1	-37	-36

By inspection of these tables and figures we see that the Rayleigh and Rician distributions are quite accurate in modeling the realized small-scale fading behavior of the channel. While the Rician distribution is in general slightly more accurate than the Rayleigh, the difference is not large enough to warrant the added complexity of the Rician model. Specifically the estimated K-factors (see tables) are all small ($<$ 1) which suggests that the Rayleigh fading model is a good model for outdoor NLOS channels and link lengths as short as tens of meters. The data set that diverges most
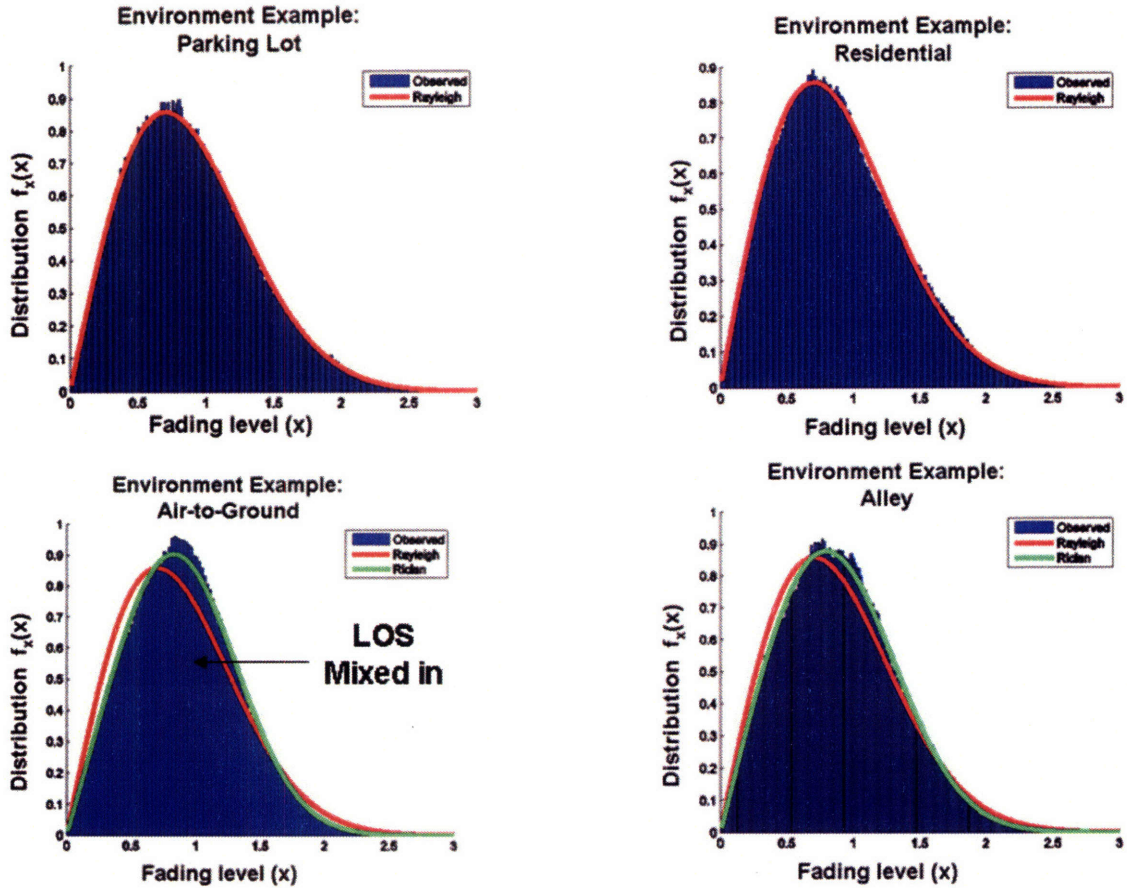
Figure 7-2: Small-Scale fading distribution across four example environments.

from this fading model is the set comprised of air-to-ground links. The K-factor of this set (K=1), while still fairly small, is most likely due to the presence of Line-Of-Sight links mixed into this data set.

7.3 Predicting Multipath Structure

Recalling the path-loss experiments of Chapter 6, we were able to justify experimentally simple environmental models as tools for accurately predicting α utilizing only a few environmental parameters. That said, it would also be beneficial to be able to do the same for the multipath structure of the channel. Specifically we would like to reduce the complexity of this structure into a model that captures the important features, e.g. fade duration and coherence bandwidth, yet depends on a
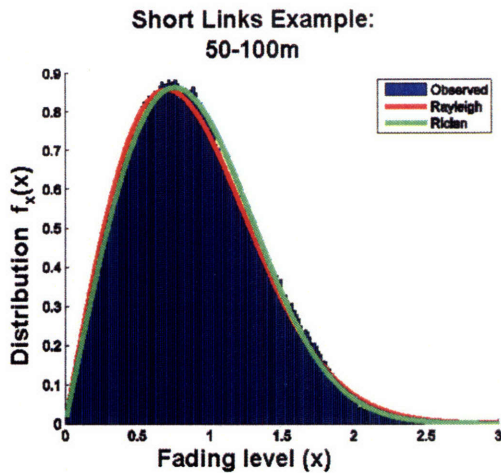
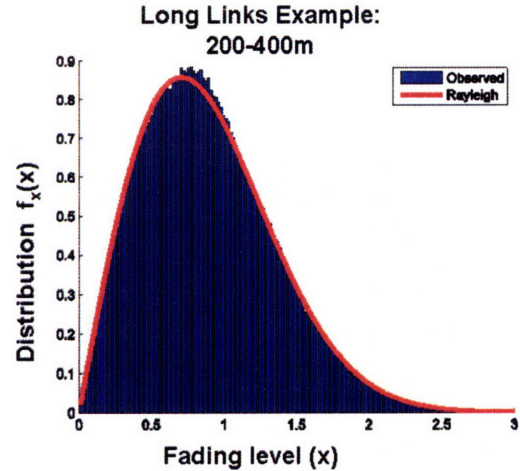Figure 7-3: Small-scale fading distribution: Short links

Figure 7-4: Small-scale fading distribution: Long links

small number of parameters that are easily measured. Figure 7-5 displays a scatter plot of 5dB coherence bandwidth (averaged across each snapshot) versus link length. Here we observe that as link-length increases, the coherence bandwidth correspondingly decreases on average. Figure 7-6 displays the same calculations taken over the air-to-ground channel data. In 7-6 we see no such systematic relationship between link-length and multipath structure. This suggests that there are additional environmental factors that drive this behavior. These observations support the theory that systematic relationships exist between multipath structure and the environment and motivate the model which we now introduce.

7.4 Multipath Model: Description

Here we introduce a model for multipath structure and derive a distribution for the delay-spread (and equivalently coherence bandwidth) of the channel. Recall that in a rich scattering environment a superposition of multipath components (MPCs) arrive at the receiver forming a channel response. The delay-spread of the channel is then defined (as a function of a threshold C) as the difference in propagation path lengths between the first MPC to arrive and the last with power of at least $(1/C)$ times the
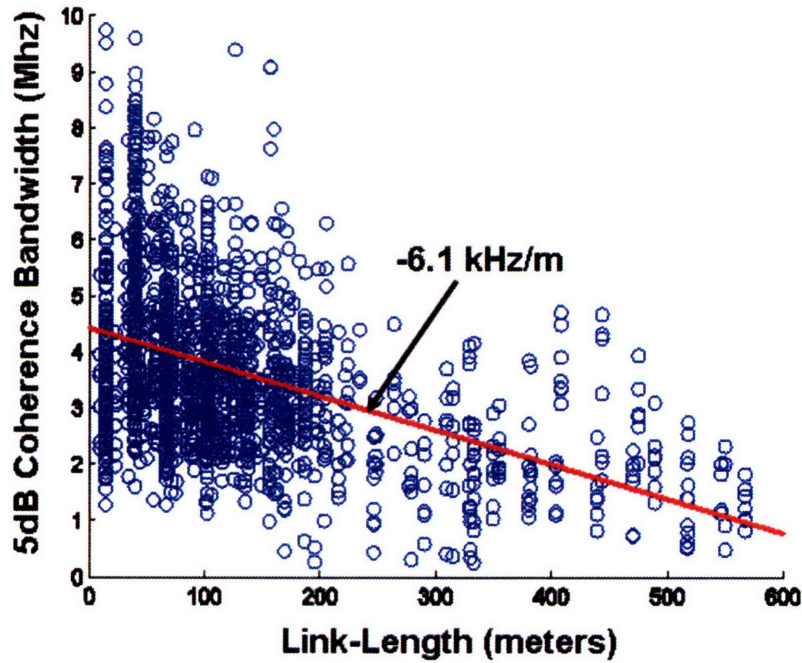
Figure 7-5: Coherence Bandwidth vs. Link Length: Ground-to-Ground Links

power of the first. Formally let us define the following arrival process,

$$X(x) = \begin{cases} 1 & \text{if } \exists \text{ a MPC with propagation length } d_o + \text{x, s.t. } |h_x|^2 \geq \frac{1}{C}|h_o|^2, x > 0 \\ 0 & \text{else} \end{cases}$$

where $|h_x|^2$ is the squared amplitude of the MPC that arrives with propagation path length $d_o + $ x meters, if it exists, and d_o is the propagation path-length of the first MPC to arrive. An arrival of the process X(x) then corresponds to the arrival of a multipath component that is strong enough to be considered in the delay-spread calculation. If we assume that the arrivals of MPCs at non-overlapping intervals of time can be reasonably modeled as independent, we can model X(x) as a poisson process. Now consider the rate of this process, λ. For every MPC that arrives at the receiver it is only considered an arrival of X(x) if it meets the power threshold. This leads to:
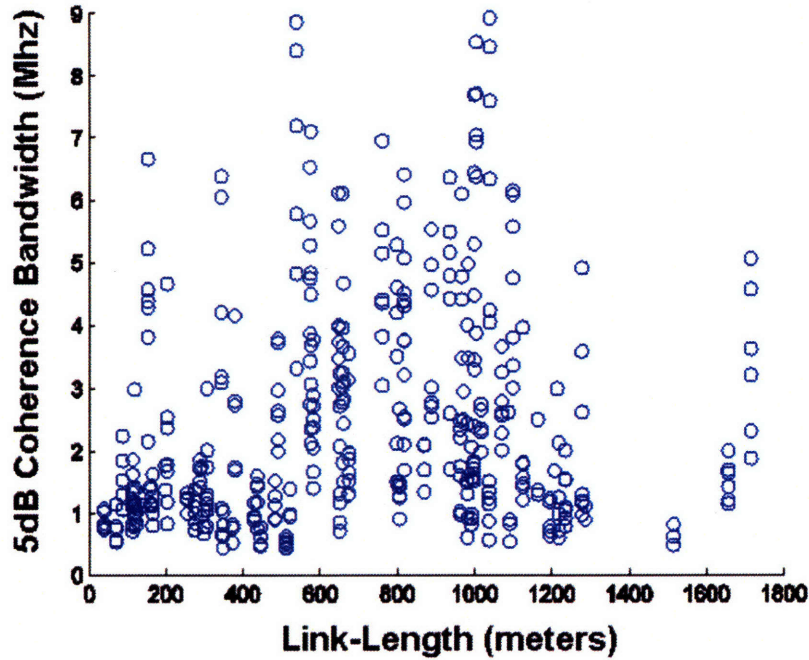
$$\lambda = q \cdot P_C$$

164

Figure 7-6: Coherence Bandwidth vs. Link Length: Air-to-Ground Links

where q (MPCs/m) is the arrival rate of MPCs and P_C denotes the probability of a MPC meeting the power threshold. To complete the distribution of X(x) we find P_C by:

$$P_C = P_C(x) = \text{Prob}(\frac{|h_o|^2}{|h_x|^2} \leq C)$$

$$= \text{Prob}(\frac{P \cdot (d_o)^{-\alpha} \cdot Y_1}{P \cdot (d_o)^{-\alpha} \cdot (\frac{d_o+x}{d_o})^{-\beta} \cdot Y_2} \leq C)$$

where P is the transmit power, α is the path-loss coefficient of the environment, β is the decay rate of the MPCs as a function of propagation length relative to the link-length, and Y_1, Y_2 are two independent exponentially distributed random variables with rate 1. Here β is a measure of the power penalty paid by MPCs for having propagation lengths longer than the link-length. In general we would expect β to be larger than α given that MPCs with longer delays tend to interact more with scatterers along the propagation path. The exponential distribution follows from the

165

assumption that the amplitude of MPCs is Rayleigh distributed. It follows that:

$$P_C(x) = P(\frac{Y_1}{Y_2} \leq C \cdot (\frac{d_o}{d_o + x})^\beta)$$

$$= \frac{C \cdot (\frac{d_o}{d_o + x})^\beta}{C \cdot (\frac{d_o}{d_o + x})^\beta + 1}$$

where the last expression follows from the exponential distribution of Y_1 and Y_2. Given this expression for $P_C(x)$ we arrive at:

$$\lambda(x) = \frac{C \cdot (\frac{d_o}{d_o + x})^\beta}{C \cdot (\frac{d_o}{d_o + x})^\beta + 1} \cdot q \; [\frac{\text{MPCs}}{m}]$$

as the arrival rate of the non-homogeneous poisson process X(x). The CDF of the delay spread τ_{DS} then follows as:

$$P(\tau_{DS} \leq x) = P(\text{X(x) has no arrivals after } d_o + x)$$

$$= P(N(x) = 0)$$

where N(x) is the number of arrivals of X(x) after x meters. With X(x) distributed as a poisson process, N(x) is poisson distributed with,

$$\lambda_N(x) = \int_x^\infty \lambda(x) \cdot dx$$

so that,

$$P(\tau_{DS} \leq x) = \exp^{-\lambda_N(x)}$$

giving the following distribution for the delay-spread:

$$f_{\tau_{DS}}(x) = -a'(x) \cdot \exp^{-a(x)}$$

$$= \lambda(x) \cdot \exp^{-\int_x^\infty \lambda(x) \cdot dx}$$

Given that $\lambda(x)$ is a function of C, β, q, d_o, and x, the distribution for τ_{DS} is best solved numerically for general values of β. In the case of $\beta = 2$, an analytical expression exists for the distribution as,

$$f_{\tau_{DS}}(x) = \frac{C \cdot d_o^2 \cdot q}{C \cdot d_o^2 + (d_o + x)^2} \cdot \exp^{\sqrt{C} \cdot d_o \cdot q \cdot (\arctan \frac{d_o + x}{\sqrt{C} \cdot d_o} - \frac{\pi}{2})}$$

The above expression was derived by utilizing the Mathematica software package to solve the integral of Equation 7.4. However as we will see in the next section β is typically much larger than 2. Additionally we note that the distribution is insensitive to q when the arrival-rate is dense, e.g. for changes in q when q is on the order of $1 \frac{MPC}{m}$ or larger. If this is the case, which we have observed empirically in ground-to-ground data, then the complexity of the model reduces to the single parameter β.

7.5 Multipath Model: Performance

Given this multipath model we now test its performance by comparing it to our channel data. Recall that our model is parameterized by link-length (d_o), MPC arrival-rate (q), and decay-rate (β). Given that the link-lengths are known, we test performance by finding values of q and β that provide the best match between model and data, quantify any differences between the two over several multipath metrics, and then validate that these parameter values are physically plausible.

The first metric that we consider is that of Fade Width (FW), which is a measure of the bandwidth of fades. Specifically we define FW at a frequency x, such that Fade(x) ϵ [L,U], as:

$$FW(x) = x_{max} - x_{min}$$

$$x_{max} = \min_{y \geq 0 | \text{Fade}(x+y) \, = \, U} y$$

$$x_{min} = \max_{y \leq 0 | \text{Fade}(x+y) \, = \, L} y$$

where the fading level, Fade(x) [dB] (see Section 7.2), is the power received at fre-

quency x relative to the mean attenuation for that link and [L,U] is the interval over which the fade is defined. Specifically we consider three fading intervals: Unfaded [-5dB, ∞], Faded [-15dB, -5dB], and Deeply-Faded [$-\infty$, -15dB].

As a first measure of model performance we have stratified our ground-to-ground data set into overlapping subsets according to link-length,

$$s_i \epsilon S_L \Leftrightarrow l_i \epsilon [L - 20, L + 20], \quad \text{L=50,70,90,....,650}$$

where snapshot i (s_i) belongs to subset S_L if its link-length (l_i) is within 20 meters of L. For each subset S_L we then calculate the average FW according to,

$$\bar{FW}_L = \frac{1}{|S_L| \cdot B} \sum_{i:s_i \epsilon S_L} \sum_{j=1}^{B} FW(s_i(j)) \tag{7.1}$$

by averaging over the fading widths at each frequency (B=300) of each snapshot in S_L. Similarly a set of channel snapshots ($\tilde{S}_L$) was generated according to the model (see Section 7.4) over a variety of values for the model parameters β and q for link lengths centered at each value of L. The average fade width was similarly calculated for each subset of model-generated data $\tilde{S}_L$ according to 7.1 to see which, if any, value of model parameters resulted in a match between observation and model. Figure 7-7 displays the results of this experiment. Here note that the fade width decreases for more strongly faded channels. Further we see that there is a value of β that results in a close match between data and model across all fading levels with respect to average width,

$$\hat{\beta} = 4.3 + 0.005 \cdot d_o$$

Here we see that the decay-rate (β) tends to increase with increasing link-length providing an estimator for β in this environment with an empirical rms error of 730KHz. A physical explanation of this behavior is that the paths of first-arrival will presumably utilize few scattering surfaces to propagate down the street, e.g. diffraction around corner, single bounce from scatterer at head of street, while the trailing paths will utilize the building surfaces lining the street many times over. As
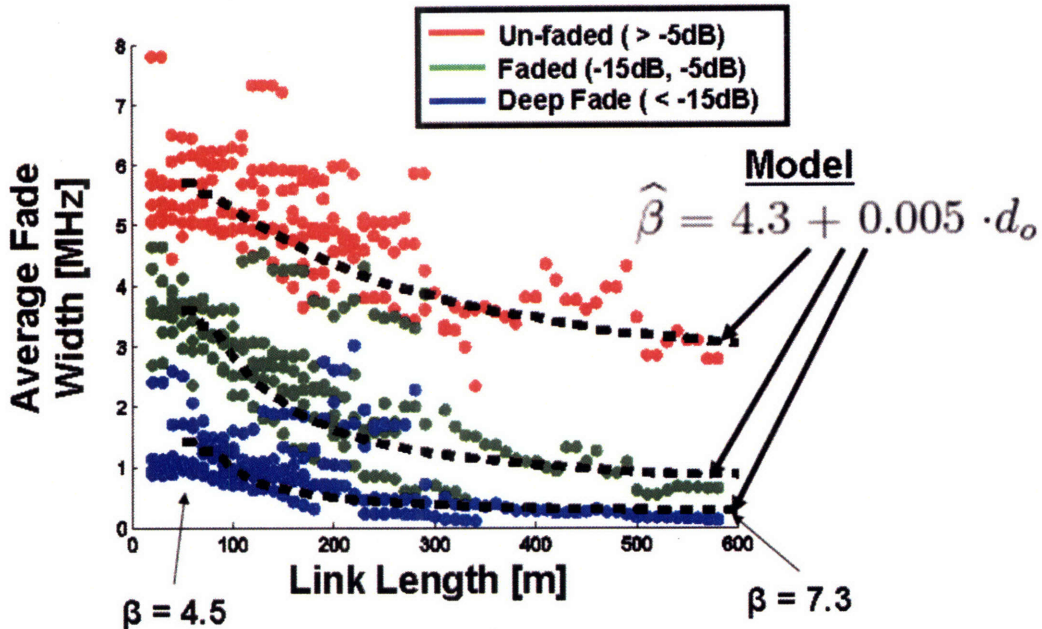
Figure 7-7: Multipath Model Performance: Average Fade Width in street links

we move down the street then the ratio of scatterer interaction between the MPCs of first arrival and the rest tends to decrease, resulting in a higher-decay factor further down the street.

While the results of Figure 7-7 support the validity of the model, a more complete test considers the complete distribution of fade width as opposed to only the mean. Our data set is not large enough to obtain distribution convergence for every set of link lengths. However we can visually inspect the empirical distributions for those subsets S_L with the largest number of samples and compare them to the distributions predicted by the model. Figures 7-8- 7-10 display the distributions for two link lengths (short: 70m, long: 390m) across all three fading levels. In the figures the model distributions have been estimated by interpolating the histogram formed from the simulated model-driven data. Here we observe similar distribution shapes between model and data, adding further support to the validity of the model.

We now consider the same calculation over a different type of environment. Figure 9-4 contains a gps image of a ground-to-ground environment (campus parking lot) that contains a richer collection of scattering surfaces than the typical street environ-
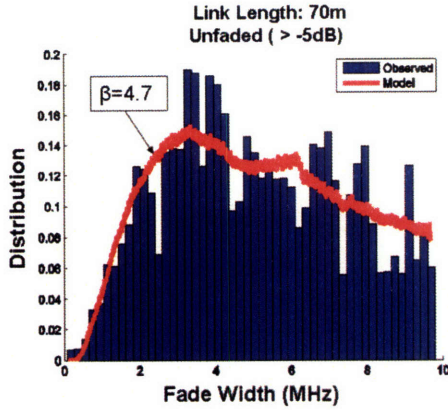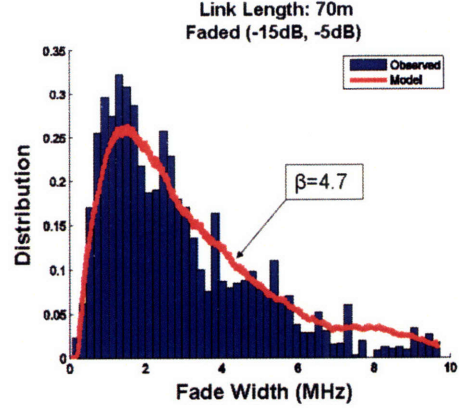
169

Figure 7-8: Fade Width Distribution

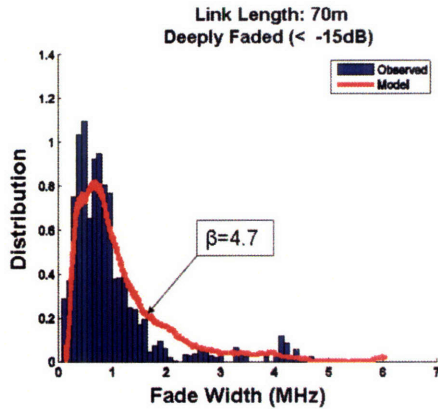Figure 7-9: Fade Width Distribution

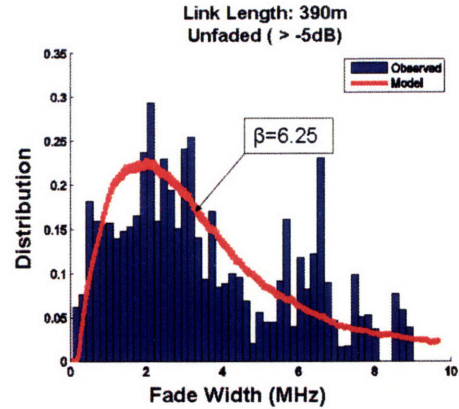Figure 7-10: Fade Width Distribution

Figure 7-11: Fade Width Distribution

ment. Again we consider the multipath distribution, but within this rich scattering environment at a single link length of 50 meters. Figures 7-14 and 7-15 display the resulting histogram and corresponding model distribution with parameter values that give the best match.

In the model we have fixed d_o at 50 meters and q at $1 \frac{\text{MPCs}}{m}$ to match the dense arrival rate found for the 50m street data. Here we see that the histograms in Figures 7-14 and 7-8 are quite different even though they both have approximately the same link lengths. The decay-rate (β) predicted for this environment is 2.3 which is approximately one half of the rate of 4.7 found for the street environment of that link length. Physically this is intuitive as this alternative environment allows single-bounce trailing MPCs, thus reducing their expected attenuation relative to the MPC of first-arrival.
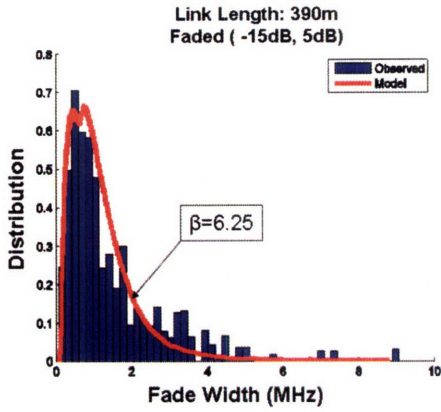
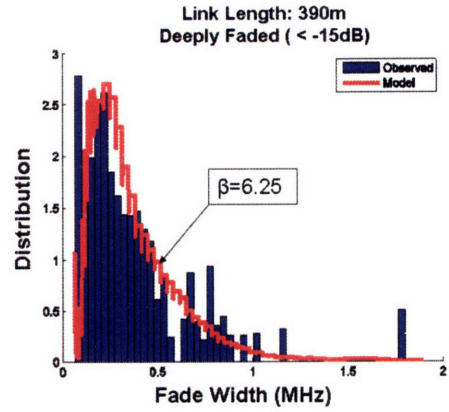Figure 7-12: Fade Width Distribution
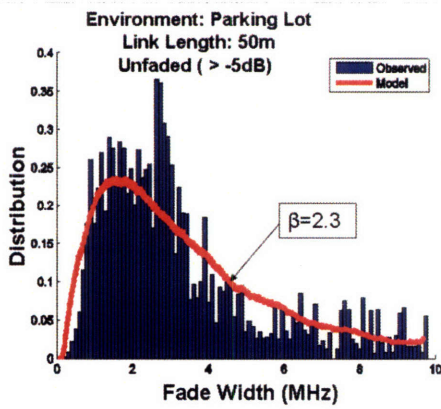

Figure 7-13: Fade Width Distribution

Figure 7-14: Fade Width Distribution
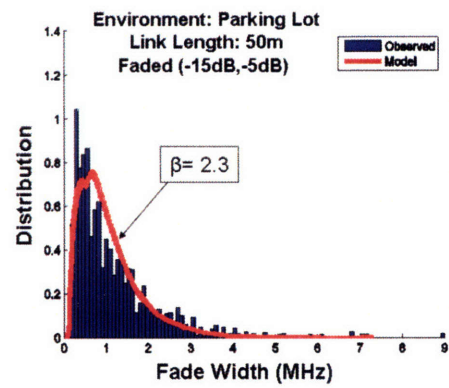
Figure 7-15: Fade Width Distibution

171

Chapter 8

Time/Stability Characteristics

8.1 Background and Theory

As objects within the propagation environment move, including the link-ends themselves, the channel response changes. This occurs as small movements of scatterers introduce small propagation delays of the signal paths associated with those scatterers. At the receiver this results in the superposition of propagation paths with different relative phases which can result in a very different channel profile as a function of frequency. Channel dynamics due to the movement of the link nodes themselves are identical to the spatial characteristics of the channel which we study in Section 9. Here we focus on channel instability due to changes in the environment for spatially fixed link-ends.

From a system design perspective we are interested in time stability characteristics as this behavior indicates how often we will have to refresh our estimate of the channel for various communication protocols. Typically time characteristics are measured according to a time coherence parameter which indicates the maximum length of time the channel can be expected to remain stable. Channel estimate refresh rates are then set according to this parameter in order to ensure their accuracy.

8.2 Experiments and Analysis

Here we study the stability characteristics of the wireless channel by analyzing the multiple-antenna data sets described in Chapter 6. Our data sets are organized as a set of channel snapshots associated with each physical realization of transmitter and receiver locations. Each snapshot is a 33kHz resolution estimate of a single 10MHz band measured coherently at eight antenna elements. Recalling Section 4.8.5, the time between snapshots is approximately 300ms when sampling eight antennas due to the time required to download snapshot buffers to the hard disk of the cpu. In our measurement campaign we recorded 15 snapshots (a 5-second window) per measurement location in order to study the stability of the channel. Figures 8-1 and 8-2 display examples from the data set for durations of 2.5 and 3.5 seconds respectfully. Note that each set of snapshots is taken within 5 seconds, however some of those snapshots do not contain packets necessary for channel estimation. See Section 4 for more details on the nature of the collection system.

The first metric that we apply to our channel data to measure stability is the probability that the power received over a particular channel remains stable to within +/- XdB after at least 300ms of time has passed, which we will denote as,

$$P(\text{Stability} \geq X \text{ dB}) = \text{Prob}(-X\text{dB} \leq \frac{|h_o|^2}{|h_t|^2} \leq X\text{dB})$$

where h_o denotes the instantaneous narrow-band frequency response at the reference time and $t \geq 300$ms. Specifically we calculate this by considering a single snapshot per link and determining the percentage of the remaining snapshots that have a squared amplitude within that window (+/- XdB relative to the baseline snapshot). This is calculated over each of the 300 frequency taps (10Mhz band/33Khz resolution), 8 antennas, and L links (hundreds) to arrive at an overall result. Figure 8-3 displays the resulting metric applied to a set of data taken from a campus parking lot (ground-to-ground link lengths ranging from 50 to 200 meters).

Here we see that the probability of power received remaining stable to within 3dB is approximately 90%. This suggests that the channel response remains fairly stable

Figure 8-1: Time Evolution of the Channel: Snapshots taken from ground-to-ground links on the order of 100 meters

even up to 5 seconds, which is quite long. However inspection of Figures 8-1 and 8-2 do not completely support a stable channel model. Specifically the channel at frequencies with high fading (nulls) appear to be quite unstable as compared to those with low fading. These observations suggest that there may be a strong dependency between stability and the fading level. To test this theory we repeated the experiment but stratified the result based on the level of small-scale fading. Recall from Section 7.2 the fading level f is quantified as the amount of power received relative to the large-scale attenuation for that link:

$$f(h_{l,r,f,t}) = \frac{|h_{i,j,k,m}|^2}{P_{ave}}$$

$$P_{ave} = \sum_{l=1}^{L} \sum_{r=1}^{R} \sum_{f=1}^{F} \sum_{t=1}^{T} \frac{|h_{l,r,f,t}|^2}{L \cdot R \cdot F \cdot T}$$

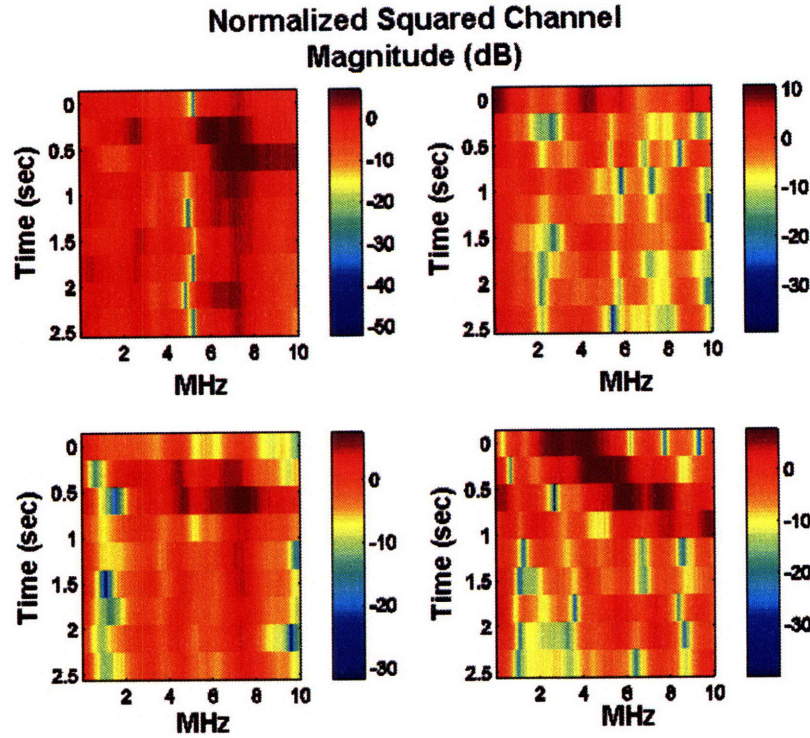where f(h) denotes the fading level for a particular channel realization and P_{ave} is the
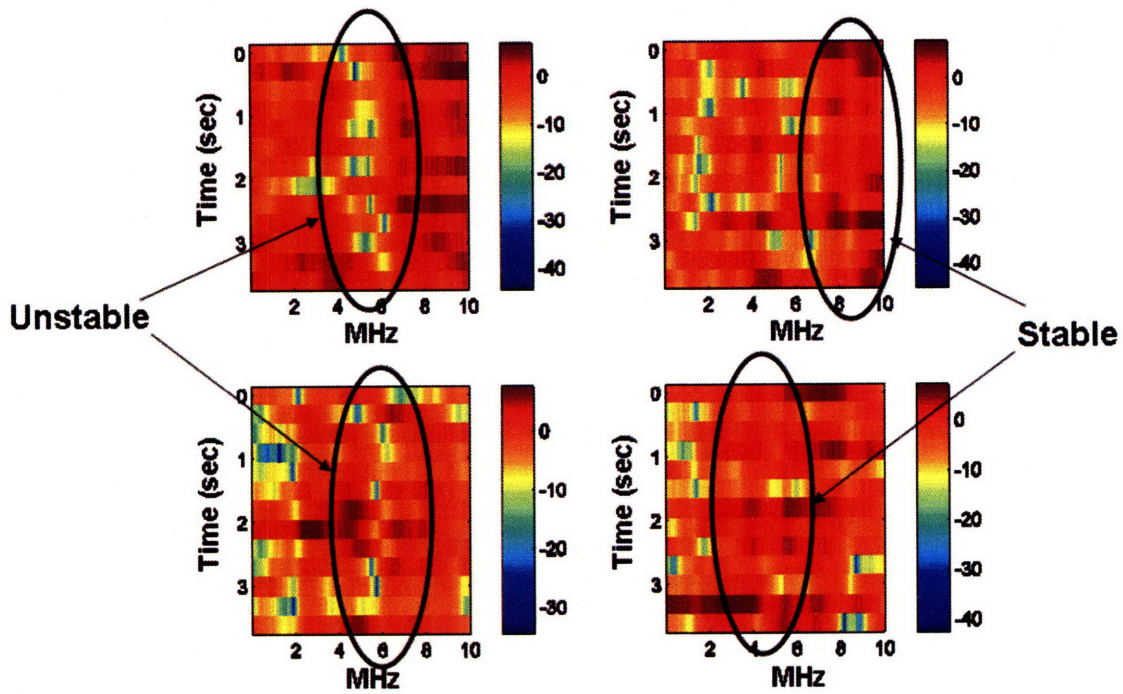
Figure 8-2: Time Evolution of the Channel: Snapshots taken from ground-to-ground links on the order of 100 meters

average power received over the R receivers (8), F frequencies (300), T snapshots (15), and L link realizations at that link-length. We then compute our stability metric as a function of fading level. Figure 8-4 displays the results of this analysis. The x-axis of Figure 8-4 displays the fading level of the channel (relative to P_{ave}). Here we observe a clear relationship between stability and the level of fading. Specifically highly faded channels (nulls) are quite unstable whereas channels with power close to the mean (0 dB in the figure) or better experience high stability. Physically we can support this result by considering the behavior of individual multipath components (MPCs). Obtaining a null requires precise phasing between each of the MPCs arriving at the receiver. Small delays in the arrival of these signal paths due to small movements of scatterers in the environment result in relative phase perturbations between the signal paths at each frequency.

To illustrate this point we have conducted a simulation highlighting this behavior. In the simulation a narrow-band channel is constructed as the superposition of 10

176

Figure 8-3: Channel Stability vs Threshold
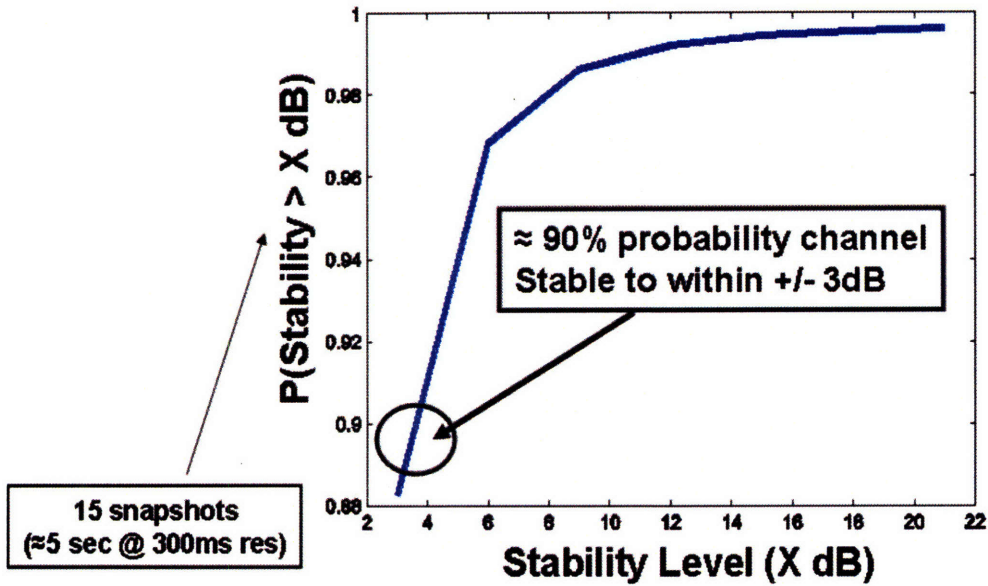
multipath components each of which is generated according to a circular symmetric complex gaussian distribution. An additional channel is then constructed by perturbing the phase of each of the original multipath components by a random phase offset that is uniformly distributed over some tolerance, e.g. $\frac{\pi}{64}$. This simulates how the overall channel response will change when relative delays between multipath components are introduced by small dynamics in the environment. A large number of simulation runs were then carried out (tens of thousands) so that a statistical distribution of the stability characteristics could be constructed. Figure 8-5 displays the results of the simulation. The phase error denotes the maximum phase offset (as a percentage of 2π) that each MPC can take on due to delays caused by changes in the environment. Here we see that the simulation results match our claim that faded channels are much more sensitive to small environment-induced delays than their less faded counterparts.

We have till now computed our stability statistics in such a way that each offset between snapshots, whether it be 300 ms or 5 seconds, has been treated the same. However it is additionally of interest to observe how these statistics change as a function of elapsed time. That said we have repeated the above analysis and calculated

177
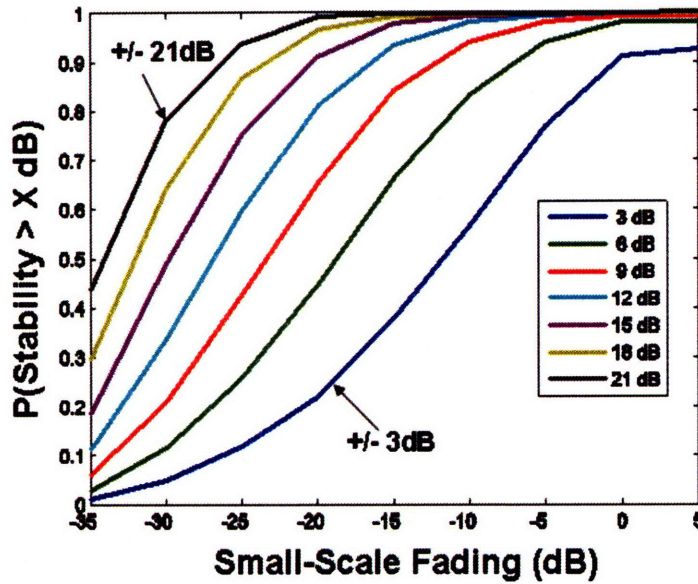
Figure 8-4: Channel Stability vs Fading Level

the statistical distributions separately for each possible snapshot offset (integer multiples of 300ms up to 5s). The results of this analysis are displayed in Figure 8-6. Here we see that the change in the stability characteristics are relatively small as we move from offsets of 300ms to offsets of nearly several seconds. This suggests that high frequency (smaller than 300ms) environment dynamics dominate the stability characteristics of the channel.

While we have analyzed the stability characteristics of the channel magnitude it is additionally of interest to understand the associated behavior of the channel's phase. In protocols where multiple frequency tones are utilized coherently, e.g. OFDM, it is necessary to refresh the complete channel estimates, including phase, at a rate faster than the stability time of the channel to ensure effective communication. Given this motivation we have repeated the above analysis for the phase components of our data sets. Specifically for each set of snapshots the phase is computed as the phase relative to the strongest channel across frequency as this is presumably the most stable reference point which to work from. Figure 8-7 displays the results of this analysis.

Here we use the same metric as before, the probability of being stable with respect
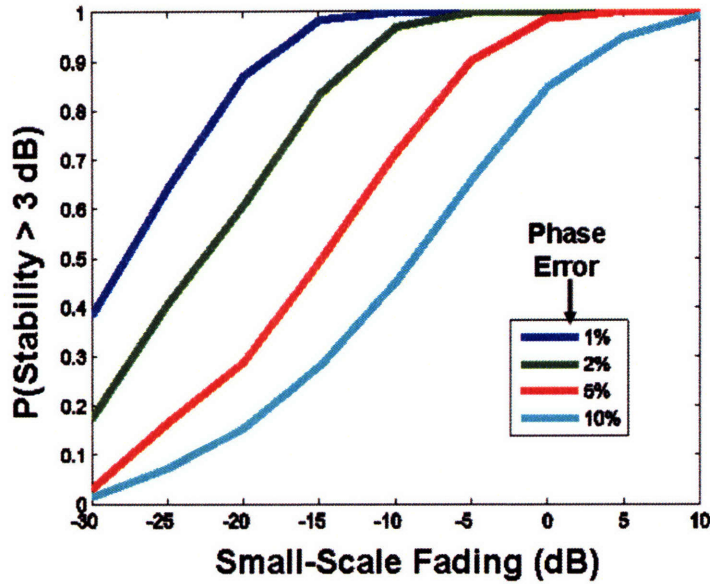
Figure 8-5: Channel Stability (Simulation): Stability vs. MPC phase error

to a threshold level. In this case the threshold is computed as a percentage (of 2π) of change in the phase of the channel. Analogous to the results before the phase stability increase with respect to decreased channel fading. However the phase of the strong channels seems to be relatively less stable than their associated magnitudes. Physically this can be justified by the notion that small phase offsets of the individual multipath components are more likely to push the phase away from its previous state than destructively combine to form nulls.

8.3 Channel Stability Model

In this section we consider the problem of modeling the time characteristics of wireless channels based on our observations in the previous section. In the above analysis we found that the channel is sensitive to time offsets of 300ms and that the level of sensitivity was dependent on the fading level of the channel. In addition we found that these stability characteristics were insensitive to additional time offsets, even as long as 5 seconds. These observations suggest that the time characteristics of the channel are such that it changes due to high-frequency (faster than 300ms) environmental
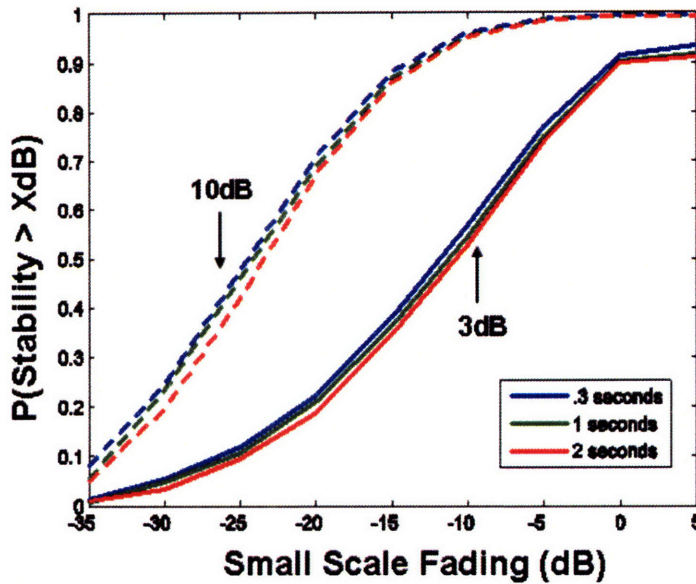
Figure 8-6: Long Duration Stability

dynamics but that this process is mean reverting making the channel insensitive to longer durations.

We can support these statistical observations by means of a physical explanation. In a completely static environment, all scattering objects that relay multipath components (MPCs) from transmitter to receiver are completely stationary. Given this the relative phasing between MPCs is constant and the channel response is constant over time. However high frequency changes in the channel response correspond to high frequency dynamics of the scattering objects in the environment. Specifically the scattering objects encountered in our measurement campaigns have been predominantly either buildings, trees, or vehicles. That said, high-frequency dynamics experienced by these types of objects are usually caused by either the movement of trees from the wind or vehicular traffic. Given this dynamic framework we can consider the set of multipath components comprising the channel response to be categorized into two regimes, namely those that are sensitive to the high-frequency environment dynamics (tree/wind, moving vehicles, denoted set S) and those that are not (building dominated, etc, denoted set U). The narrow-band channel response can then be modeled as,

180
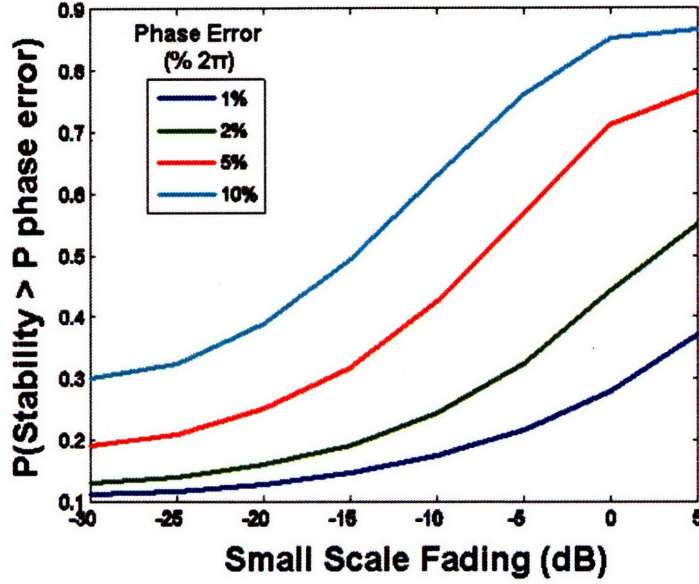
Figure 8-7: Phase Stability

$$h_t = \sum_{j \epsilon S} p_{j,t} + \sum_{j \epsilon U} p_{j,t}$$

where $p_{j,t} \epsilon \mathbb{C}$ denotes the complex channel response of the jth multipath component (MPC) at time t. Here the MPCs, $p_{j,t} \epsilon S$, are considered to be stable over long time lengths (in our observations at least 5 seconds). Physically we can consider this set as those MPCs that utilize only stable core components of the scattering environment such as buildings and immobile vehicles to propagate across the link. The stability characteristics of these components are such that they are slowly varying, anywhere from several seconds, minutes, to hours. The slow variation can be caused by thermal/humidity factors or the movement of once stationary objects (parked cars). Alternatively the MPCs, $p_{j,t} \epsilon U$, are such that they are unstable over very shore time horizons (in our measurements sub 300ms). These are paths that scatter off of trees and traverse streets with heavy traffic. The variation of paths in this regime can be quite large in both magnitude and phase as traffic blocks/unblocks propagation and trees move on the order of wavelengths due to wind.

Given this framework, if the scattering environment is such that the channel re-

181
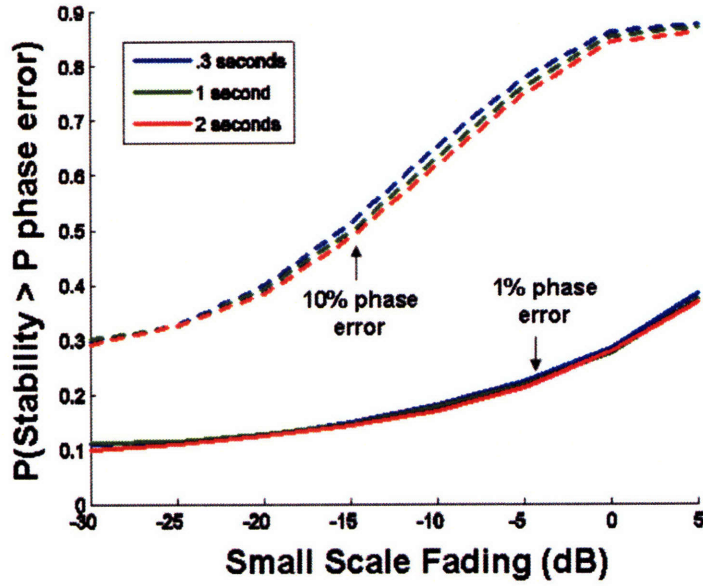
Figure 8-8: Long Duration Phase Stability

sponse h_t is not dominated by a small number of MPCs then we can model the response due to each subset of MPCs (S and U) as being independently gaussian distributed (Rayleigh fading). This assumption is supported by our analysis in 7.2. Specifically we can model this behavior as,

$$h_t = X_S + X_U^t$$

$$X_S \sim \mathcal{CN}(0, \sigma_S^2)$$

$$X_U^t \sim \mathcal{CN}(0, \sigma_U^2)$$

where X_S and X_U^t denote the contributions to the channel response from the stable and unstable MPCs respectfully. Note that X_U^t is a function of time and can be considered to be independent over time durations of several milliseconds. The stability of the link then is determined by the ratio $\frac{\sigma_S^2}{\sigma_U^2}$. The higher this ratio, the more stable the channel will be on average. Note though however that even for very large values of $\frac{\sigma_S^2}{\sigma_U^2}$ a particular link realization is not guaranteed to be stable as the response due to the stable paths may be highly faded.

For a particular realization of the stable MPCs ($X_S = \sqrt{\frac{K}{K+1}} \cdot \exp^{j \cdot \theta}$) this model reduces to the popular Rician fading model,

$$h_t = \sqrt{\frac{K}{K+1}} \cdot \exp^{j \cdot \theta} + X_U^t$$

$$X_U^t \sim \mathcal{CN}(0, \sqrt{\frac{1}{K+1}})$$

where the parameter K is referred to as the Rician K-Factor and quantifies the stability of the link as the ratio of the squared magnitude of the fixed component (realization of stable MPCs) and variance of a random component (unstable MPCs). A complete description for our fading model in the time domain is,

$$h_t = X_S + X_U^t$$

$$X_S \sim \mathcal{CN}(0, \frac{S}{S+1})$$

$$X_U^t \sim \mathcal{CN}(0, \frac{1}{S+1})$$

where S, which we refer to as the S-factor, is the ratio between the average power in the stable to unstable MPCs:

$$S = \frac{\sigma_S^2}{\sigma_U^2}$$

In our channel measurements (as will be shown in the next section) we have observed a non-gaussian structure (fat tails) to the fading behavior in the time domain. Physically we can justify this observation as there being a non-negligible probability of the stable components falling in a fade.

8.3.1 Model Performance

We now test the performance of this model by comparing it to the characteristics observed in our measurements. The model parameter S is generally non-stationary so we stratify the data according to two degrees of freedom over which this parameter can vary, namely: environment and link length. For each subset of the data set we

calculate the performance of the model in predicting the realized fading characteristics (time domain). The time-domain fading distribution of each data set is calculated from,

$$\hat{h}_{r,t} = \frac{h_{r,t}}{\bar{h}_r}$$

$$\bar{h}_r = \sum_{t=1}^{T} \frac{|h_{r,t}|^2}{T}$$

where each channel snapshot realization $h_{r,t}$ has been normalized by the average power across T (≈ 10) snapshots, and the total number of realizations R is proportional to the number of antennas (8), frequencies (300), and links (L) for that set. The S-factor is then found numerically by finding the value of S that minimizes the distribution-weighted difference between the empirical ($f_e(x)$) and model ($f_r(x, S)$) distributions:

$$\text{Error (E)} = \int_0^\infty |f_e(x) - f_r(x, \hat{S})|^2 \cdot f_e(x) \cdot dx$$

Figures 8-9, 8-10, 8-11, and 8-12 display example distributions from two measurement environments at two link lengths each. Additionally Figure 8-13 displays the performance of the Rician fading model as applied to one of these example environments. Note that the fading level $\hat{h}_{r,t}$ is denoted as x in these figures.
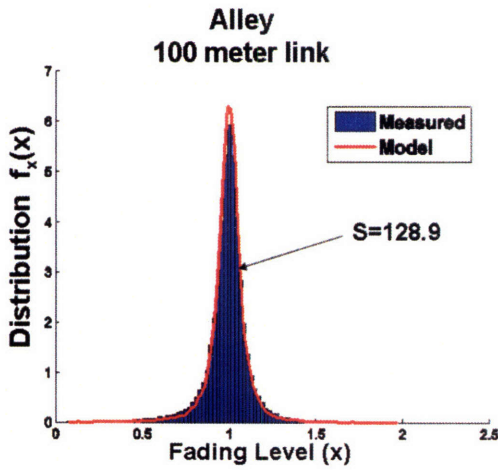

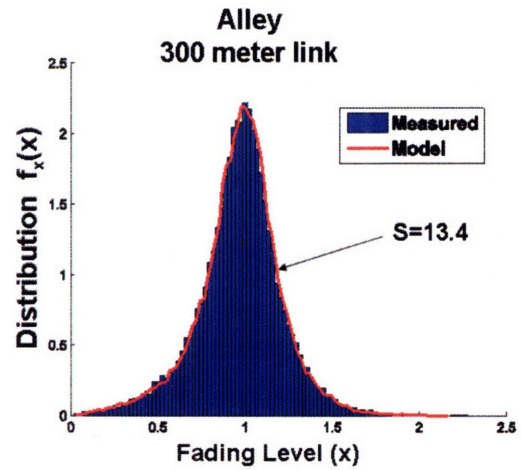Figure 8-9: Model Performance: Time-domain fading

Figure 8-10: Model Performance: Time-domain fading

In these figures we see a dependence of S on both environment and link length. Ad-

184
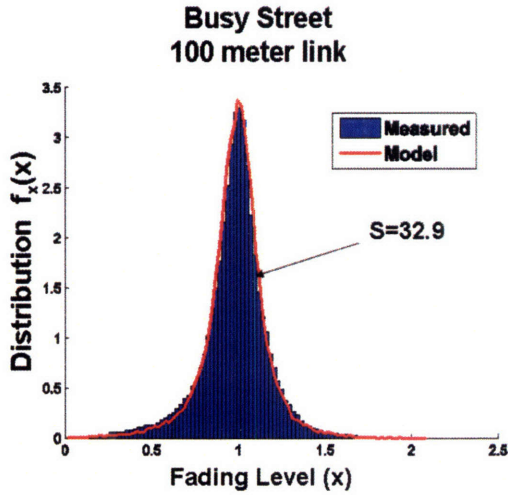
Figure 8-11: Model Performance: Time-domain fading
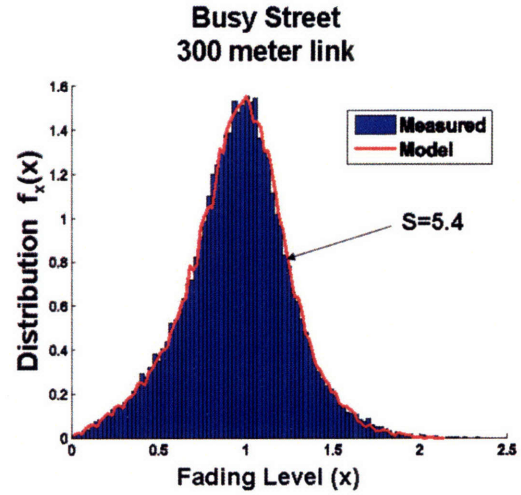
Figure 8-12: Model Performance: Time-domain fading

ditionally we see a close distributional match between measurements and our model. Here we note that the empirical distributions are distinct from the Rician fading distribution as they contain fatter tails. This shape arises from the possibility that the stable MPCs may fall in a null which is not accounted for in the standard Rician model where the fixed component is deterministic.

We have shown the model is accurate when S is known, but as seen in Figures 8-9 and 8-12, the shape of the fading distribution is highly dependent on the parameter S. Given this, obtaining an estimator for S will be crucial in applying the model in practice. In ground-to-ground links we would intuitively expect the S-factor to decrease with increased link-length given that longer links have a higher probability of interacting with moving scatterers. To test this theory we have displayed a scatter plot of the calculated S-factors as a function of link-length in Figure 8-14 across all street data. Here we see a log-linear relationship between S-factor and link length providing us with an estimator:

$$\hat{S} = -13 log_{10}(d_o) + 44 \text{ [dB]}$$

that has an empirical rms error of 3.3dB. To test if such an estimator is available for air-to-ground links we have displayed the same scatter plot for those links in
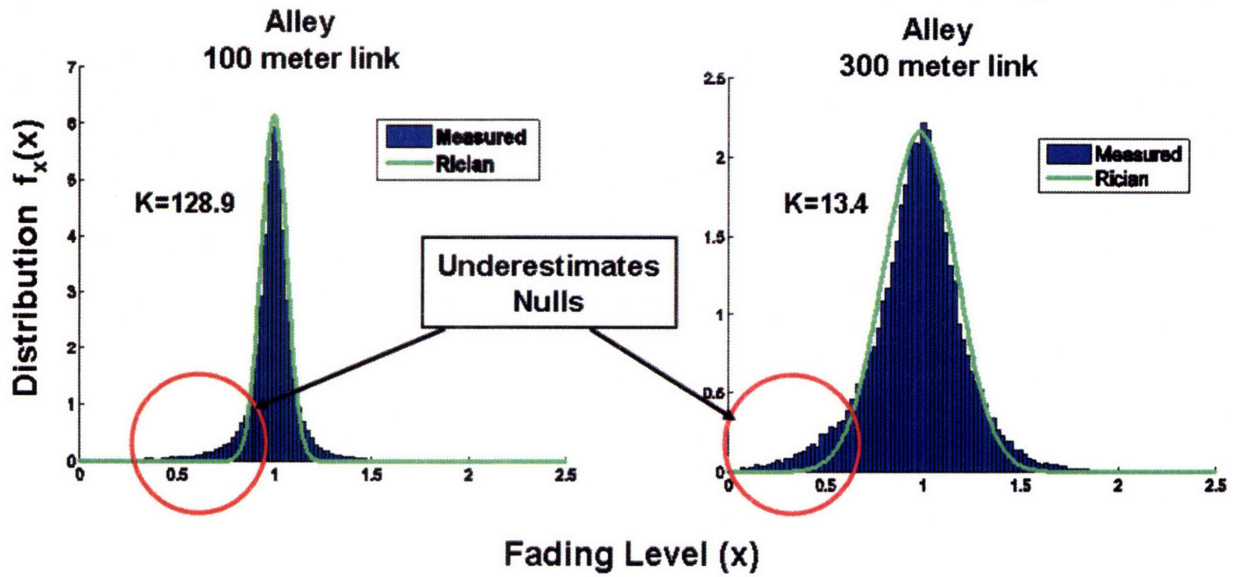
Figure 8-13: Rician Model Performance (Time-domain fading): Tendency to under-estimate tail events.

Figure 8-15. Here we see little relationship (least-square slope = -0.08) between the S-factor and link-length. This can be physically justified by the fact that the majority of the link length (first segment in our air-to-ground path-loss model) is above the scattering line of the environment which in general does not contain any moving scatterers. Channel instability then in these links is caused by moving scatters in the local environment of the ground link making the stability characteristics largely independent of link-length. However note that the range of S-factors observed in this link regime was smaller and had an empirical mean and standard deviation of 12.7dB and 3dB respectively. We also mention the dependency of S-factor on the environment. Table 8.1 displays the average S-factors measured over 9 different environments. Here we note the lower S-factors present in areas of the MIT campus (parking lots, busy streets) where there is a higher amount of traffic as compared to environments measured in residential areas of greater Cambridge. This shows that the environment under consideration should also factor into the estimate of S, namely bias to the right side of the distribution for low traffic areas and vice versa in the alternative case.

$$\hat{S} = -13\log_{10}(d_o) + 44 \text{ [dB]}$$
$$e_{rms} = 3.3 \text{ dB}$$
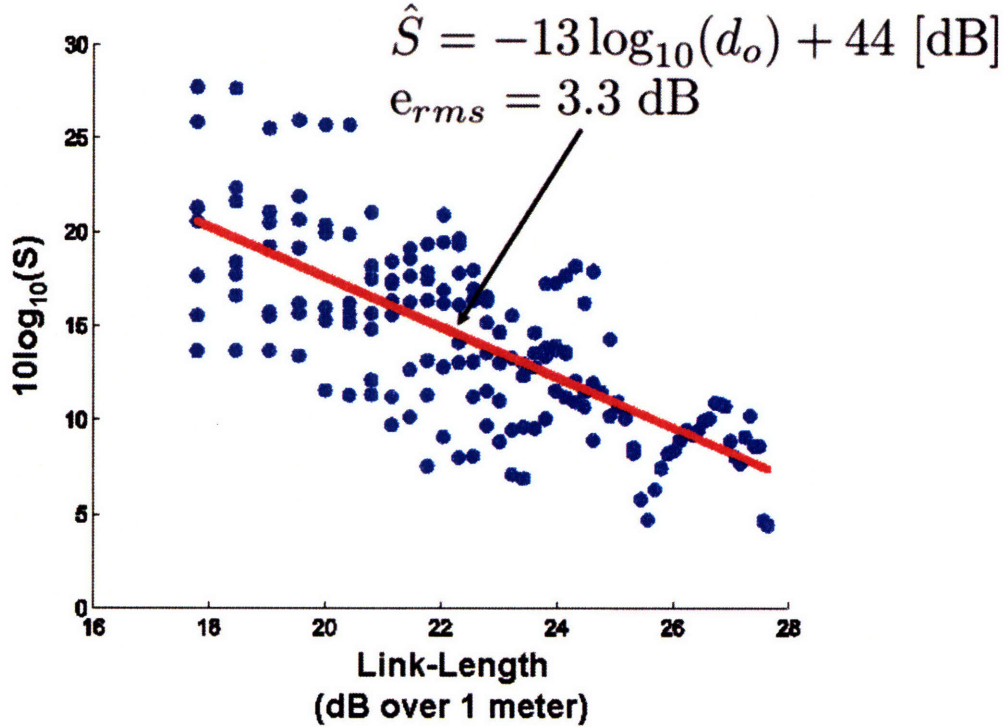
Figure 8-14: Street Environments: Estimating S from link length

8.3.2 Note on the Stability level of Unstable Paths

We found that the unstable MPCs of the channel changed faster than the processing rate of our system (300ms). In outdoor environments we would expect the highest velocities to be at most 100 miles per hour, e.g. moving vehicles and wind induced movements. With the channel having a sensitivity level on the order of half a wavelength of the carrier frequency we would expect the highest frequency dynamics to be influential at rates as fast as,

$$\frac{0.062\text{m}}{100\text{m.p.h.}} = \frac{0.062m}{44.7m/s} = 1.4ms << 300ms$$

This is consistent with our findings. Such changes are generally too fast for most communication systems to track in any event.

187
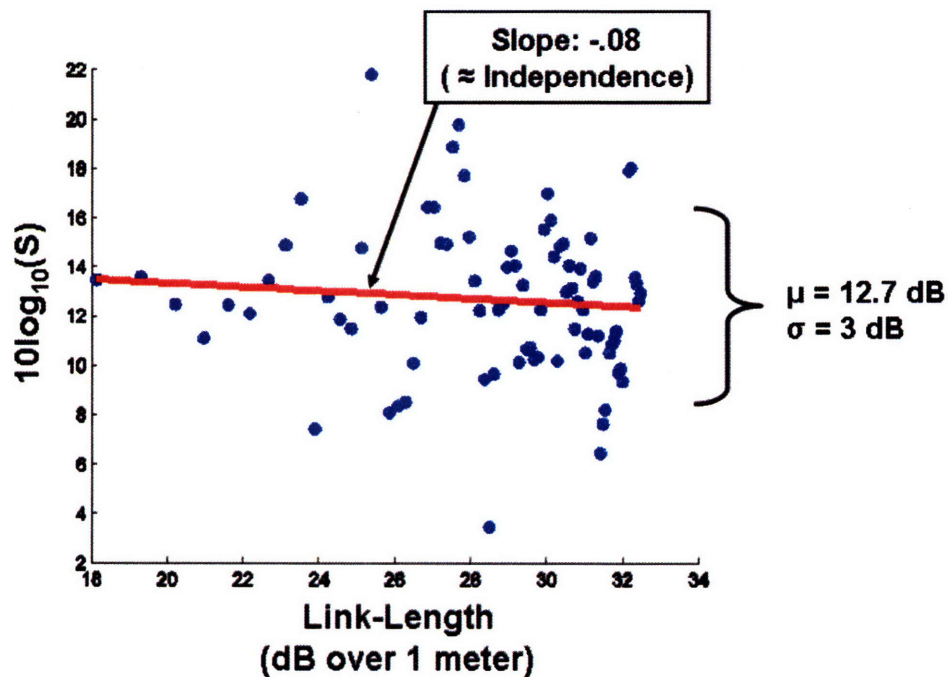
Figure 8-15: Air-To-Ground Links: Independence between S and link length

Table 8.1: Average S-factor over different environment types

No.	Type	$\hat{S}$
1	Campus Street (Main)	11.2
2	Campus Street (Vassar)	20.3
3	Air-to-Ground	22.8
4	Parking Lot (Stata)	20.1
5	Parking Lot (Main Lot)	42.7
6	Alley	100.8
7	Residential	106.0
8	Residential	89.4
9	Residential	84.2

Chapter 9

Spatial Structure

9.1 Theory

As discussed in Chapter 2, MIMO systems take advantage of orthogonal spatial sub-channels formed in multipath environments to increase channel capacity. For a given system and corresponding array topology, the potential utility of spatial multiplexing is completely dependent on the spatial structure of the channel environment. Several models have been proposed in the literature that attempt to capture the important spatial characteristics of the MIMO channel into a simplified representation.

9.1.1 Analytical Models

Analytical MIMO channel models have been proposed as a practical alternative to the double-directional model. These analytical models take the approach of directly modeling the channel matrix H, often statistically, instead of modeling the details of the underlying propagation mechanisms. The underlying assumption in this class of models is that the propagation environment is Rayleigh fading. If this is the case then the statistical behavior of the channel matrix, H, is completely described by its second order statistics, i.e. the covariance matrix R of its entries.

1. **Independent and Identically Distributed (IID) Model:** The most simplistic analytic channel model is IID model. Here it is assumed that all entries

189

of the NxM channel matrix, H, are independent and identically distributed with a circularly symmetric complex gaussian distribution, i.e. R is the identity matrix. In practice this model can overestimate spatial multiplexing gain when there exists correlation among channel matrix entries, which is often the case.

2. **Kronecker Model**: Assuming that the entries of the NxM channel matrix, H, have a complex Gaussian distribution (Rayleigh fading), the distribution of the channel matrix is completely specified by its second order statistics, i.e. the covariance matrix, R, of its channel entries, where:

$$\text{vec}\{H\} = R^{\frac{1}{2}} \cdot \text{vec}\{G\}$$

Here vec{} refers to the column stacking operator (stacks columns of a matrix into a single column vector, e.g. NxM -> NMx1), and G is an NxM iid complex gaussian matrix. Given that there are N·M channel entries, the corresponding covariance matrix, R, is of size (N·M) x (N·M). With the generally large size of the covariance matrix, R, the Kronecker model attempts to reduce this complexity by simplifying the structure of R. More specifically, the Kronecker model assumes (ignoring scale) that the covariance matrix is in the form,

$$R = R_T \otimes R_R$$

where $\otimes$ denotes the Kronecker product [1] and R_T, R_R are the one-sided covariance matrices at the transmitter and receiver respectfully defined as:

$$R_T = E[(H^H H)^T]$$

$$R_R = E[H H^H]$$

---

[1]

$$A \otimes B = \begin{pmatrix} a_{11}B & \dots & a_{1m}B \\ a_{21}B & \dots & a_{2m}B \\ \vdots & \vdots & \vdots \\ a_{n1}B & \dots & a_{nm}B \end{pmatrix}$$

Here we see that the Kronecker model assumes that any correlation among channel matrix entries can be separated into the product of the correlation contributions at the receiver and transmitter [20], which is in general not physically justifiable [17].

9.2 Background and Research Objectives

As outlined in section 9.1 there is a variety of methods for modeling the spatial structure of the wireless channel. At one extreme the Double-Directional channel model assumes complete knowledge of the channel as a function of direction at both link ends, delay, and polarization. Given that this level of description is in general impractical to obtain, we are focused in our research on analytical MIMO channel models. In particular we consider the Kronecker model [20] which is the most heavily utilized analytical model that includes spatial correlation (i.e. outside the IID domain) and is additionally included as part of the model suite for the multiple-antenna WiFi extension 802.11n.

Several papers [18], [19], [20] have claimed to validate this model by presenting empirical results that support its ability to predict various channel metrics. However the applicability of these results has been questioned in [17] for reasons including the limited size of the arrays (2x2 in some cases) used in the measurements and the lack of correlation in the measured channels. [35] provides measurement results corresponding to larger array sizes and more highly correlated channels. In their indoor experiments they found a tendency of the Kronecker model to underestimate channel capacity. In [17] the authors present both the necessary mathematical and propagation conditions that must hold in order for the Kronecker model to be valid. The two necessary mathematical conditions are:

1. **Mathematical Condition I:** The magnitude of the correlation coefficient between any two receive (transmit) antennas is independent of the transmit (receive) antenna. i.e. $E[h_{ik}^* h_{jk}] = r_{ij}$ for any pair of receive antennas {i,j} and transmit antenna k.

2. **Mathematical Condition II:** The correlation coefficient between two channel matrix entries corresponding to distinct transmit and receive antennas is equal to the product of their corresponding transmit and receive correlation coefficients. i.e. $E[h_{ik}^* h_{jm}] = r_{ij}^* t_{km}$ where $i \neq j \neq k \neq m$

Here the authors point out that these mathematical conditions are not sufficient in guaranteeing the validity of the Kronecker model for any array configuration in the environment under consideration. In order for the environment to be considered, as referred in [17], Kronecker-structured it must be that the following necessary and sufficient propagation conditions hold,

1. **Propagation Condition I:** The receive (transmit) array must be composed of elements with identical radiation patterns and orientations. Additionally the spacing of these elements must be small, several wavelengths.

2. **Propagation Condition II:** The Angle-Of-Arrival (AOA) and Angle-Of-Departure (AOD) spectrums are independent. i.e. the angle of departure (transmitter) gives no information as to the angle of arrival (receiver) and vice versa.

Each propagation condition above implies its corresponding mathematical condition. Given the lack of thorough performance analysis of the Kronecker model in the literature [17], our objective in this domain is to provide such analysis. In particular we are interested in better understanding the ability of the model to predict the structure of the channel over a variety of outdoor environments. In addition we would like to look at the relationship between predictive performance and environment structure and compare this result to the propagation validity conditions outlined above.

9.3 Measurement Campaign and Setup

1. **Transmitter**

    (a) **Antenna Element:** One 8dBi dipole

    (b) **Antenna Polarization:** Vertical
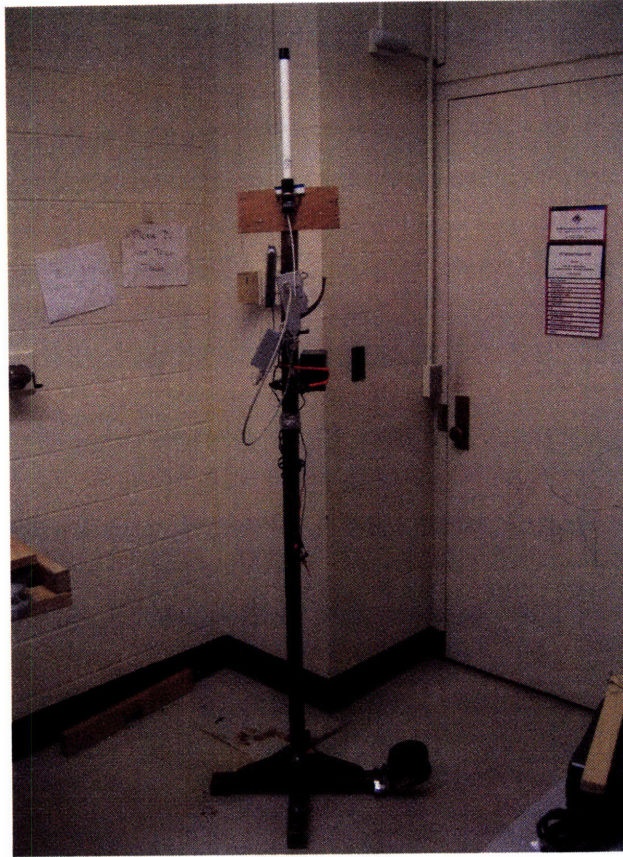
Figure 9-1: The Channel Sounder mounted to a coat rack

(c) **Mounting:** Electronics and antenna mounted to 7-ft wooden coat rack. Coat rack placed into wooden jig for simulating 7 transmit antenna locations. See Figures 9-1 and 9-2.

2. **Receiver**

(a) **Antenna Elements:** Seven 2-dBi dipoles, One 8-dBi dipole

(b) **Antenna Polarizations:** Vertical

(c) **Antenna Array:** Arranged in a linear, half wavelength spaced array with a single reference antenna spaced tens of wavelengths from the other elements. See Figure 9-3.

(d) **Mounting:** System installed in van with receiver mounted to the roof of the van.
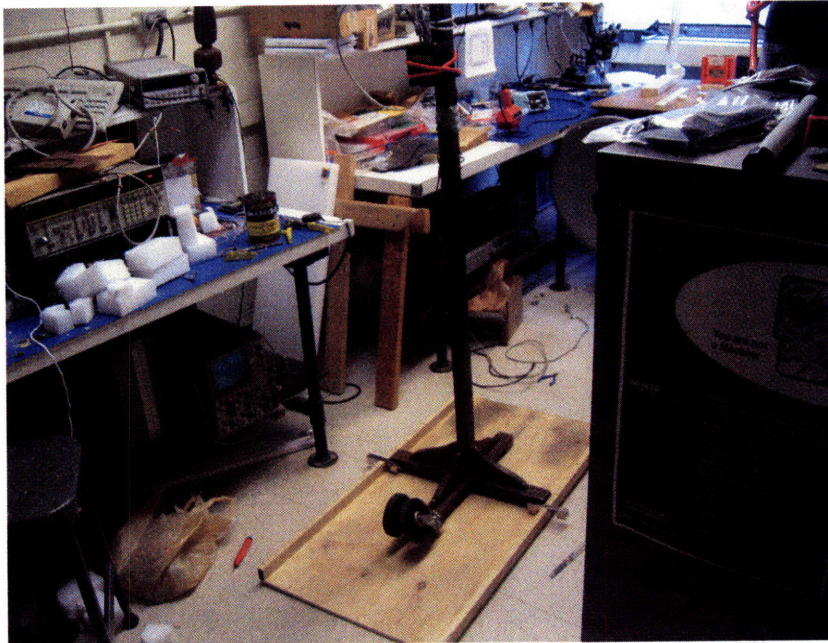
Figure 9-2: Simulation of array at the transmit end.

3. **Measurement Setup:** For each measurement scenario the van housing the receiver is parked and left stationary. For each scenario several full MIMO channel measurements are taken. A full MIMO channel measurement consists of seven transmitter locations along a jig that simulates a half-wavelength linear array. Several full MIMO measurements are taken in order to gather enough statistics for estimating the Kronecker Model parameter space.

4. **Environments:** Outdoor MIT Campus and residential neighborhoods in Cambridge.

9.4   Analysis and Results

The purpose of this experiment is to directly measure the performance of the Kronecker model in approximating the true MIMO channel. Here we will define performance as the accuracy of the model in predicting the spatial multiplexing structure of the channel. This analysis can be broken into the following steps: channel matrix construction, Rayleigh validation, stability validation, parameter estimation, and
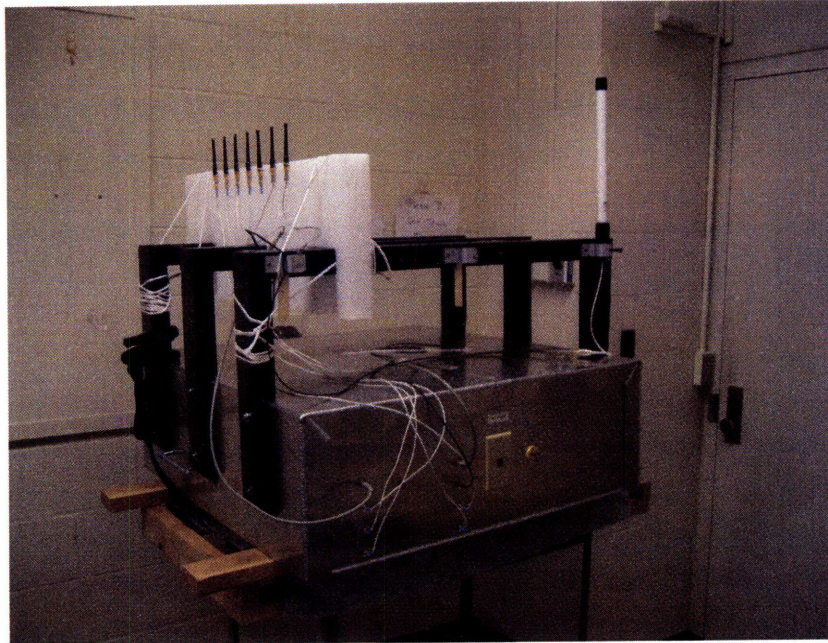
Figure 9-3: Receiver Array for Kronecker Performance Analysis Experiments.

performance analysis.

9.4.1 Channel Matrix Construction

The first step of the analysis is to obtain the channel matrices for each channel configuration from the data set. A channel configuration is defined as a particular link scenario, i.e. transmitter and receiver positions. For each configuration we have numTaps · numPositions channel matrix realizations. Here numTaps refers to the number of frequency taps in the channel estimation (here 300 @ 33-Khz resolution) and numPositions is the number of full MIMO channel measurements (distinguished by spatial offset) taken (here 7-10). For each configuration then we obtain thousands of channel matrix realizations. However, given that the coherence bandwidth is on average much larger than the frequency resolution of the estimator, there will be on the order of hundreds of independent channel matrix realizations per configuration.

9.4.2 Rayleigh Validation

The Kronecker channel model is only applicable to Rayleigh fading channels. Given this we want to restrict our performance analysis to this domain. In the same manner as Section 7.2, we compare the histogram of the channel estimates from each configuration to the Rayleigh distribution to validate that we are operating in the Rayleigh domain. Here we specifically restricted our measurements to Non-Line-Of-Sight (NLOS) links to help ensure that we were operating in the Rayleigh regime.

9.4.3 Stability Validation

Each full MIMO channel measurement involves measuring the channel between the receive array and 7 transmitter positions that simulate a 7-element transmit array. It is necessary that the channel be stable over the duration of this measurement (on the order of a minute) in order to ensure the accuracy of the MIMO data. To maximize stability all measurements were taken at night to minimize activity in the environment. In order to filter out non-stationary data several snapshots were taken for each measurement.

9.4.4 Parameter Estimation

In order to measure the performance of the Kronecker model we must first estimate its parameter space. The parameters of the model are the one-sided correlation matrices among antenna elements, i.e. the transmit and receive correlation matrices.

System Model

Recall that the receiver and channel sounder of the CDCS are not synchronized so that different time snapshots will be offset from one another by a random phase term. This term corresponds to the random phase offset between receiver and transmitter oscillators at the time of the snapshot. In addition given the structure of the channel estimator there is a timing offset between channel estimates at different time snapshots. In the frequency domain this corresponds to a linear phase offset, so that the

196

overall phase offset between channel matrices will be a function of frequency. Given this we can model the narrowband channel matrix measurement as,

$$\tilde{H} = H \cdot D$$

where,

$$D = \begin{pmatrix} \phi_1 & 0 & 0 & \ldots & 0 \\ 0 & \phi_2 & 0 & \ldots & 0 \\ 0 & 0 & \phi_3 & \ldots & 0 \\ \vdots & \vdots & \vdots & \ddots & \vdots \\ 0 & \ldots & 0 & 0 & \phi_M \end{pmatrix}$$

and ϕ_i represents the random phase term at the ith snapshot.

Estimator Definitions

An estimator for the one-sided receiver correlation matrix $(\widehat{K}_{rx})$ can be defined as,

$$\widehat{K}_{rx} = \frac{1}{T \cdot M} \sum_{i=1}^{T} \tilde{H}_i \tilde{H}_i^H$$

where $\tilde{H}_i$ is the ith of T channel matrix measurements. Given the virtual nature of the transmit array, a reference antenna is necessary in estimating the one-sided transmitter correlation matrix. The estimator is defined as,

$$\widehat{K}_{tx} = sqrt(f)$$

$$f = \frac{1}{T \cdot N} \sum_{i=1}^{T} \overline{H}_i^H \overline{H}_i$$

Here $\overline{H}_i$ is defined as the ith channel matrix adjusted by the reference antenna (multiplied by complex conjugate of reference), which we will now show provides an unbiased and consistent estimator.

Properties of Estimators

Both estimators can be shown to be unbiased and consistent.

$$\widehat{K}_{rx} = \frac{1}{T \cdot M} \sum_{i=1}^{T} \tilde{H}_i \tilde{H}_i^H$$

where $\tilde{H}_i$ represents the ith of T total measurements of the MIMO channel. We can expand this as,

$$\Rightarrow \widehat{K}_{rx} = \frac{1}{T \cdot M} \sum_{i=1}^{T} H_i D_i D_i^H H_i^H$$

$$\Rightarrow \widehat{K}_{rx} = \frac{1}{T \cdot M} \sum_{i=1}^{T} H_i H_i^H$$

The $(n, m)^{th}$ element of this estimator is,

$$(\widehat{K}_{rx})_{n,m} = \frac{1}{T \cdot M} \sum_{i=1}^{T} r_{i,n} \cdot r_{i,m}^H$$

where $r_{i,n}$ corresponds to the nth row (n^{th} receive antenna) of the ith channel matrix realization. The underlying assumption is that the distribution is constant across channel realization so that the estimator should have the following distribution,

$$(\widehat{K}_{rx})_{n,m} \sim \mathcal{CN}(\frac{E[r_{i,n} \cdot r_{i,m}^H]}{M}, \frac{Var[r_{i,n} \cdot r_{i,m}^H]}{T})$$

$$= \mathcal{CN}((K_{rx})_{n,m}, \frac{C}{T})$$

where C is a constant. Here we see that this estimator of the receiver covariance matrix is unbiased and consistent. Similarly we have for the transmit covariance matrix,

$$\widehat{K}_{tx} = \frac{1}{T \cdot N} \sum_{i=1}^{T} \tilde{H}_i^H \tilde{H}_i$$

We can expand this as,

$$\Rightarrow \widehat{K}_{tx} = \frac{1}{T \cdot N} \sum_{i=1}^{T} D_i^H H_i^H H_i D_i$$

Here the random phase component affects the estimator. Instead consider using the first receive antenna as a reference and define,

$$H_2 = \begin{pmatrix} r_2 \\ r_3 \\ \vdots \\ r_N \end{pmatrix}$$

$$H_1 = \begin{pmatrix} r_1 \\ r_1 \\ \vdots \\ r_1 \end{pmatrix}$$

with H_1, $H_2 \in C^{(N-1)xM}$. Now define,

$$\overline{H} = \tilde{H}_2 \odot \tilde{H}_1^*$$

$$= (H_2 \cdot D) \odot (H_1 \cdot D^*)$$

$$= H_2 \odot H_1^*$$

Now consider the statistic,

$$f = \frac{1}{T \cdot N} \sum_{i=1}^{T} \overline{H}_i^H \overline{H}_i$$

The $(n, m)^{th}$ element of this statistic is,

$$f_{n,m} = \frac{1}{T \cdot N} \sum_{i=1}^{T} (t_{i,n}^H \cdot t_{i,n}^1) \cdot (t_{i,m} \cdot (t_{i,m}^1)^H)$$

$$= \frac{1}{T \cdot N} \sum_{i=1}^{T} t_{i,n}^{H} \cdot t_{i,m} \cdot (t_{i,m}^{1})^{H} \cdot t_{i,n}^{1}$$

where $t_{i,n}$ corresponds to the nth column (n^{th} transmit antenna) of the ith referenced channel matrix realization, $\overline{H}_i$. Similarly $t_{i,n}^{1}$ corresponds to the channel between the nth transmit antenna and first receive antenna (n^{th} reference channel) of the ith channel matrix realization. In our system we place the reference antenna sufficiently far ($>$ several wavelengths) away such that its channel can be considered approximately independent on average from the others leaving,

$$f \sim \mathcal{CN}(\frac{E[t_{i,n} \cdot t_{i,m}^{H}]}{M} \cdot E[|t_{i,n}^{1}|^2], \frac{Var[t_{i,n} \cdot t_{i,m}^{H}] \cdot Var[|t_{i,n}^{1}|^2]}{T})$$

$$\Rightarrow f \sim \mathcal{CN}(((K_{tx})_{n,m})^2, \frac{C}{T})$$

Then the statistic $\sqrt{f}$ converges to $(K_{tx})_{n,m}$ with increasing sample size T.

9.4.5 Performance Analysis

Given the parameter space estimates for each link configuration we can use the Kronecker model to generate a set of T channel matrices $\{H_i^K\}_{i=1}^T$ predicted for each link by the model equation,

$$H_i^K = \widehat{K}_{rx}^{\frac{1}{2}} G_i (\widehat{K}_{tx}^{\frac{1}{2}})^T$$

where G_i is an N by M matrix whose entries have an IID complex gaussian distribution. In order to carry out performance analysis on the Kronecker model we then need to come up with an appropriate metric for comparing the realized channel matrices, $\{H_i\}_{i=1}^T$, to those predicted by the Kronecker model, $\{H_i^K\}_{i=1}^T$.

We measure the accuracy of the Kronecker model in predicting the spatial multiplexing structure of the channel with average mutual information (b/s/Hz) as our metric. More specifically we calculate the average mutual information predicted by the Kronecker model and compare it to that of the corresponding measured channels. The true average (across tone and spatial realization) realized mutual information is

calculated as,

$$C_{ave} = \sum_{i=1}^{T} \log_2(\det|I + \frac{SNR}{N}H_iH_i^H|)$$

where N is the size of the array (here 7), and H_i is the ith of T measured channel matrix realizations. The same formulation is used to calculate the Kronecker predicted mutual information by replacing the channel matrices $\{H_i\}_{i=1}^{T}$, with $\{H_i^K\}_{i=1}^{T}$.

Additionally the goal of this study is to observe how this performance analysis varies as a function of channel environment. Recalling Section 9.2, an environment is kronecker-structured if and only if the two propagation conditions introduced in [17] are met. The first propagation condition holds in our measurements as the antenna elements were of the same manufacturing line and orientated identically with half wavelength spacing. The performance of the model should then be related to how well the environment meets the second propagation condition, namely independence of AOA and AOD spectrums.

In order to test this we have bisected our measurement campaign into two environmental regimes. The first regime consists of around-the-corner propagation scenarios similar to that from Chapter 6 that are dominated by single-bounce propagation paths. The second regime includes longer link-length scenarios within residential neighborhoods. Here the transmitter and receiver locations were on opposite sides of a residential street block so that propagating paths were forced to traverse between houses and trees in order to complete the link. Figures 9-4 and 9-5 display representative measurement locations from environment regimes 1 and 2 respectfully. Note that the GPS image of Figure 9-4 includes some buildings that were removed before measurements were taken. Given this setup approximately 30 link scenarios were measured with approximately half belonging to each of the environment scenarios outlined above.

Figure 9-6 displays the result of the experiment utilizing our performance metric of mutual information at 20dB SNR. Upon inspection we see that the Kronecker model tends to underestimate the mutual information of the MIMO channel. This result supports the observation of underestimation within indoor environments by
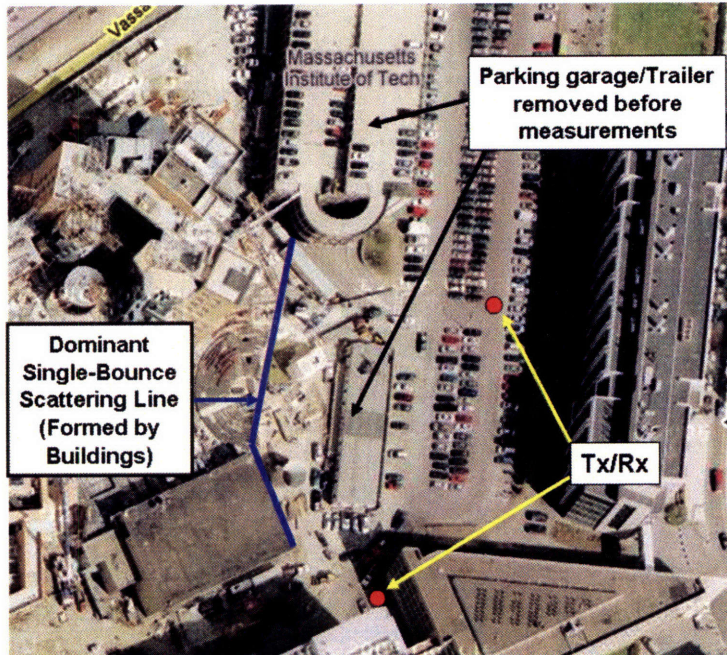
Figure 9-4: Example environment from regime 1 of kronecker measurement campaign. Here single-bounce propagation paths dominate.

[35]. Additionally we see that this underestimation increases with decreasing channel capacity. Specifically the model prediction has an rms error of $1.7 \frac{bits}{s \cdot Hz}$.

The Kronecker model specifically simplifies the structure of the channel covariance matrix into a parameter space that can be more easily estimated. Given this, a decrease in the sparsity of the channel correlation matrix (i.e. more high correlations) will result in an increase in modeling error. This follows from the fact that as the complexity of the system being modeled decreases (moves closer to the model domain) the potential for modeling error similarly decreases. An increase in correlation among channel matrix entries corresponds to a decrease in channel capacity, which supports this result. In particular it supports the observation that the Kronecker modeling error increases with decreasing channel capacity.

Environmental Dependence

Returning to Figure 9-6 we see that the scatter plot is color-coded according to environmental regime. Recalling the previous section, our measurement campaign
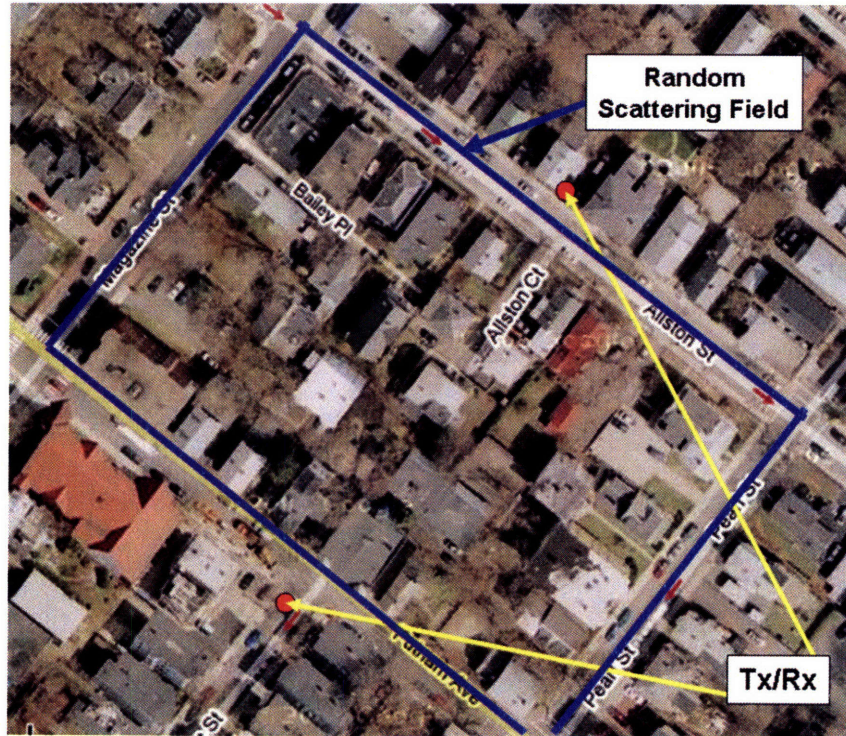
Figure 9-5: Example environment from regime 2 of kronecker measurement campaign.

centered around two link scenarios, namely:

1. **Regime 1:** Single-bounce dominated propagation: Around-the-corner propagation.

2. **Regime 2:** Multi-bounce propagation: link-ends separated physically by random scattering fields, specifically residential buildings and trees.

By inspection of Figure 9-6 we see that the kronecker model tends to be more accurate when applied to the environments of regime 2 as opposed to regime 1. Specifically there is a 3dB performance advantage (Single-bounce: 2.1 $\frac{bits}{s \cdot Hz}$ rms, Multi-bounce: 1 $\frac{bits}{s \cdot Hz}$ rms) in this prediction when applied to environments in regime 2 as compared to regime 1. Recalling the above discussion, the kronecker model assumes that the propagation environment supports independent direction-of-arrival (DOA) and direction-of-departure (DOD) spectrums. The regime-1 link scenarios were selected to be biased towards single-bounce propagation. In such propagation conditions each DOA corresponds to a single DOD which specifically violates independence. In con-
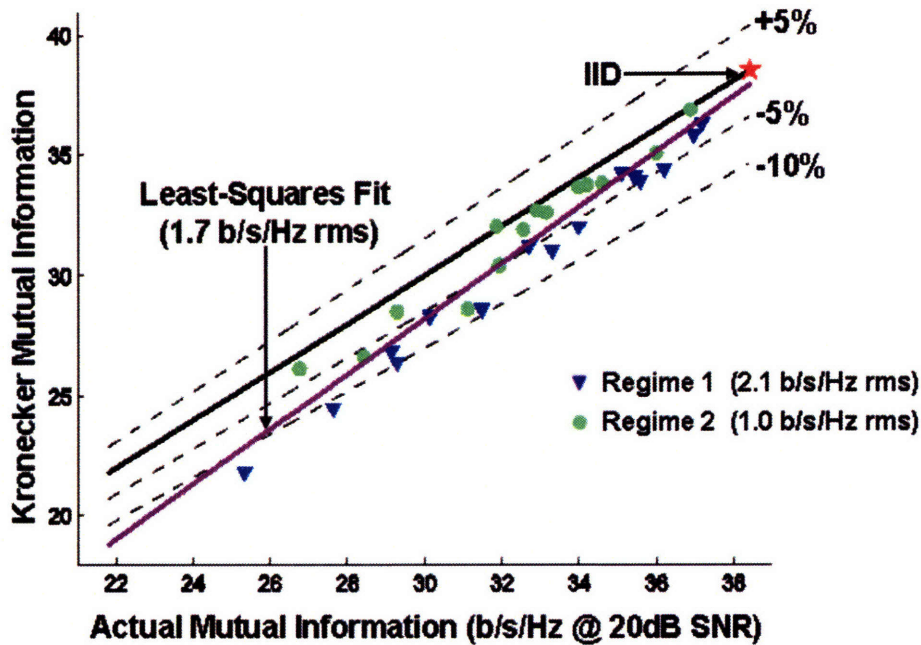
Figure 9-6: Kronecker Model Performance Analysis

trast the link scenarios from regime 2 include propagation paths that traverse random scattering fields. Here energy from a single DOD is potentially received at each of the primary DOAs as propagation paths randomly split into multiple physical paths while traversing the scattering field. Although independence is far from assured, the more equitable distribution of energy between each DOD and the primary DOAs make the independence assumption more plausible. This result illustrates that while the independence assumption implied by the kronecker model typically can not be physically justified, the approximation can in some environments be relatively acceptable. Specifically we see that when applied to longer link-lengths with more scattering mechanisms modeling error will tend to decrease.

Capacity Underestimation

As seen in figure 9-6 the kronecker tends to underestimate the actual mutual information of the channel. The mutual information of the MIMO channel depends on the singular value distribution of the channel matrix H (channel shape). To better under-

204

stand the nature of the kronecker modeling error we can look at the average singular value distribution of the actual channel data and compare it to the corresponding distribution predicted by the kronecker model.
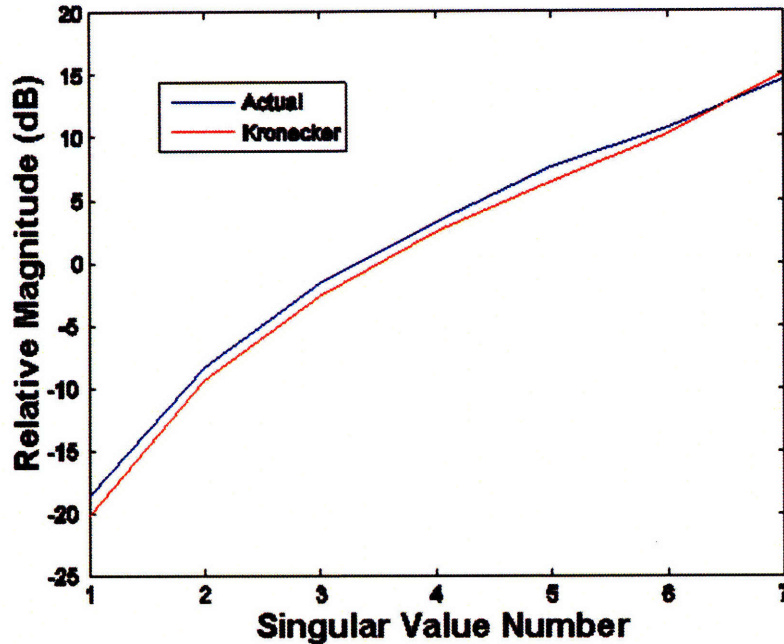

Figure 9-7: Kronecker model performance: channel shape

Figure 9-7 displays the singular value distribution of both the actual and kronecker predicted channel data from a representative link scenario. Here we see that largest singular value from the kronecker distribution is larger than the corresponding largest singular value of the real data. Additionally the remaining smaller eigenvalues from the kronecker distribution are smaller than their counterparts from the actual data set. In essence the kronecker model has estimated the channel shape to be "steeper" than it actually is. This behavior was consistent throughout the set of link scenarios. Recalling Section 2, mutual information increases when the channel shape becomes flatter, i.e. equal magnitude across eigenmode/sigular value. The observation of the kronecker model steepening the channel shape is then consistent with the underestimation of mutual information.

As demonstrated in Section 9.4.5 the modeling error arises from the channel envi-

ronment not supporting the necessary propagation condition of independence between DOD and DOA spectrums. To test whether violating this condition results in the same modeling error behavior observed in our data we have performed a collection of simulations. The simulation is carried out in the analytical domain making the complete covariance matrix, R, the object of the simulation rather than the underlying propagation mechanisms. The simulation assumes that the covariance matrix R is comprised of a weighted average of two covariance matrices,

$$R = w \cdot R_K + (1 - w) \cdot R_N \qquad 0 \leq w \leq 1$$

The matrix R_K is assumed to be a covariance matrix that satisfies mathematical necessary conditions of the kronecker model namely,

$$R_K = R_r \otimes R_t$$

for some one-sided correlation structure R_r, R_t at both link ends. The matrix R_N is a randomly generated matrix constrained only to be positive definite. With this setup we can then vary the structure of the covariance matrix R from completely constrained within the kronecker condition space (w=1) to completely unconstrained (w=0). We can then see how the performance of the kronecker model degrades with decreasing w.

Figure 9.4.5 displays a representative simulation for 4 values of w. For each value we have plotted the average channel shape for a set of channels that were generated from the actual covariance matrix R, and the corresponding shape for a set of channels generated using the covariance matrix predicted by the kronecker model. Here we can see how the channel shape predicted by the kronecker model perfectly matches the actual channel shape when the covariance matrix is completely constrained within the kronecker mathematical conditions (w=1). As these constraints are loosened (decreasing w) we see the channel shape predicted by the kronecker model becomes increasingly more steep than the actual channel shape. This matches the behavior observed in the real channel data.

206
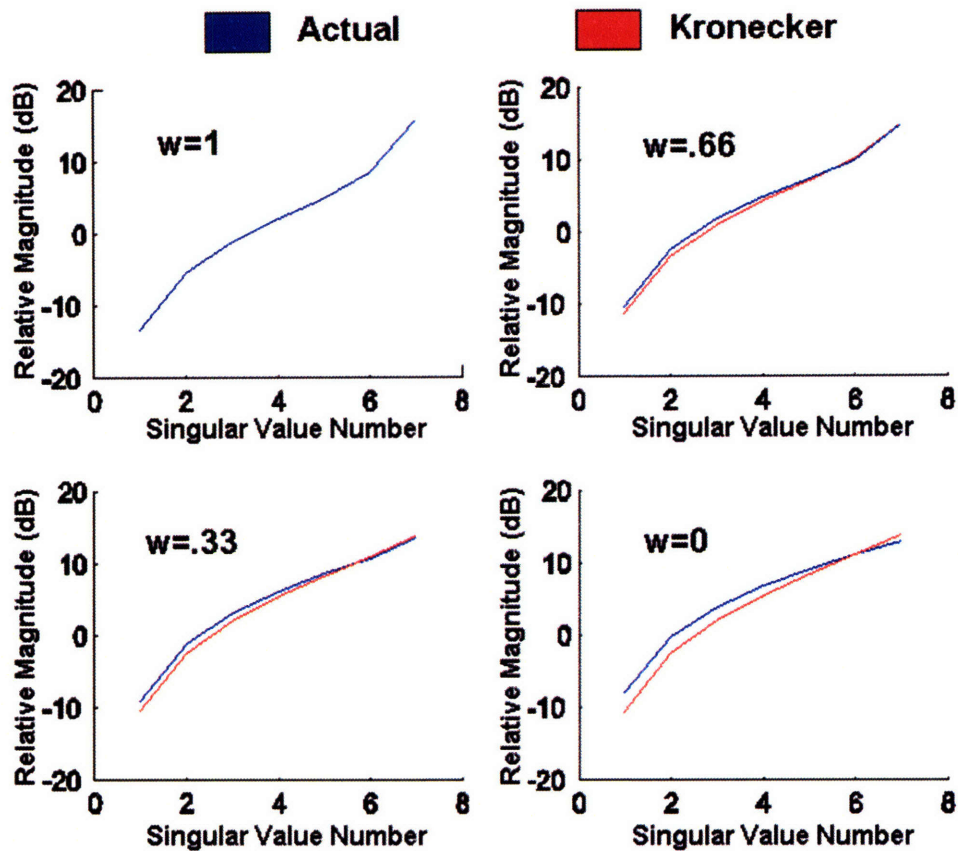
9.5 Spatial Diversity

In section 2.4.1 diversity was discussed as an single link-end metric of the spatial structure of the wireless channel. Multiple antenna systems use spatial diversity in order to increase the likelihood of high data rate communication. The idea is that each spatially offset antenna will have a distinct channel structure making it more likely that at least one antenna will have an acceptable Signal-to-Noise to ratio.

In our field experiments we have collected a large amount of coherent multiple antenna data where the spatial displacements between adjacent antennas is on the order of 1-2 wavelengths. As an example of this behavior Figures 9-8, 9-9, and 9-10 display the channels at each of 6 antennas for various levels of multipath (coherence bandwidth).

The most common method for modeling this behavior is to assume that the chan-
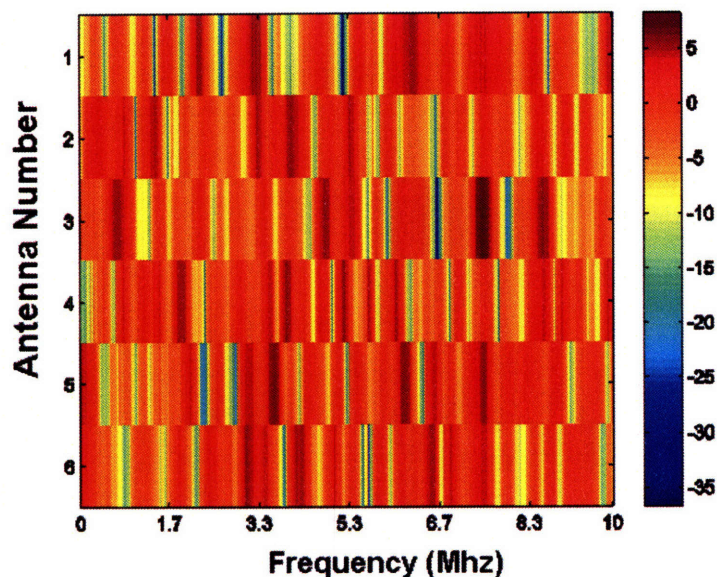
Figure 9-8: Instantaneous channel response at each of 6 antennas, Example 1: High Multipath

nel at each antenna is Rayleigh distributed and mutually independent of the channels at the other antennas. For independence between antennas it is implicitly assumed that the antennas are sufficiently far apart, typically at least half a wavelength. More sophisticated models are needed for compact systems where the antennas are spaced closer than this.

Here we wanted to test how well the above assumptions hold when applied to real channel data. In Section 7.2 we showed that the channels at each individual antenna are modeled accurately by the Rayleigh fading model. However we did not analyze the relationship between antennas in this analysis. In the above Kronecker experiments we showed that the channel response at closely spaced antennas (sub wavelength) will in general not be independent of one another. This was observed in Figure 9-6 as the realized channel capacity of the MIMO channels observed was generally lower than what would be present if there were complete independence between antennas. As a further example of this behavior Figures 9-11 and 9-12 show how the structure of the channel evolves smoothly over small spatial offsets for an outdoor and indoor link respectfully.
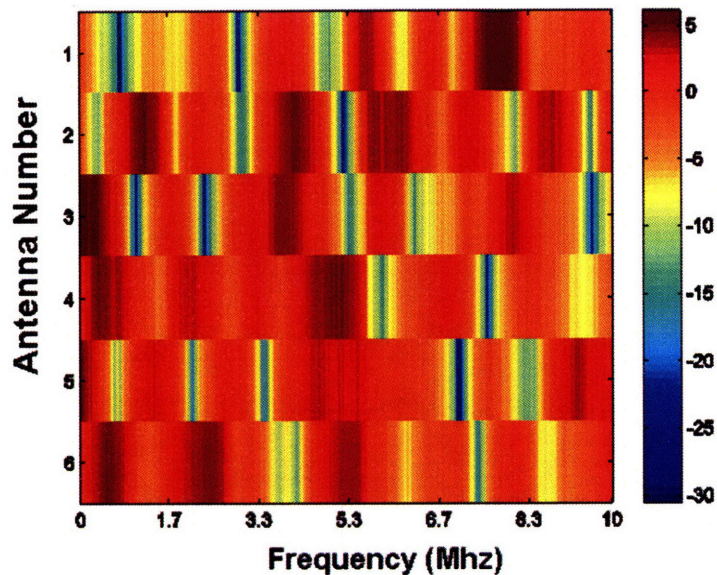
Figure 9-9: Instantaneous channel response at each of 6 antennas, Example 2: Medium Multipath

The question under consideration in this analysis however is whether independence can be reasonably assumed in systems where several wavelength spacing is present between antennas.

In order to test this we consider the following metric, the probability of having a channel with a power of at least X dB (relative to the average power for that link) when utilizing K antennas at one link-end. Formally this can be defined as:

$$P_D(K, X) = P(\max_{i=1,..,K} P_i \geq X)$$

where P_i is the power in dB (normalized to the average link-power) of the ith of K antennas. This is a useful metric for measuring spatial diversity as it characterizes well the utility in deploying multiple antennas for use in diversity-based systems. In the case of independence among antennas this probability measure should grow with the number of antennas as,

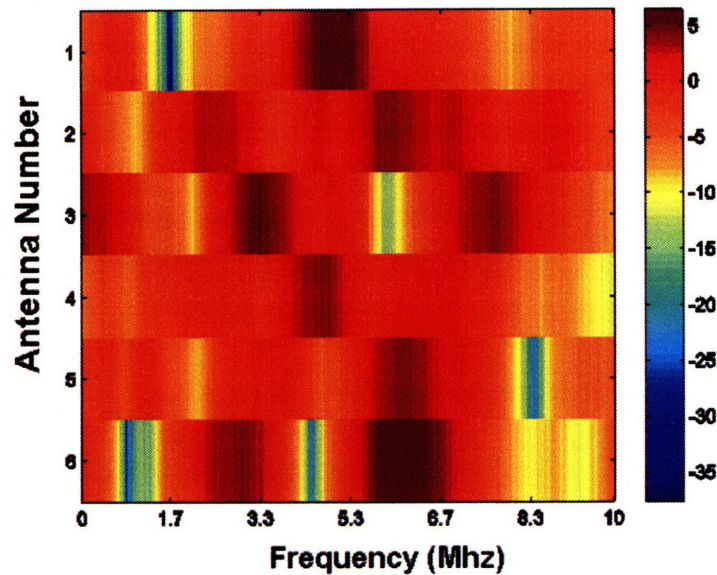$$P_D(K, X) = 1 - (1 - P_D(1, X))^K$$

209

Figure 9-10: Instantaneous channel response at each of 6 antennas, Example 3: Low Multipath

where $P_D(1, X)$ denotes the probability that a single antenna has a power of at least X dB which is a function of the distribution of channel. Figures 9-13 and 9-14 display the result of applying this diversity metric (Quality of Service) for a range of power thresholds (X) and antenna numbers (K) to a large collection of data.

The solid lines correspond to the realized value of the metric when applied to our channel data and dashed lines correspond to the values predicted by a model with independent Rayleigh distributed channels. Figure 9-13 corresponds to street data while Figure 9-14 is from the rich scattering environment displayed in Figure 9-4. Here we observe a good match between the model and data suggesting that not only is a Rayleigh model appropriate for modeling the multipath characteristics of Non-Line-Of-Sight links but additionally we can consider the channel response between antennas to be independent so long as they are separated by at least a couple of wavelengths. Practically speaking, this simplifies our choice of the number of antennas to deploy as it provides us with a simple model for assessing the number of antennas necessary to achieve a particular quality of service (QoS) requirement in a diversity-based system.
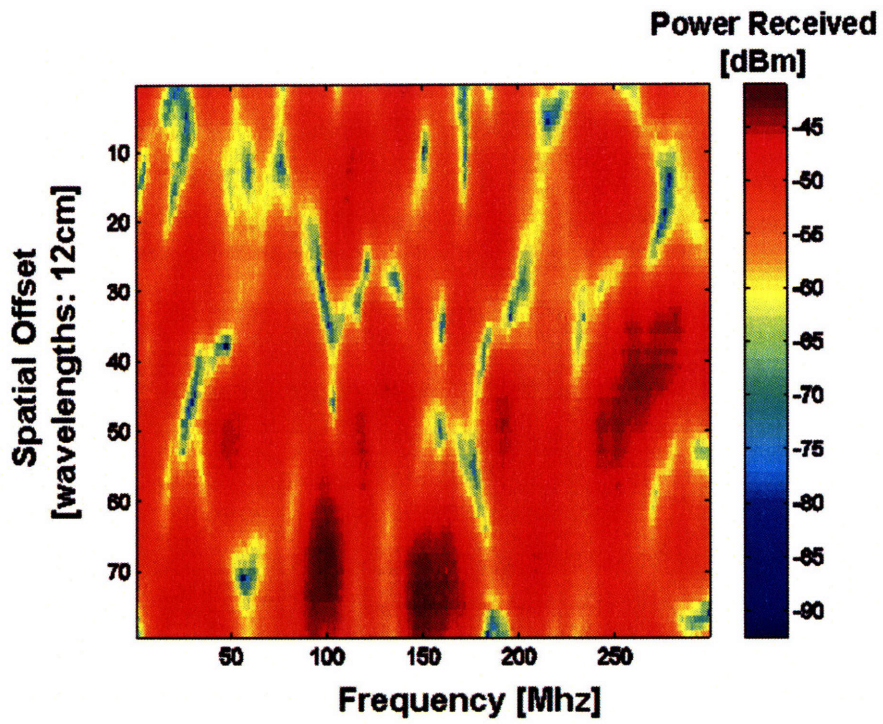
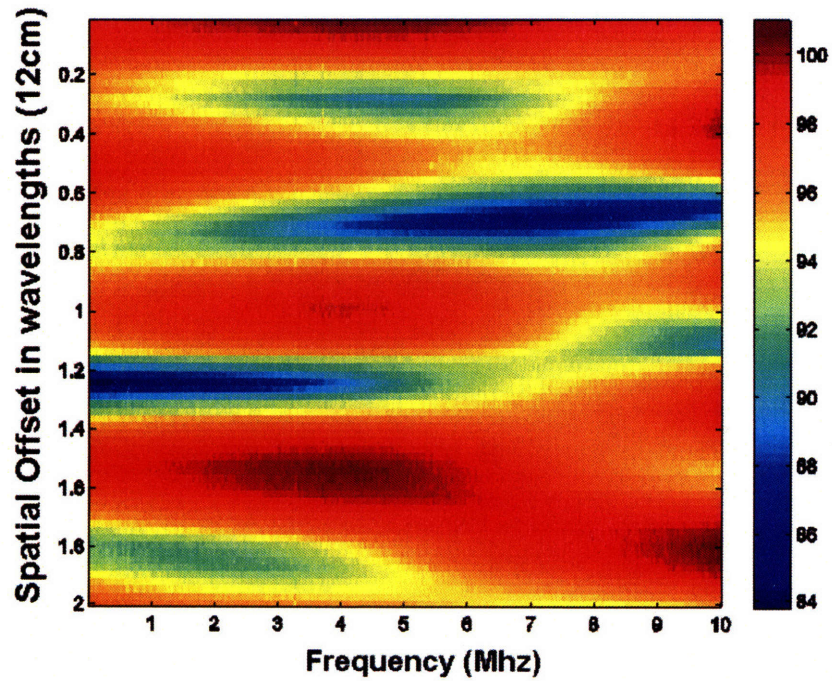Figure 9-11: Image of spatial/frequency structure of an outdoor channel

Figure 9-12: Image of spatial/frequency structure of an indoor channel
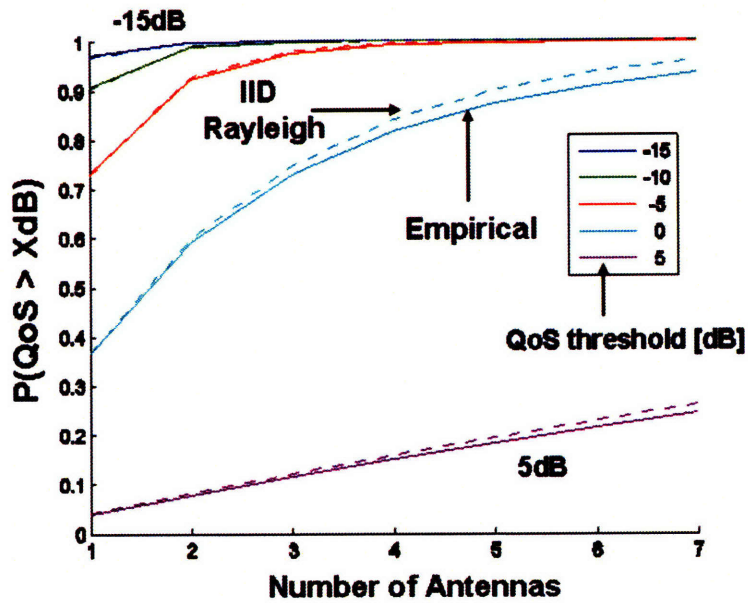
Figure 9-13: Quality of Service (QoS) as a function of number of antennas: street environments
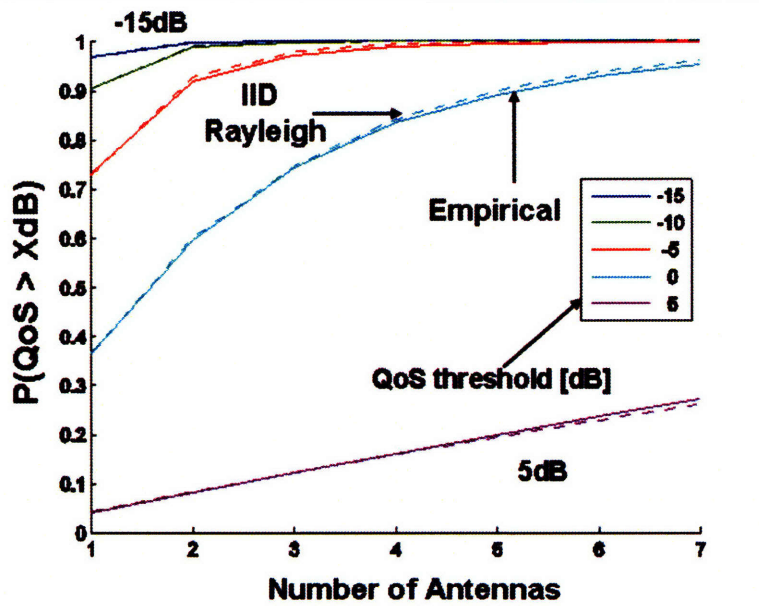

Figure 9-14: Quality of Service (QoS) as a function of number of antennas: Parking Lot

Chapter 10

Conclusions and Future Work

10.1 Conclusions

In conclusion, we have parameterized what we believe to be the important degrees of freedom associated with wireless propagation that are relevant to wireless system and protocol design, namely the path-loss, frequency, time stability, spatial, and polarization structure of the wireless channel. Given this characterization we have developed a collection of empirically tested channel models and experiments that provide improved insight into the behavior of these propagation parameters.

Specifically we have developed a path-loss model for ground-to-ground communication over sub-kilometer link lengths that outperforms traditional empirical models by utilizing physical micro-parameters of the environment. Specifically in street environments, which empirical models consider a single macro-environment type, we have developed an estimator for the path-loss coefficient α that is a function of two building-gap metrics and has an empirical rms error of 0.22 α for α ranging between 2 and 5. Here we conclude that path-loss estimates can be improved by as much as 10dB for link lengths as short as 100 meters by utilizing efficient representations of the environment. In addition we conclude that the path-loss characteristics of air-to-ground links are well represented by a two segment model having a Line-Of-Sight component with $\alpha \approx 2$(above local building/tree scattering line) and a stochastic component (empirically $\approx$ 8dBm standard deviation) due to the variation in local

scattering conditions at the ground link.

Additionally we have carried out robust analysis of the Rayleigh fading model by measuring the fade distribution (frequency domain) over a diverse set of outdoor Non-Line-Of-Sight (NLOS) environments: parking lots, alleys, streets, and residential neighborhoods. Experiments have shown the Rician K-factors of link lengths as short as tens of meters to be quite small (< 1) suggesting that a Rayleigh distribution (K=0) is sufficient in modeling this channel behavior. We have also proposed a model for predicting the multipath structure of the channel (fade width/coherence bandwidth) that utilizes two factors: multipath component (MPC) arrival-rate q $[\frac{MPCs}{m}]$ and MPC decay-rate $\beta[\frac{dBm}{10 \cdot \log_{10}(m)}]$. Measurements indicate a dense arrival-rate (q) (on the order of 1 $\frac{MPC}{m}$) in ground-to-ground links. In this range the frequency structure of the channel is insensitive to q, which reduces the modeling complexity to a single parameter, β. In street environments we have found the decay-rate β to be linear in link-length, and have provided an estimator of beta that has been shown empirically to estimate average fade width with an rms error of 730kHz over a spectrum of fading windows: Unfaded [$> $ -5dB], Faded [-15dB, -5dB], Deeply-faded [$<$ -15dB]. In addition we have shown the complete distribution of fade duration predicted by the model matches measurements over a wide range of link lengths. We conclude that multipath characteristics relevant to system/protocol design can be accurately estimated in these environments utilizing a single parameter, namely link-length.

With respect to channel stability our measurements indicate that the time-coherence length (t_c) of individual MPCs tends to be either less than 300ms (high-frequency) or 5 minutes and longer. We conclude that the time characteristics of the channel are accurately modeled as the superposition of two independent circularly symmetric complex gaussian random variables, corresponding to the channel response due to a set of stable and unstable MPCs. For a particular realization of the stable MPCs the model reduces to Rician fading in the time domain, however in the aggregate the distribution exhibits fatter tails than Rician fading due to the non-negligible probability of the stable MPCs falling in a null. We have shown a close distributional match between model and measurements taken from a diverse set of environments,

link types, and link lengths. Observed S-factors over this data set range from 0-30dB where we define S-factor as the ratio of expected power from the stable and unstable paths (distinct from Rician K-factor where stable component is fixed). Experiments have shown that the S-factor in street environments can be estimated from link-length with an rms error of 3dB. In air-to-ground links the S-factor has been observed to be independent of link length with mean 13dB and standard deviation 3dB. Given this behavior we note that OFDM channels that have experienced a null recently (over recent refresh cycles) are likely to experience a null again in the future as this is indicative of the stable MPCs being in a null. We conclude that channel estimation overhead can be reduced by taking advantage of this systematic behavior, i.e. sticking to channels that have had a history of good signal-to-noise ratio.

Additionally we have explored the realized performance of the Kronecker Multiple-Input Multiple-Output (MIMO) channel model over a collection of outdoor ground-to-ground links. Our observation of capacity underestimation by the Kronecker model matches the indoor experiments of [35]. We also observe a 3dB performance advantage with respect to capacity estimation of this model when applied to multi-bounce scattering environments as opposed to environments dominated by single-bounce propagation. In these 7x7 (number of transmit by receive antennas) experiments we observed average errors on the order of 5 percent which suggest acceptable performance for this model when applied to today's technology that have systems sizes on this order.

In summary we have shown the utility in utilizing efficient environmental representations in modeling channel behavior and estimating the associated parameters of these models. Specific examples of this behavior include our sub-kilometer path-loss model for ground-to-ground links, the S-factor estimator of our channel stability model, and beta estimator in the fade width model. Additionally we have provided empirical performance analysis of popular theoretical models where there was previously little data available. This included empirical studies of the Rayleigh/Rician fading models and the Kronecker MIMO channel model. Lastly we have shown that there exist systematic channel behaviors that can be taken advantage of with respect to both system and protocol design. Examples include incorporating channel fading

history into channel state information update strategies, scaling network density to local building features, and allowing for dynamic channel allocation according to environment. These results we hope will provide further insight into efficient utilization of the wireless propagation channel.

10.2 Future Work

In this section we outline potential extensions to this research.

10.2.1 Extension to Additional Environments

Each propagation environment/link scenario is distinct leading to an infinite number of potential propagation links. Here we have categorized links according to several properties (LOS, Ground-to-Ground, link-length) and environment type (streets, parking lots, residential, etc.). Given this we have shown how model structure and parameters vary according to these properties. However in our measurements we have focused on outdoor links in urban and residential environments. A potential extension to this work would be to study the utility of these models as applied to environments outside of this scope, for example indoor and rural outdoor environments. Specifically in indoor environments a study could include testing whether there is an analog to our ground-to-ground path-loss model that potentially substitutes building gaps with building materials/wall gaps. Additionally we would be interested in seeing how well the Rayleigh fading model holds up in indoor environments and correspondingly the behavior of beta in our fade-width model within this environment type. With respect to stability we would expect S-factors to be related to foot traffic in indoor areas. In rural environments it would be interesting to see if the variance of the log-normal fading in air-to-ground links decreases given the lower density of buildings. Additionally utilizing metrics based on tree density may have utility in these environments.

10.2.2 Model Fine Tuning

Additionally there is room for further analysis within the environments already studied. Specifically in the case of our ground-to-ground path-loss model it would be of interest to study more closely corner losses. In our previous analysis we found an empirical distribution of corner loss that suggested a high power penalty associated with communication around corners. However in the limited samples available we began to see some systematic behavior associated with this penalty as a function of the building types and geometry present at the street corners. There would be utility then in obtaining more corner data so that we could potentially stratify corners according to these physical degrees of freedom and use this stratification to improve corner loss estimation. An additional example of model fine tuning would be to carry out further analysis of our fade-width model. Recall that this model is a function of a single parameter beta, which is a measure of the power penalty incurred for a multipath component having a propagation path longer than the link length. In our analysis we found that in street environments our model accurately represented this behavior utilizing a single parameter of beta. It would be of further interest to see how beta varies over sub-environment type including: parking lots, residential streets vs. urban streets, open areas, etc.

10.2.3 Polarization

The Channel Parametrization introduced in Chapter 3 included channel polarization as one of its parameters. While some preliminary experiments were conducted with respect to polarization during this research, it was found that more data would be necessary in order to properly study this behavior. Specifically, future research of channel polarization should include studying the relationship between α's across channels formed by different polarization combinations (eg. h-to-h, v-to-v, etc.) at each link within different environments to see if any systematic behavior is present. With respect to MIMO technology it would be of interest to empirically study the correlation structure of channels formed across orthogonal polarizations to better un-

derstand the utility of deploying compact arrays utilizing polarization diversity as well as spatial diversity. Additionally, characterizing systematic differences in multipath and time stability behavior across polarization would provide useful information for system engineering.

10.2.4 Model Software Package

Additionally it would be useful to construct a software package for simulating the wireless channel that utilizes the models studied in this thesis. Specifically a software package that uses input link characteristics (e.g. LOS, link-length, link type) and environmental parameters (e.g. building density, traffic rates, outdoors/indoors) to predict channel characteristics such as channel realizations, S-factors, betas, alphas, etc. would be useful for those doing research and engineering in this area.

Bibliography

[1] J. H. Winters, On the capacity of radio communication systems with diversity in a Rayleigh fading environment, IEEE J. Select Areas Commun., vol. SAC-5, pp. 871878, June 1987.

[2] G. J. Foschini and M. J. Gans, On limits of wireless communications in a fading environment when using multiple antennas, Wireless Personal Commun., vol. 6, pp. 311335, Mar. 1998.

[3] T. L. Marzetta and B. M. Hochwald, Capacity of a mobile multiple-antenna communication link in Rayleigh flat fading, IEEE Trans. Inform. Theory, vol. 45, pp. 139157, Jan. 1999.

[4] G. G. Raleigh and J. M. Cioffi, Spatio-temporal coding for wireless communication, IEEE Trans. Commun., vol. 46, pp. 357366, Mar. 1998

[5] MIMO - study propagation first! Bonek, E.; Herdin, M.; Weichselberger, W.; Ozcelik, H.; Signal Processing and Information Technology, 2003. ISSPIT 2003. Proceedings of the 3rd IEEE International Symposium on 14-17 Dec. 2003 Page(s):150 - 153

[6] Tse, David. Fundamentals of wireless communication [electronic resource] / David Tse and Pramod Viswanath. Cambridge: Cambridge University Press, 2005

[7] Bliss, D.W.; Chan, A.M.; Chang, N.B., "MIMO wireless communication chan-

nel phenomenology," Antennas and Propagation, IEEE Transactions on, vol.52, no.8, pp. 2073-2082, Aug. 2004

[8] Rappaport, Theodore S., 1960- Wireless communications : principles and practice /Theodore Rappaport. Upper Saddle River, N.J. : Prentice Hall PTR, c2002.

[9] P. Gupta and P. Kumar, "The capacity of wireless networks" , IEEE Transactions on Information Theory, vol. 46, 2000.

[10] Characteristics of measured 44 and 1010 MIMO wireless channel data at 2.4-GHz Wallace, J.W.; Jensen, M.A. Antennas and Propagation Society International Symposium, 2001. IEEE, Vol.3, Iss., 2001 Pages:96-99 vol.3

[11] Measured propagation characteristics of simulcast signals in an indoor microcellular environment Harbin, S.; Palmer, C.; Rainer, B.K. Vehicular Technology Conference, 1992 IEEE 42nd, Vol., Iss., 10-13 May 1992

[12] Hashemi, H., Impulse Response Modeling of Indoor Radio Propagation Channels, IEEE J. on selected Areas in Comm., Vol 11, No. 7 pp. 967-977, 1993

[13] RMS delay and coherence bandwidth measurements in indoor radio channels in the UHF band, Valera, M.S.; Sanchez, M. G., Vehicular Technology, IEEE Transactions on, Volume: 50 Issue: 2 Mar 2001, Pages 515-525

[14] Okamura, Y. a kol.: Field Strength and its Variability in VHF and UHF Land-Mobile Radio Service. Rev. Elec. Comm. Lab. No.9-10pp. 825 - 873, 1968.

[15] Hata, M.: Empirical Formula for Propagation Loss in Land Mobile Radio Services. IEEE Trans. Vehicular Technology, VT-29, pp. 317 - 325, 1980.

[16] A review of antennas and propagation for MIMO wireless communications Jensen, M.A.; Wallace, J.W.; Antennas and Propagation, IEEE Transactions on Volume 52, Issue 11, Nov. 2004 Page(s):2810 - 2824

[17] C. Oestges, Validity of the Kronecker model for MIMO correlated channels, in Proc. Vehicular Technology Conference, Melbourne, Australia, May 2006, vol. 6, pp. 2818 2822.

[18] D. Shiu, et al., "Fading correlation and its effect on the capacity of multielement antenna systems," IEEE Trans. Comm., vol. 48, no. 3, pp. 502-5 13, 2000.

[19] D. Chizhik, J. Ling, P.W. Wolniansky, R.A. Valenzuela, N. Costa, K. Huber, "Multiple-Input Multiple-Output measurements and modelling in Manhattan," IEEE J. Select. Areas Commun., vol. 21, No. 3, pp. 321- 332, 2003.

[20] J.P. Kermoal, et al., "A stochastic MIMO radio channel model with experimental validation," IEEE J. Selected Areas Commun., vol. 20, no. 6, pp. 1211-1226, 2002.

[21] Measurement and characterization of broadband MIMO fixed wireless channels at 2.5 GHz Baum, D.S.; Gore, D.; Nabar, R.; Panchanathan, S.; Hari, K.V.S.; Erceg, V.; Paulraj, A.J.; Personal Wireless Communications, 2000 IEEE International Conference on 17-20 Dec. 2000 Page(s):203 - 206

[22] Measurements of the spatio-temporal polarization characteristics of a radio channel at 1800 MHz Nilsson, M.; Lindmark, B.; Ahlberg, M.; Larsson, M.; Beckman, C.; Vehicular Technology Conference, 1999 IEEE 49th Volume 1, 16-20 May 1999 Page(s):386 - 391 vol.1

[23] Effect of antenna polarization on the capacity of a multiple element system in an indoor environment Kyritsi, P.; Cox, D.C.; Valenzuela, R.A.; Wolniansky, P.W.; Selected Areas in Communications, IEEE Journal on Volume 20, Issue 6, Aug. 2002 Page(s):1227 - 1239

[24] Diversity and multiplexing: a fundamental tradeoff in multiple-antenna channels Lizhong Zheng; Tse, D.N.C. Information Theory, IEEE Transactions on, Vol.49, Iss.5, May 2003 Pages: 1073- 1096

[25] The double-directional radio channel Steinbauer, M.; Molisch, A.F.; Bonek, E.;

Antennas and Propagation Magazine, IEEE Volume 43, Issue 4, Aug. 2001
Page(s):51 - 63

[26] Keyhole Effect in MIMO Wireless Channels: Measurements and Theory Almers,
P.; Tufvesson, F.; Molisch, A.F. Wireless Communications, IEEE Transactions
on, Vol.5, Iss.12, December 2006 Pages:3596-3604

[27] Jakes, William C. Microwave mobile communications.Edited by William C.
Jakes, Jr. New York, Wiley [c1974]

[28] ROOFNET. Computer Science and Artificial Intelli-
gence Laboratory, Massachusetts Institute of Technology.
¡http://pdos.csail.mit.edu/roofnet/doku.php¿

[29] T. Kurner, D. J. Cichon, andW.Wiesbeck, Concepts and results for 3D digi-
tal terrain-based wave propagation models: An overview, IEEE J. Select Areas
Commun., vol. 11, pp. 10021012, Sept. 1993.

[30] S. Y. Seidel and T. S. Rappaport, Site-specific propagation prediction for wireless
in-building personal communication system design, in Proc. IEEE 52nd Veh.
Technol. Conf., vol. 43, 1994, pp. 879891.

[31] G. E. Athanasiadou, A. R. Nix, and J. P. McGeehan, A microcellular ray-tracing
propagation model and evaluation of its narrow-band and wide-band predictions,
IEEE J. Select Areas Commun., vol. 18, pp. 322335, Mar. 2000.

[32] K. Schaubach, N. J. Davis, T. S. Rappaport, "A Ray Tracing Method for Predict-
ing Path Loss and Delay Spread in Microcellular Environments," IEEE Vehicular
Technology Conference, Denver, CO, May 1992, pp. 932 935.

[33] V. Erceg, K. V. S. Hari, et al., "Channel models for fixed wireless applications,"
tech. rep., IEEE 802.16 Broadband Wireless Access Working Group, January
2001.

[34] COST Action 231, "Digital mobile radio towards future generation systems, final report," tech. rep., European Communities, EUR 18957, 1999.

[35] H. Ozcelik, N. Czink and E. Bonek, "What makes a good MIMO channel model?," in Proc. IEEE Veh. Techn. Conf Spring, VTC-S '05 (Stockholm, Sweden), vol. 1, pp. 156-160, May 2005.

[36] Tepedelenlioglu, C.; Abdi, A.; Giannakis, G.B., "The Ricean K factor: estimation and performance analysis," Wireless Communications, IEEE Transactions on , vol.2, no.4, pp. 799-810, July 2003